ISSN 1068-3755, Surface Engineering and Applied Electrochemistry, 2008, Vol. 44, No. 1, pp. 1–5. © Allerton Press, Inc., 2008.
Original Russian Text © A.I. Dikusar, L.I. Bruk, E.V. Monaico, D.A. Sherban, A.V. Simashkevich, I.M. Tiginyanu, 2008, published in Elektronnaya Obrabotka Materialov, 2008, No. 1, pp. 4–9.

ELECTRICAL PRECISION TREATMENT OF MATERIALS

Photoelectric Structures Based on Nanoporous p-InP

A. I. Dikusar[a], L. I. Bruk[a, b], E. V. Monaico[c], D. A. Sherban[a], A. V. Simashkevich[a], and I. M. Tiginyanu[a, c]

[a] *Institute of Applied Physics, Academy of Sciences of Moldova, ul. Academiei 5, Chisinau, MD-2028 Republic of Moldova*
e-mail: dikusar@phys.asm.md
[b] *Moldova State University, ul. Mateevicha 60, Chisinau, MD-2009 Republic of Moldova*
[c] *Technical University of Moldova, ul. Shtefana chel Mare 168, Chisinau, MD-2004 Republic of Moldova*

Received September 11, 2007

Abstract—The possibility of nanostructuring of surfaces of indium phosphide with hole conduction is confirmed. The technique of manufacturing and research of SnO_2/InP heterostructures with a nanoporous surface at the interface is developed. It is shown that the investigated structure can form a basis for working out photovoltaic devices with an enlarged active surface.

DOI: 10.3103/S1068375508010018

Indium phosphide is one of the most promising materials for preparation of photoelectric structures, since its bandgap corresponds to the energy of photons of the maximum of the solar irradiation spectral radiation. Therefore, its application makes it possible to obtain the highest efficiency of solar energy transformation into electric energy. Indeed, on the basis of InP, there have already been prepared solar cells with efficiency exceeding 20% [1]. However, due to the high cost of the base material, these cells are not competitive for terrestrial application. It is also known [2] that indium phosphide is a radiation-resistant material; devices on its basis, in particular, solar cells, can operate in conditions of ionization radiation.

The cost of solar cells' may be reduced due to simplification of their fabrication technology, for example, preparation of semiconductor–insulator–semiconductor (SIS) structures by the method of pyrolytic pulverization of a mixture of tin and indium oxides (ITO) on the surface of p-InP crystals [3–6]. The advantage of this method is that its technological preparation does not require the high-temperature processes of diffusion or epitaxy necessary for formation of surface hetero- or *p–n*-junctions in traditional solar cells. In the case of SIS structures, the potential barrier separating the photogenerated charge carriers is formed at the ITO–InP interface, whereupon a tunnel-transparent thin oxide layer of P_2O_5 appears in the process of the ITO layer spraying [7, 8].

The same result may be achieved by enlargement of the active effective area of the photovoltaic cell. The active area enlargement usually occurs due to its texturing by selective chemical etching. As a result, on the surface of the base semiconductor material, there are formed inverse pyramids or truncated cones, their bases having dimensions of about 5×5 μm or a diameter of 10 μm, respectively (see Fig. 1).

The nanostructured surface is a limiting case of texturing. Such a surface has a maximum surface value; therefore, research of the possibility to apply semiconductor materials with a nanostructured active surface in photoelectric devices appears to be relevant. Hence, the aim of the present paper is to study the possibility to obtain heterostructures based on conducting solar-radiation-transparent oxides ITO, SnO_2, and p-InP with a nanoporous surface as well as the corresponding photovoltaic cells; the authors have accumulated sufficient experience in their preparation with application of indium phosphide with a smooth surface [2–6].

The parameters of the photocells prepared on the basis of ITO/p-InP structures with a smooth surface are given in the table.

As one can see from the table, the efficiency of the ITO/p-InP structures prepared by a simple method of pulverization of a solution of indium and tin chlorides in ethanol on indium phosphide plates at a temperature of 450°C is comparable with the efficiency of other

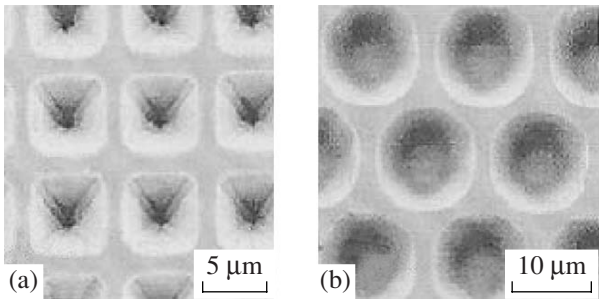

Fig. 1. Textured active surfaces of the photocells in the form of inverse pyramids (a) and truncated cones (b).

Parameters of ITO/p-InP photocells

InP surface orientation	Surface area, cm^2	U_{xx}, V	J_{sc}, mA/cm^2	FF	Efficiency, %
(111)B	1.0	0.674	28.3	0.74	10.4
$(100)p^+/p$	1.0	0.707	30.8	0.73	11.6
(111)A	1.0	0.626	22.72	0.71	10.1

structures based on this semiconductor material, CdS/p-InP, p–n-InP prepared by more sophisticated technology [2].

Anodic electrochemical etching is one of the simple methods for formation of a nanoporous surfaces; however, up to the present moment, specialists do not have a uniform understanding of the mechanisms of the pore formation. Thus, if in 2005 a group of German specialists [9] stated, concerning pore formation in InP, that nanopores could be obtained both on an n-InP surface and on a p-InP one, then, based on their ideas of nanopore formation, the authors of [10] insist on the impossibility of electrochemical pore formation on a p-InP surface. Nevertheless, taking into account recommendations given in [9], applying anodic etching in 1 M HBr of the p-InP crystal surface with the charge carrier concentration 10^{16}–10^{17} cm^{-3}, we have obtained nanoporous layers with a thickness of 3–5 μm with a pore diameter of 500–800 nm. True, the nanoporous layer on the p-InP surface was not continuous; it occupied approximately 80% of the area subjected to the electrochemical etching.

The ITO/p-InP structures on both the smooth (look above) and nanoporous surface formed by the electrochemical etching were obtained by the method of pyrolytic pulverization of alcoholic solutions of indium and tin chlorides in a ratio of 10 : 1 by virtue of the installation described in [11]. The dispersive gas was oxygen. The InP substrate temperature was 450°C, and the spraying time was 60–80 s. However, as one can see from the results of the surface study by virtue of the scanning electron microscope (SEM), it turned out that, on the nanoporous InP surface, a continuous ITO film does not appear, conglomerates of solidificated drops of In_2O_3 are formed instead (see Fig. 2). It is not improbable that, due to the nonuniform temperature distribution over the nanoporous surface (it is obviously higher on spikes of nanopore walls) and due to the low melting temperature, indium at pyrolysis conglomerates into drops, which are well defined in Fig. 2.

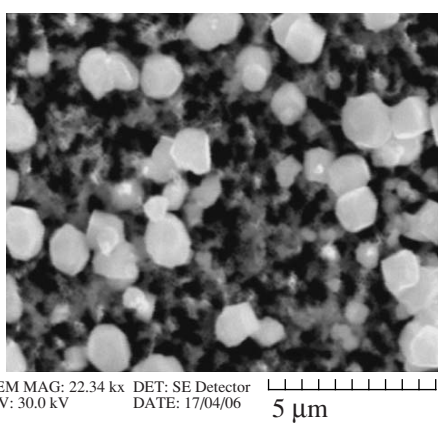

Fig. 2. SEM image of the nanoporous InP surface with a sprayed ITO layer.

For formation of a potential barrier on the porous p-InP surface, there was applied another material from the class of properly conducting electric current and solar-radiation-transparent oxides (TCO), namely, SnO_2. Thin layers of SnO_2 doped with antimony (SnO_2 : Sb) were sprayed on the nanoporous p-InP surface by the method applied for ITO layers. For this purpose, a 1 M mixture of solutions of tin and antimony chlorides in ethanol in a ratio of 11 : 2 was pulverized at a temperature of 400–450°C on the mentioned surface for not more than 60 s. The sprayed layers of SnO_2 : Sb were continuous, their electric conductivity provided by a concentration of electrons of 10^{20} cm^{-3} and their mobility up to 20 $cm^2/(V\ s)$ achieved values of 10^2 Ω^{-1} cm^{-1}. The SEM image of the nanoporous p-InP surface with the sprayed SnO_2 : Sb layer and results of the EDX analysis of the surface at the points marked with an "x" are shown in Fig. 3.

The results of the EDX analysis of the studied surface show that atoms of the elements constituting the compounds InP, SnO_2, and P_2O_5 are present in the space subjected to the EDX analysis. The rather high content of oxygen atoms, being inconsistent with the stoichiometric composition of the specified compounds, may be due to oxygen adsorption by the nanoporous p-InP surface.

A thin SnO_2 layer is formed not only on the porous InP surface but also in the volume of the nanopores, this signifies the effect of enlargement of the active surface of photoelectric structures due to the nanoporosity of the surface layer.

In Fig. 4b, the values of the ratio of the EDX analysis distances from the porous layer surface and depth of the porous layer boundary position in the InP crystal plate are plotted on the abscissa; the content (in atomic percent) of tin, phosphorus, and indium in the porous layer area subjected to the analysis is plotted on the ordinate. One can see that, while moving away from the surface of the porous InP layer, the content of tin and oxygen decreases and that of indium and phosphorus

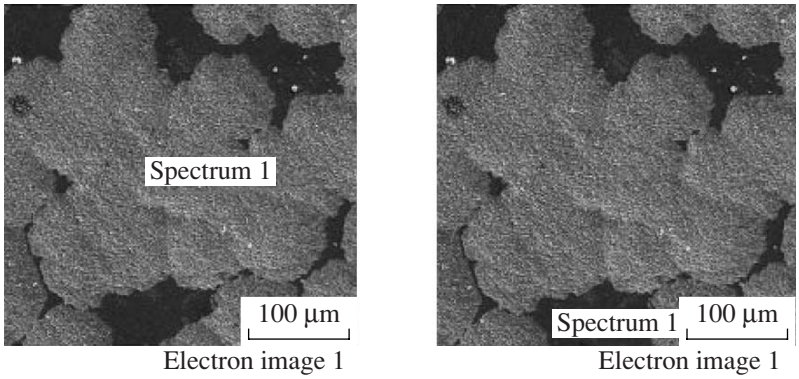

Spectrum 1			Spectrum 2		
Element	wt %	at %	Element	wt %	at %
O K	26.06	68.44	O K	22.82	60.51
P K	5.06	6.86	P K	11.21	15.35
In L	26.55	9.72	In L	46.91	17.33
Sn L	42.32	14.98	Sn L	19.05	6.81
Total	99.99	100	Total	99.99	100

Fig. 3. SEM image of the nanoporous InP surface with a sprayed SnO_2 : Sb layer and the results of the EDX analysis of this surface.

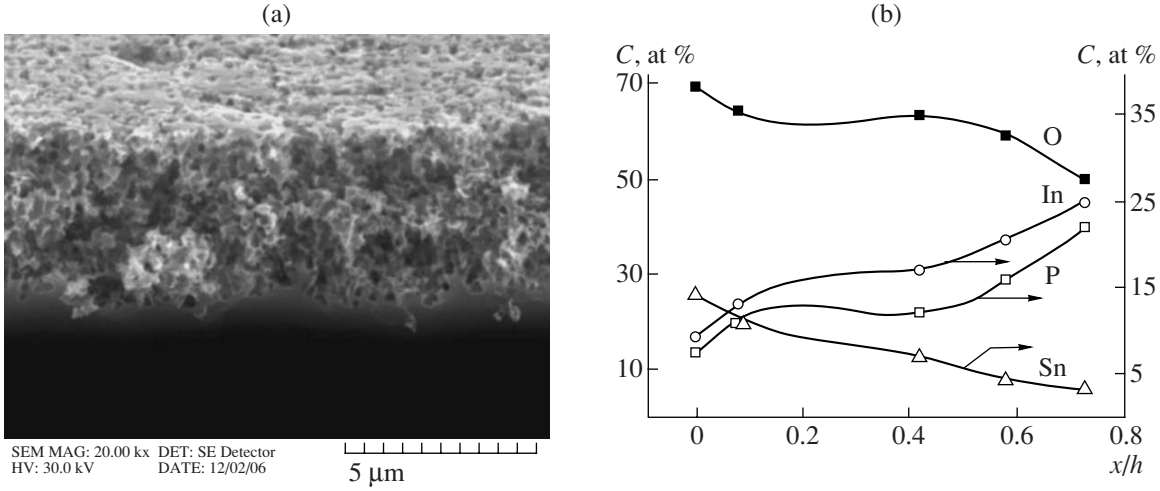

Fig. 4. Cross section of the nanoporous InP layer (a) and the distribution of chemical elements in the layer in the direction from the surface towards the depth of the sample (b).

increases. Tin in the region of the porous layer–bulk InP boundary (x/h = 0.8–1.0) is not found, while oxygen is present beyond this boundary, probably, due to simultaneous formation of the SnO_2 and P_2O_5 layers. At the values x/h = 1.1, oxygen in the InP volume is not found and the content of indium and phosphorus in atomic percent becomes strictly stoichiometric. Thus, we can conclude that a thin SnO_2 : Sb layer is formed not only on the surface of the porous InP layer, but also in its pores at a depth up to 4 µm (thickness of the electrochemically etched layer).

For research of the electric and photoelectric properties of the SnO_2 : Sb/nanoporous p-InP structure, there was prepared a sample, and its schematic representation is shown in Fig. 5.

The p-InP base plate was subjected to the electrochemical etching for porous layer formation so that a band about 2 mm wide remained electrochemically

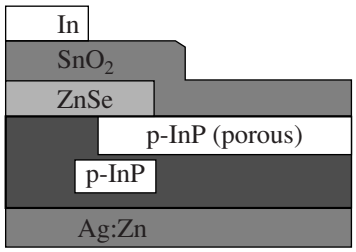

Fig. 5. Schematic representation of the SnO_2 : Sb/nanoporous p-InP structure.

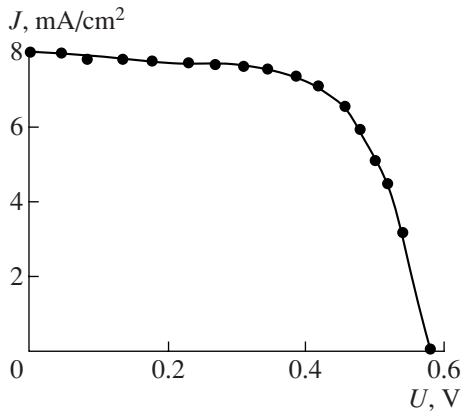

Fig. 6. Load CVC of the SnO_2 : Sb/nanoporous p-InP structure.

unetched on the plate edge. This band and the adjacent small part of the porous p-InP layer surface were coated with a thin layer of dielectric zinc selenide obtained by vacuum evaporation. Then, by the method of pulverization of alcoholic solutions of tin and antimony chlorides in the above described conditions, a thin layer of SnO_2 : Sb was sprayed on the ZnSe layer and the porous p-InP layer remained uncoated. The ohmic contacts for the prepared structure were the alloy Ag + 5%Zn and In. The alloy Ag + 5%Zn was thermally evaporated in vacuum in the form of a continuous thin layer on the free p-InP surface. In was deposited by the same method in the form of a contact grid on the surface of the SnO_2 : Sb layer. The contact grid on the SnO_2 : Sb layer surface was formed so that its teeth were located on the porous layer surface, and the indium metal strip connecting them was placed over the crystalline InP section that was not subjected to the electrochemical etching. After application of the ohmic contacts, for their formation, the studied structure was thermally treated in vacuum at a temperature of 350°C for 9 min. Thus, at the structure connection to the metering circuits through mechanical or other contacts, the nanoporous part of the subject of the research remained undamaged; the dielectric layer of zinc selenide reliably protected the registration of measurements from the SnO_2 : Sb contact with the crystalline p-InP.

Electric measurements have shown that the current dependence through the In/SnO_2 : Sb/nanoporous p-InP/Ag + 5%Zn on the applied voltage (CVC) has an asymmetric behavior, which may be described by the known expression [12]

$$J = J_0[(\exp qU/AkT) - 1],$$

where J is the current density, J_0 is the saturation current density, q is the electron charge, U is the applied voltage, A is constant, k is the Boltzmann constant, and T is the experiment temperature. The quantities of the electric parameters of the structure determined from the electric measurements have the following values: A = 1.5; $J_0 = 2 \times 10^{-7}$ A; $U_d = 0.7$ V.

The studied In/SnO_2 : Sb/nanoporous p-InP/Ag + 5%Zn structures are sensitive to illumination. The sensitivity range covers part of the solar radiation spectrum located in the wavelength interval $0.4\ \mu m \le \lambda \le 1.0\ \mu m$. The load characteristic of the structure as a photovoltaic cell at illumination from a standard incandescent lamp is shown in Fig. 6.

It follows from Fig. 6 that the potential barrier appearing at the interface of the SnO_2 layer and the porous p-InP layer effectively separates light generated charge carriers; this makes application of the In/SnO_2 : Sb/nanoporous p-InP/Ag + 5%Zn structures promising for development of photovoltaic cells with high efficiency due to the active surface being enlarged by nanostructuring.

The foregoing allows us to draw the following principal conclusions:

—The technology for nanostructuring of surfaces of indium phosphide with hole conductivity has been developed.

—Deposition of thin layers of metal oxides on nanostructured surfaces has peculiarities: continuous thin layers of ITO are not formed on the porous InP surface by the method of pulverization of alcoholic solutions of indium and tin chlorides; conglomerates of solidificated drops of In_2O_3 appear.

—Thin SnO_2 layers sprayed by the above mentioned method on the nanoporous InP surface are continuous, properly conduct electric current, and transparent for the visible solar radiation range.

—The technique of preparation and research of SnO_2/InP heterostructures with a porous surface of the interface has been developed.

—It has been shown that the studied heterostructures may be a basis for the design of photoelectric devices with an enlarged active effective area.

ACKNOWLEDGMENTS

This work was supported by the CRDF–MRDA, project no. MOE2–3062–CS–03.

REFERENCES

1. Gessert, T.A., Li, X., Wanlass, M.W., and Couts, T.J., Progress in the ITO/InP Solar Cell, *Second Int. Conf. Indium Phosphide and Related Materials*, Denver, USA, 1990, pp. 260–264.
2. Botnaryuk, V.M., Gorceak, L.V., Grigorieva, L.N., and Simashkevich, A.V., Radiation Degradation of Solar Cells Based on InP–CdS Heterojunction, *Sol. Energy Mater.*, 1990, vol. 20, pp. 359–365.
3. Adeeb, N., Kretsu I., Sherban, D., Sushkevich, V., and Simashkevich, A., Spray Deposited ITO–CdTe Solar Cells, *Sol. Energy Mater.,* 1987, vol. 15, no. 1, pp. 9–19.
4. Do Quoc Hung, Bobeico, E., Gorceac, L., Sherban, D., and Simashkevich, A., Solar Cells Based on SIS Structures, *Proc. Third Int. Workshop on Material Sciences*, Hanoi, 1999, part 1, pp. 56–59.
5. Gagara, L., Gorcheac, L., Radu, C., Sherban, D., and Simashkevich, A., Photovoltaic Converters of Solar Energy on the Base of SIS Structures, *Proc. Int. Conf. "Euro–Sun 96,"* Munchen, 1996, vol. 2, pp. 665–669.
6. Andronic, I., Gorceac, L., Simashkevich, A., Gagara, L., Potlog, T., and Sherban, D., InP Based Radiation Stable Solar Cells, *Proc. 2nd World Conf. on PV Solar Energy Conversion*, Vienna, 1998, vol. 1, pp. 249–252.
7. Singh, R. and Shewchun, J., A Possible Explanation for the Photovoltaic Effect in Indium Tin Oxide on InP Solar Cells, *J. Appl. Phys.*, 1978, vol. 49, pp. 4588–4591.
8. Ming Iong Tsai, Fahrenbruch, A., and Bube, R., Sputtering Oxide/Indium Phosphate Junctions and Indium Phosphate Surfaces, *J. Appl. Phys.*, 1980, vol. 50, pp. 2696–2705.
9. Schlier, U., Lockwood, D.J., Graham, M.J., and Schmuki, P., Pore Formation on p-Type InP(100), *Phys. Stat. Sol. (a)*, 2005, vol. 202, no. 8, pp.1446–1450.
10. Ulin, V.P. and Konnikov, S.G., Nature of Electrochemical Pore Formation Processes in $A^{III}B^{V}$ Crystals (Part I), *Fiz. Tekh. Poluprovodn.*, 2007, vol. 41, issue 7, pp. 854–866 [Semiconductors (Engl. Transl.), vol. 41, issue 7, pp. 832–844].
11. Simashkevich, A., Sherban, D., Bruk, L., Bobeico, E., Coval, A., Fedorov, V., and Usatyi, Yu., Spray Deposited ITO–nSi Solar Cells with Enlarged Area, *Proc. 20th European PV Solar Energy Conf.*, Barcelona, 2005, pp. 980–982.
12. Roderick, A.H., *Kontakty metal–poluprovodnik* (Metal–Semiconductor Contacts), Stepanov, G.V., Ed., Moscow: Radio i Svyaz', 1982 (Russian translation).

ISSN 1068-3755, Surface Engineering and Applied Electrochemistry, 2008, Vol. 44, No. 1, pp. 6–8. © Allerton Press, Inc., 2008.

ELECTRICAL PRECISION TREATMENT OF MATERIALS

Application of Surface Charge Lithography to Nanostructuring of GaN Epilayers[1]

V. Iu. Popa[a], O. Volciuc[a], I. M. Tiginyanu[a], A. Sarua[b], and P. Heard[b]

[a] *National Center for Materials Study and Testing, Technical University of Moldova, bulv. Stefan cel Mare 168, Chisinau, MD-2004 Republic of Moldova*

Institute of Applied Physics, Academy of Sciences of Moldova, ul. Academiei 5, Chisinau, MD-2028 Republic of Moldova

[b] *H.H. Wills Physics Laboratory, University of Bristol, Tyndall Avenue, Bristol, BS81TL United Kingdom*

e-mail: popa_sl@yahoo.com

Received December 3, 2007

Abstract—It is shown that treatment of GaN epilayers by a low energy low dose focused ion beam with subsequent photoelectrochemical etching represent an efficient tool for GaN nanostructuring. Direct "writing" of a surface negative charge trapped by radiation defects allows one to fabricate thin GaN walls with a thickness as low as 100 nm using focused ion beam treatment. The obtained results show that the undercut etching inherent to GaN etching through windows defined by surface charge lithography depends on the depletion length in the doped GaN material and does not occur in the structures below a critical size of 200 nm in our case.

DOI: 10.3103/S106837550801002X

INTRODUCTION

Recently, we demonstrated that low-energy Ar^+ ion beam treatment of n-GaN epilayers with subsequent photoelectrochemical etching (PEC) in an aqueous solution of KOH can be used for material microstructuring [1]. The low-energy ion beam treatment creates surface defects that trap electrons, thus generating a surface layer of negative charge. The ion-beam-induced surface layer of trapped negative charge shields the GaN against PEC etching. The new approach is called surface charge lithography (SCL), taking into account the possibility to design and exploit the surface charge trapped by ion-beam-induced radiation defects as a lithographic mask for the purpose of manufacturing GaN mesostructures [1]. We found that the mesostructures fabricated by using ion beam treatment with subsequent PEC etching of n-GaN epilayers exhibit an undercut of about 200 nm determined by the hole diffusion length [1]. The reason is that, due to lateral diffusion of minority carriers, partial etching occurs under the mask, which is the top area damaged by the ion beam. The undercut etching made questionable the ability to fabricate GaN mesostructures with transverse dimensions less then the hole diffusion length. In this work, we demonstrate the possibility to fabricate GaN nanowalls with transverse dimensions as low as 100 nm using direct "writing" of protective masks by a focused ion beam (FIB) with subsequent subjection of the samples to photoelectrochemical etching in an aqueous solution of KOH.

[1] The text was submitted by the authors in English.

EXPERIMENT

The GaN layers used in our experiments were grown by low-pressure metalorganic chemical-vapor deposition (MOCVD) on (0001) c-sapphire. A buffer layer of about 25-nm-thick GaN was first grown at 510°C. Subsequently, a 0.5-μm-thick n-GaN film followed by an Si-doped n^+-GaN film and a top n-GaN layer with a 2.0 μm thickness each were grown at 1100°C. The concentration of free electrons in the top n-GaN layer was 1.7×10^{17} cm^{-3}, while the density of the threading dislocations was in the range of 10^9–10^{10} cm^{-2}.

An FEI Strata FIB 201 focused ion beam system was used for exposure of the gallium nitride samples. This instrument produces a focused gallium ion beam of 30 keV energy with beam currents in the range of 1 pA to 12 nA and corresponding beam diameters of 8 nm to 500 nm. For the exposure of the gallium nitride here, a beam current of 150 pA was used. The exposure pattern was created in a bitmap form with a 1024 × 1024 pixel format covering an area of 122 μm square on the sample. An exposure time of 1 μs per pixel gave a total exposure time for the pattern of 0.48 s and a corresponding exposure dose of 6.6×10^{12} cm^{-2}. Stopping range calculations predict the main projection range of the Ga ions in the GaN layer at about 14 nm under these conditions.

PEC etching was carried out in a stirred 0.1 mol aqueous solution of KOH under in situ UV illumination provided by focusing the radiation of a 350 W Hg lamp on a spot about 5 mm in diameter on the GaN surface exposed to the electrolyte. No bias was applied to the sample during the etching. The morphology of the

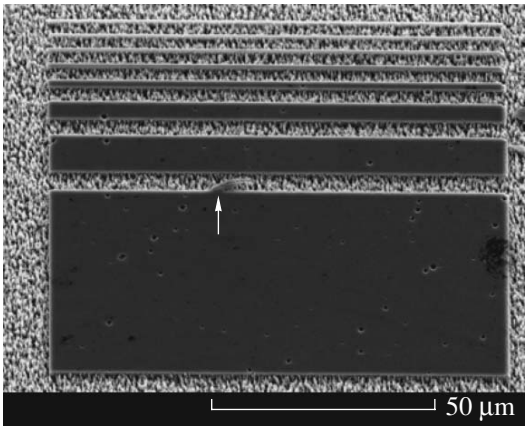

Fig. 1. SEM image taken from an n-GaN sample subjected to FIB treatment followed by PEC etching for 30 min. The dimensions of the mesostructures (from the top to bottom) are the following in μm^2: 100×0.1, 100×0.2, 100×0.5, 100×1, 100×2, 100×5, 100×10, and 100×50. A featherlike extension is marked by the white arrow (see the text for details).

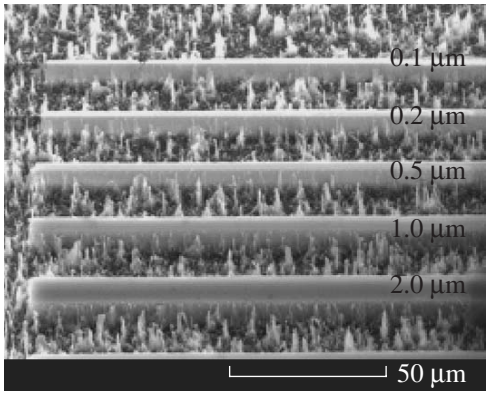

Fig. 2. SEM image taken of an n-GaN sample subjected to FIB treatment followed by PEC etching for 60 min. The dimensions of the mesostructures (from the top to bottom) are the following in μm^2: 100×0.1, 100×0.2, 100×0.5, 100×1, and 100×2.

etched samples was studied using a TESCAN scanning electron microscope (SEM) operating at 20 keV.

Micro-Raman measurements were performed using a Renishaw InVia spectrometer and a 488 nm laser line of an Ar^+ ion laser. The laser beam was focused on the sample surface using a 50× microscope lens onto a spot 0.5–0.7 μm in diameter. The micro-Raman spectra were recorded at room temperature using back-scattering geometry.

Before the PEC etching, selected GaN surface areas with dimensions of 100×0.1, 100×0.2, 100×0.5, 100×1, 100×2, 100×5, 100×10, and 100×50 μm^2 were uniformly treated with the focused ion beam. Figure 1 shows an SEM image taken from a surface region subjected to FIB treatment followed by PEC etching for 30 min.

It is evident that only the areas not subjected to the ion beam treatment are vulnerable to photoelectrochemical attack. In the etched areas, whiskers representing the remaining GaN material containing threading dislocations [1–3] can be easily distinguished. At the same time, the FIB treated areas prove to be resistant to PEC attack in spite of the fact that these areas exhibit some micrometer-size defects related to the growth process. The featherlike extension (marked by the white arrow) of the rectangle with dimensions of 100×50 μm^2 is likely to be associated with a mechanical scratch on the surface, which can make GaN resistant to PEC etching as well [1].

The advantage of low-energy focused ion beam writing combined with PEC etching is that it allows one to easily create nanostructures, which are in practice limited by the resolution of the ion beam system. It is rather spectacular that this maskless approach leads to the formation of thin walls with a thickness as small as 100 nm. The 100-nm thick walls are bright in SEM images due to charging phenomenon. The observation of charging phenomenon is indicative of low conductivity of the wall, which may be caused by the depletion of free carriers. It is known that the Fermi level at the surface of n-GaN is pinned at 0.5–0.7 eV below the bottom of the conduction band [4, 5], and this phenomenon leads to the formation of the depletion space charge layer of about 70 nm for the n-type doping level in our samples. Taking this into account, one may assume that the surface depletion layers related to the two lateral sides of the 100-nm thick wall merge resulting in poor wall conductivity.

The SEM image in Fig. 2 illustrates a region subjected to FIB treatment followed by PEC etching for 60 min. The analysis shows that the height of the GaN walls in this image is higher than the height of the walls formed after etching for 30 min (Fig. 1). Note the reduced density of the whiskers in the areas between the GaN walls in Fig. 2 in comparison with that inherent to such areas in Fig. 1. Most remarkably, note that no undercut etching is observed in the case of very thin GaN structures fabricated by surface charge lithography.

As one can see from Fig. 2, the morphology of the 2-μm width mesostructure reflects the impact of undercut etching (the charging effect allows one to visualize the undercut in SEM images as bright periphery areas of the mesostructures [1]), while the 100-nm wide nanowall exhibits no traces of the undercut. One may conclude that, in structures below a critical width defined by the FIB-induced surface charge mask, no undercut etching occurs. Such critical width seems to be defined as twice the extension of the surface depletion layer width. Note that, for n-GaN with a free electron concentration on the order of 10^{17} cm^{-3}, the depletion space charge layer is about 70 nm. Under such conditions, the 100-nm thick walls are fully depleted of

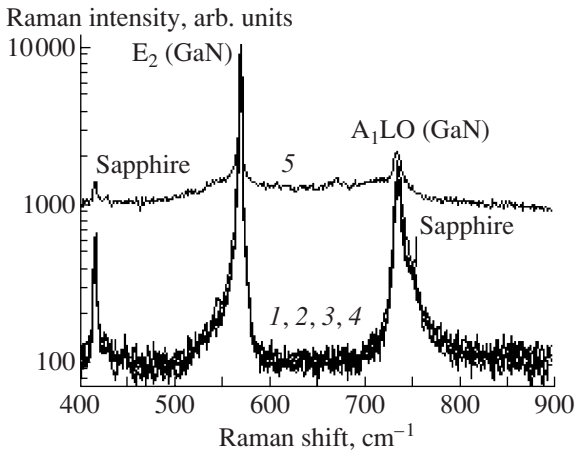

Fig. 3. Raman scattering spectra of n-GaN samples subjected to FIB treatment at different doses in cm^{-2}: *1*—as-grown, *2*—6.6×10^{11}, *3*—6.6×10^{12}, *4*—8.0×10^{13}, and *5*—7.7×10^{14}.

free carriers and therefore cannot support current flow. Taking into account that current flow is essential for the PEC etching process, it is clear that the undercut etching will not take place in spite of the fact that the minority carrier diffusion length can reach values as high as 200 nm [1]

To estimate the degree of crystal lattice disorder induced by FIB processing, we studied micro-Raman scattering spectra of n-GaN samples subjected to FIB treatment at doses of 6.6×10^{11}, 6.6×10^{12}, 8.0×10^{13}, and 7.7×10^{14} cm^{-2}. The Raman spectra in Fig. 3 show two allowed Raman modes of 0001-oriented GaN material, namely, E_2 and A_1LO at 569 and 735 cm^{-1}, respectively. Since GaN is transparent to the 488 nm excitation, the modes of the sapphire substrate are visible at 418 and 750 cm^{-1}.

The spectra of samples irradiated with ions at doses of up to 8.0×10^{12} cm^{-2} are practically identical to that of the as-grown n-GaN specimen. Taking into account that the frequency and width of the phonon bands in the Raman spectra of semiconductor compounds are dependent upon the amount of the crystal lattice damage [6], one may conclude that the ion beam treatment at doses up to 8.0×10^{13} cm^{-2} generates lattice point defects at relatively low densities limited to the surface region of the GaN layer (about 15 nm in our case). The crystalline quality of the material as a whole is negligibly disturbed. According to the data presented in Fig. 3, only the highest dose of irradiation, i.e., 7.7×10^{14} cm^{-2}, leads to pronounced changes in the Raman spectrum. The visible 488 nm excitation normally penetrates the whole thickness of the 2.5 μm thick GaN layer; however, implantation of Ga ions at doses above 10^{13} cm^{-2} reduces the optical penetration depth of the laser beam and the Raman signal becomes more sensitive to the ion bombardment damage on the surface. Note the reduced intensity ratio between the GaN and the sapphire substrate peaks.

Thus, surface charge lithography proves to be an efficient tool for both micro- and nanostructuring of gallium nitride. Moreover, in the case of fabrication of nanostructures with transverse dimensions equal to or less than the double surface depletion layer, no undercut etching related to the minority carrier diffusion occurs. We believe that further improvement of GaN growth technology will allow one to fabricate high quality nanostructures by maskless FIB direct writing with subsequent PEC etching.

ACKNOWLEDGMENTS

This work was supported by the Supreme Council for Research and Technological Development of Moldova.

REFERENCES

1. Tiginyanu, I.M. et al., Surface-Charge Lithography for GaN Microstructuring Based on Photoelectrochemical Etching Techniques, *Appl. Phys. Lett.*, 2005, vol. 86, pp. 174102–174105.
2. Youtsey, C. et al., Rapid Evaluation of Dislocation Densities in n-Type GaN Films Using Photoenhanced Wet Etching, *Appl. Phys. Lett.*, 1999, vol. 74, pp. 3537–3539.
3. Weyher, J.L. et al., Selective Photoetching and Transmission Electron Microscopy Studies of Defects in Heteroepitaxial GaN, *J. Appl. Phys.*, 2001, vol. 90, pp. 6105–6109.
4. Segev, D. and Van de Walle, C.G., Origins of Fermi-Level Pinning on GaN and InN Polar and Nonpolar Surfaces, *Europhys. Lett.,* 2006, vol. 76, pp. 305–311.
5. Kočan, M. et al., Surface Potential at as-Grown GaN(0001) MBE Layers, *Phys. Status Solidi B*, 2002, vol. 234, pp. 773–777.
6. Sarua, A. et al., Raman Spectroscopy of Porous and Bulk GaP Subjected to MeV-Ion Implantation and Annealing, *J. Appl. Phys.*, 2000, vol. 88, pp. 7006–7012.

ISSN 1068-3755, Surface Engineering and Applied Electrochemistry, 2008, Vol. 44, No. 1, pp. 9–14. © Allerton Press, Inc., 2008.
Original Russian Text © T.V. Bortsoi, 2008, published in Elektronnaya Obrabotka Materialov, 2008, No. 1, pp. 14–20.

ELECTRICAL SURFACE TREATMENT METHODS

Estimation of Distributed Parameters at Electrochemical Deposit Formation

T. V. Bortsoi

Institute of Applied Physics, Academy of Sciences of Moldova, ul. Academiei 5, Chisinau, MD-2028 Republic of Moldova
e-mail: bortzoi_tudor@yahoo.com

Received July 23, 2007

Abstract—This work presents a system created for the purpose of research of the process of electrochemical deposit formation based on methodological tools of estimation of the distributed parameters, being an integrated unity characterized by internal relations. It is established that the system elements representing the general and particular attributes are levels of electrochemical objects, principles, techniques, methods, and devices for estimation of distributed parameters. They are characterized by a high generality with elements of similar systems of research from other fields of knowledge. An important feature and advantage of the proposed system of research is the possibility to study the laws of the process of formation of electrochemical deposits at various levels of electrochemical objects with application of methods, techniques, and devices of estimation of distributed parameters adopted from electrochemistry and other fields of knowledge. The system opens possibilities for further development, enhancement, deepening, and transition to new steps of perfection of theoretical and experimental research of electrochemical deposits, thus increasing the level of accuracy and reliability of the obtained results.

DOI: 10.3103/S1068375508010031

The complexity and variety of factors influencing the process of formation of electrochemical compositional and other deposits determine the necessity of practical research of the interaction between the electrochemical system parameters and deposit characteristics. One of the methodological tools for investigation of the process of formation of electrochemical deposits (ED) is the estimation of its distributed parameters (DP) [1–4, etc.].

Let us note that DP include indexes for which there appear derivatives with respect to at least one of the coordinates and possibly to all three.

At present, for research of different levels of electrochemical objects, in electrochemistry numerous principles, methods, and devices are applied [1–13, etc.], which are characterized by different methodological tools of DP estimation. However, the methods of DP estimation are not considered to be an integrated research theory with internal relations between its different parts and its components (especially, in the context of the electrodeposition processes).

Therefore, there appear certain difficulties in the enhancement of the possibilities of description, prediction, and control of the ED formation process, as well as improvement and development of methods, techniques, and devices for DP estimation [14, etc.] at different levels of electrochemical objects.

In our opinion, further development and enhancement of theoretical and experimental research of the ED formation process may be realized on the basis of an integrated theoretical system of DP estimation that is characterized by internal relations between the general and the particular and the individual and the integral.

It should be noted that, in some fields of science, DP estimation is considered as a subject of research and it is studied with application of some auxiliary (interdisciplinary) branches of science [15–17, etc.], for example, statistical physics [15], biometrics [16], and econometrics [17].

A theoretical system of ED research may be formed on the basis of the levels of electrochemical objects, principles, methods, techniques, and devices of DP estimation developed by us [1–7] and other researchers [8–13, etc.].

Thus, the most favorable system for ED research is the one characterized by the DP estimation methodological tool, which may play the role of connecting attributes (links) for units of its components representing levels of electrochemical objects, principles, methods, techniques, and devices, being particular attributes of the system.

Let us consider general and particular attributes of the DP estimation electrochemical system and its elements in detail (see Fig. 1).

Levels of research of electrochemical objects are particular attributes of certain quantity of the system units, for example, macro- and microprofiles of the electrode [1, 4, 8–10, etc.], the micro- and nanolevel of the deposit composition [2, 3, 8, 11, 12], the interface level [13], etc. They are also general attributes for cer-

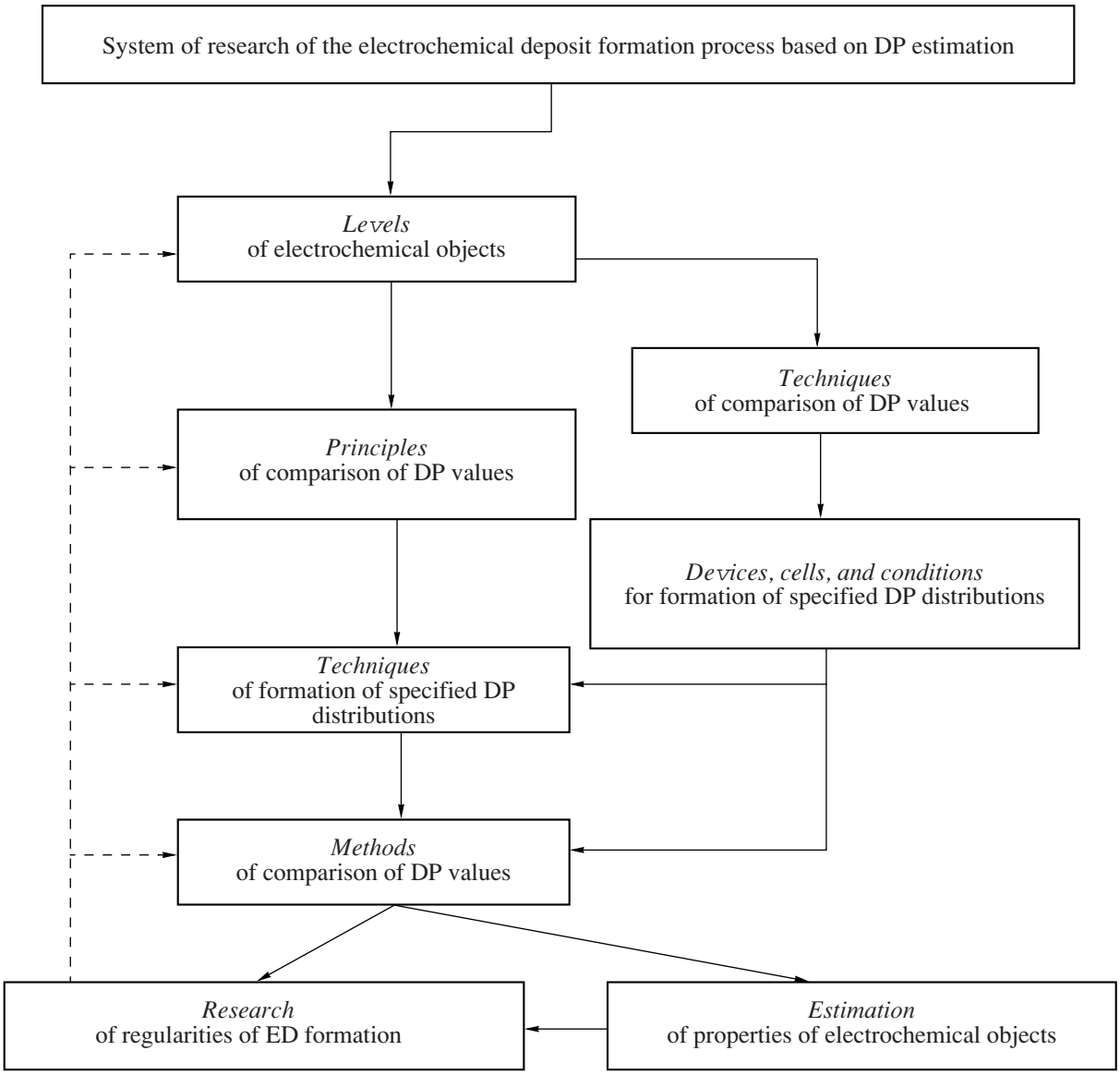

Fig. 1. Structural flowchart of the system of research of the electrochemical deposit formation process based on the estimation of distributed parameters.

tain quantities of the system units, being principles, methods, techniques, and devices for DP estimation.

Thus, the electrochemical object levels play the role of subsystems; they are components (units) of the electrochemical research system. Besides, each level of the electrochemical object research may be characterized, at least, by two attributes of subsystems. One of them reflects the principles of comparison of the DP values, and the other characterizes the techniques of formation of specified distributions of DP values.

For example, comparison of DP values may be realized on the principles of comparison of mean values [2, 3, 8–13], relative values [8–13], relative deviations of values [1–4], mutual distributions of values [2, 3, 8, 9], etc. Values of DP of a certain level of the research may be formed by their directed distribution [5–10], extreme distribution [9, 10], or by other variants.

Let us note that, as the system element, the category "principle" implies a basis of operations on values of DP of ED for their comparison.

Techniques of comparison of DP values are particular attributes for the subsystem of principles of comparison of values. Simultaneously, they are general attributes for certain quantities of methods of DP estimation. Thus, techniques of comparison of DP values play the role of a subsystem for the comparison principles. For example, on the basis of the relative deviations t_i and δ_j, there have been developed techniques of quantitative comparison of DP values at the macrolevel (macroprofile) expressed by the indexes A_B, C_B, E_B, and

H_B. The techniques of qualitative comparison of DP values at the macrolevel are formed on the basis of relative values of the electrode (characterized by certain relations between the deviations t_i and δ_j) expressed by the indexes B_B, D_B, F_B, and G_B [1, 4].

Techniques of formation of specified distribution of DP values are particular attributes of subsystems of the research levels. Simultaneously they are general attributes for certain quantities of devices, cells, and conditions of electrolysis. Thus, techniques of formation of specified distributions of DP values play the role of subsystems. For example, elements (units) of the subsystem are devices for formation of directed distribution of values of DP of ED [1, 4], cells, and conditions of electrolysis for relative estimation of the micro- and macrodiffusing power of electrolytes [1, 4], etc.

Primary elements of the system, or its basic units, are methods of DP estimation; on their basis, one can research properties of electrochemical objects and regularities of the ED formation process.

Research of regularities of ED formation makes it possible to reveal new levels; to develop new principles, techniques, methods, and devices for DP estimation; and to transit to new stages and variants of research of their formation regularities.

Therefore, the electrochemical system of DP estimation has the property of enhancement, development, and transition to new stages of ED research. Besides, it is characterized by functions of more profound and comprehensive description of the formation process and prediction of their properties [1–4].

Analysis of the structural flowchart of the electrochemical system of DP estimation allows us to find that its characteristic peculiarity and advantage is the possibility to research regularities of ED formation process at different levels of electrochemical objects with application of laws, methods, techniques, and devices adopted from electrochemistry, mathematics, mathematical statistics, and other fields of knowledge. Thereby, on its basis, it is possible to systematize and get necessary information for suggestion, confirmation, and improvement of some fields of knowledge and electrochemical theories.

The properties, sphere of possible application, and significance of the theoretical structure of the system may be revealed on the basis of analysis, for example, of one of its most general subsystems—the level of the electrode macroprofile. At this level, it is common practice to compare DP values mainly on the principle of relative value comparison [8–13].

However, this may be realized more efficiently with application of the principles developed by us of comparison of relative deviations determining quantitative and qualitative characteristics of DP comparison techniques [1, 4].

These techniques are based on comparison of values of the relative deviations t_i and δ_j of one DP with respective values of other distributed parameters or based on determination of rates of geometrical dimensions of the electrode parts with certain relations between them [1, 4].

On the basis of the described techniques of DP comparison, we have developed a number of methods for estimation of the relations between DPs, including A_B, A'_B, B_B, B'_B, C_B, C'_B, D_B, D'_B, E_B, F_B, H_B, G_B, γ_B, and η_B, which allow research of various aspects of the electrodeposit formation process with a high degree of reliability [1, 4].

The macrolevel, being one of the categories of the ED research system, is also characterized by techniques of formation of specified distributions of DP values, for example, directed ones.

A group of researchers studying processes of formation of directed distribution of DP values developed a number of devices, cells, and conditions of deposit obtaining [5–10].

For example, they have designed new types of devices (Figs. 2a, 2b, and 2c) such as an open electrolyzer with the anode and cathode spaces separated by a vertical partition [5–7]. The partition forms horizontal connecting spaces with the electrolyte level and the electrolyzer bottom.

In these devices, it is possible to place electrodes in various zones of the electrolyzer and to change their position relative to each other and to the separating partition; this allows increasing the number of variants for research of the process of electrochemical composite material (ECM) formation.

With the purpose of ECM obtaining and experimental testing of techniques of formation of directed distributions of DP values, there has been developed a device (see Fig. 2a) [5, 6] consisting of a vertical anode and an open electrolyzer (1) with bottom (2), anode space (3) and cathode space (4). The spaces are partially separated by partition (5), which forms gaps with electrolyte level (6) and electrolyzer bottom (7). Partition (5) is applied for creation of conditions for formation of directed distributions of DP of ECM. The device allows studying separated ascending and descending flows of electrolyte–suspension. For more uniform distribution of hydrodynamic flows in the cathode space, electrolyzer bottom (2) is made in the form of an eccentric pocket with small wall (8) under anode space (3) and with large wall (9) under cathode space (4). In anode space (3), there are positioned thermostat control elements (10), mechanism for electrolyte–suspension circulation (11), and elements (12) for uniform flow distribution over the cell width. In space (4), there are positioned cathode (13); elements (14) for flow stabilization in the circumcathode region; and elements (15) and (16) for the flow leveling in the cathode space, which consist of guide vanes and a grid, respectively.

The described device operates as follows. Mechanism (11) forms the electrolyte flow circulating through anode space (3) and cathode space (4). In the bottom

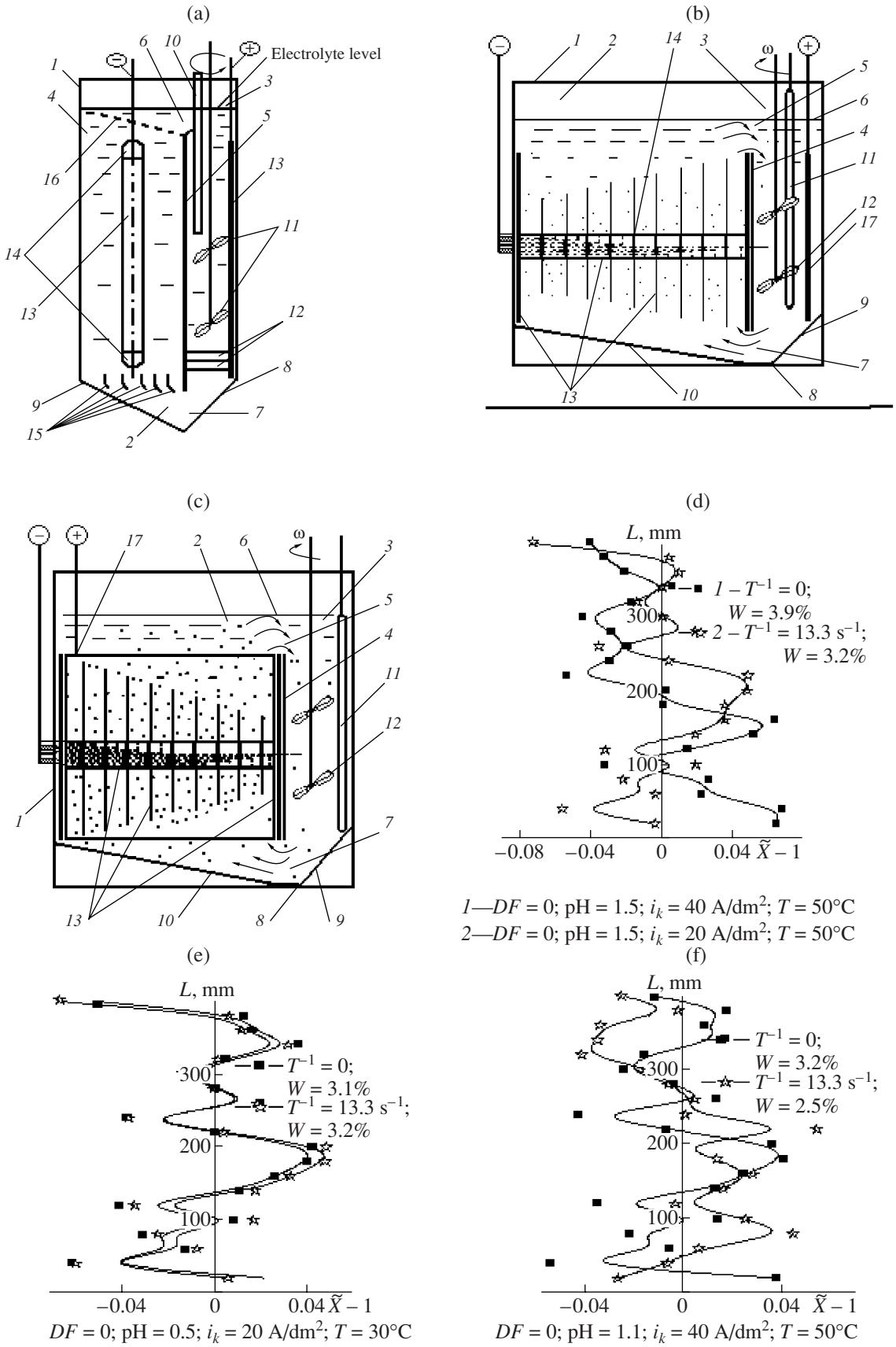

Fig. 2. Devices (a), (b), and (c) for ECM research and distributions in the cell (a) and along the cathode length of relative values $\tilde{x}$ for iron deposits (d), (e), and (f).

part of the anode space, the flow is uniformly distributed by elements (12) across the width of the bottom part of cathode space (3). From the bottom part of cathode space (3), the electrolyte–suspension flow is uniformly and homogeneously distributed in the cathode space with the help of guide vanes (15) and grid (16).

The design advantages of one of the devices shown in Fig. 1a allowing improvement of methods of the ECM research were estimated according to the experiment results obtained under various electrolysis conditions by determination of the influence of the flow rate, the uniformity of the DF particle distribution in the electrolyte, and the degree of distribution of the iron deposit amount on the cathode surface.

The presented experimental data (see Figs. 2d, 2e, and 2f) show the influence of the iron deposition modes on the distribution of the deposit volume along the cathode length, the intensity of the electrolyte stirring T^{-1}, and the coefficient of variation W of the iron deposit amount. For the given conditions of the experiments, the coefficient of variation is calculated by the formula [15]

$$W = (s_x/\bar{x}) \times 100\%, \quad (1)$$

where s_x is the standard deviation of the statistical population X, and $\bar{x}$ is the mean value of the statistical population X.

For a more illustrative estimation of the experiment results, values of the distributed volumes in Figs. 2d, 2e, and 2f are shown in relative quantities $\tilde{x}_i - 1$, where $\tilde{x}_i = x_i/\bar{x}$. Curve *1* shows the iron deposit distribution in conditions of the electrolyte stirring, curve *2*—without stirring.

As one can see from the experiment results (Figs. 2d, 2e, and 2f), irrespective of the hydrodynamic mode and the conditions of the electrolysis, the uniformity of the iron volume distribution along the cathode length (400 mm) does not exceed W_m = 2.5–3.9% and confirms the higher uniformity in comparison with known analogous devices.

For the study of the influence of the hydrodynamic modes, the directivity, the rate of the flow, the force, the concentration fields, and other factors, the designed device with a horizontal cathode has been applied (see Figs. 2b and 2c) [7]. It differs from the above-described one in the fact that separating partition (4), cathode (14), and plates (13) form the cathode block (see Fig. 2b).

This hydrodynamic system allows redistribution and control of the electrolyte flow to each cathode part by formation of equal (see Fig. 2b) or different (see Fig. 2c) rates of flow in their region. For research of the influence of the hydrodynamic mode or the electrolyzer design peculiarities on the deposit formation process, the anode may be positioned in the cathode block space.

Thus, the presented devices allow formation at the electrode macrolevel (macroprofile) of conditions for directed distribution of values of the main indexes of the ED deposition process, for example, for primary and secondary distributions of the current density, flow rates, disperse phase quantity, etc.

The validity and applicability of the system of DP estimation may be revealed by analysis of the generality of its constituents and elements of analogous research systems from other fields of knowledge. For example, its methods may be characterized, at least, by three steps of generality.

The most general methods applied to a wide variety of procedures of DP research are the methods of DP relation research at the macrolevel (A_B, B_B, C_B, D_B, E_B, F_B, H_B, G_B, γ_B, η_B [1], A'_B, B'_B, C'_B, D'_B [4], etc.). These methods are based on general statistical laws; they include such categories as statistical units, population, complex, deviation, relative parameters, etc.

Methods of the mean degree of generality, which are sometimes called "medium-range methods" and applied to a small subset of problems of various fields, are the methods of DP research at the microlevel ($\bar{S}$, $\bar{\bar{S}}$, S_B, N_S, $\bar{p}_V$, V_B, N_k [2, 3], etc.), since they are applicable for DP research for many classes of periodic media.

The lowest degree of generality concerning the solution of a narrow class of problems includes the methods of formation of conditions for relative research of DPs at the macro- and microlevel applied for estimation of the diffusing power of the electrolyte and other properties of electrochemical objects [8, 9, etc.].

Thus, the proposed system of DP estimation gives the possibility to research the degree of influence of various electrolysis factors on the regularities of the process of ECM formation by estimation of the relations between the DPs; to reveal the properties of some objects of the electrochemical system, for example, the electrolyzers and the macro- and microdiffusing power of the electrolyte; or to form the functional structure of the ED; etc.

CONCLUSIONS

1. The system developed in order to research the electrochemical deposit formation process based on methodological tools of estimation of the distributed parameters is an integrated unity characterized by internal relations.

2. The elements of the system representing general and particular attributes are levels of electrochemical objects, principles, techniques, methods, and devices for estimation of the distributed parameters. They are characterized by high generality with elements of analogous research systems from other fields of knowledge.

3. An important peculiarity and advantage of the presented system is the possibility to research regularities of the process of electrochemical deposit formation at various levels of electrochemical objects with appli-

cation of methods, techniques, and devices of estimation of distributed parameters adopted from electrochemistry and other fields of knowledge.

4. The system opens possibilities of further development, enhancement, deepening, and transition to new stages of improvement of theoretical and experimental research of electrochemical deposits, thus increasing the degree of accuracy and reliability of the obtained results.

REFERENCES

1. Bortsoi, T., Statistical Methods of Estimation of Relation between Electrochemical System Parameters with Distributed Values on the Electrode, *Elektron. Obrab. Mater.*, 2006, no. 4, pp. 24–36.
2. Bortsoi, T., Structural Estimation of Electrochemical Composite Materials, *Elektron. Obrab. Mater.*, 2005, no. 5, pp. 20–23.
3. Bortsoi, T., Characteristics of Disperse Phase Distribution in Electrochemical Composition, *Elektron. Obrab. Mater.*, 2006, no. 6, pp. 10–14.
4. Bortsoi, T., Possibilities of Development of Statistical Methods of Estimation of Distributed Parameters of Electrochemical Deposits at Macrolevel, *Elektron. Obrab. Mater.*, 2007, no. 5, pp. 67–74.
5. Bortsoi, T., MD Inventor's Certificate no. 1674, *BOPI*, 2001, no. 5.
6. Bortsoi, T., MD Inventor's Certificate no. 2530, *BOPI*, 2004, no. 8.
7. Bortsoi, T., MD Inventor's Certificate no. 2778, *BOPI*, 2005, no. 5.
8. Gamburg, Yu.D., *Elektrokhimicheskaya kristallizatsiya metallov i splavov* (Electrochemical Crystallization of Metals and Alloys), Moscow: Yanus–K, 1997.
9. *Spravochnoe rukovodstvo po gal'vanotekhnike* (Reference Manual on Electrodeposition), Lainer, V.I., Ed., Moscow: Metallurgiya, 1972, part 1.
10. Bobanova, Zh.I., Yushchenko, S.P., Yakovets, I.V., Yakhova, E.F., and Dikusar, A.I., Determination of Diffusing (Localizing) Power of Electrolytes at Electrochemical Treatment with Application of Hull Cell with Rotating Cylindrical Electrode, *Elektron. Obrab. Mater.*, 2000, no. 6, pp. 1–15.
11. Dikusar, A., Globa, P., Redkozubova, O., Sidelnikova, D., Sirbu, L., Vieru, V., and Tiginyanu, I., Kinetics of Metal Deposition in the Process of Electro Less Fabrication of Porous InP–Cu Nanocomposite, *Electrochem. Sol. State Lett.*, 2005, 8(3), pp. 51–53.
12. Dikusar, A.I., Globa, P.G., Redkozubova, O.O., Sidel'nikova, S.P., Syrbu, L., and Tiginyanu, I.M., Kinetics of Metallization and Diffusing Power of Electrolytes at Obtaining of Nanocomposites Based on $A^{III}B^{V}$, *Elektron. Obrab. Mater.*, 2005, no. 5, pp. 4–9.
13. Tochitskii, T.A., Fedosiuk, V.M., and Kasyutich, O.I., On Mechanism of Formation of Structure and Internal Stresses in Multilayer Co/Cu–Films, *Elektrokhimiya*, 1996, vol. 32, no. 6, pp. 769–773.
14. Mihai, N., *Introducere in filozofia si metodologia stiintei* (Introduction in Philosophy and Methodology of Science), Chisinau: ARS, 1996.
15. Klimontovich, Yu.L., *Statisticheskaya fizika* (Statistical Physics), Moscow: Nauka, 1982.
16. Lakin, G.F., *Biometriya* (Biometrics), Moscow: Vysshaya Shkola, 1990.
17. Zaman, C., *Econometria* (Econometrics), Pro Democraia, 1998.

ISSN 1068-3755, Surface Engineering and Applied Electrochemistry, 2008, Vol. 44, No. 1, pp. 15–22. © Allerton Press, Inc., 2008.
Original Russian Text © V.F. Gologan, Zh.I. Bobanova, S.Kh. Ivashku, G.F. Volodina, V.A. Mazur, B.M. Pushkash, 2008, published in Elektronnaya Obrabotka Materialov, 2008, No. 1, pp. 21–28.

ELECTRICAL SURFACE TREATMENT METHODS

Morphology of Electrolytic Copper Coatings at Application of a Power Supply with an Induction–Capacitance Device

V. F. Gologan[a], Zh. I. Bobanova[a], S. Kh. Ivashku[a], G. F. Volodina[a], V. A. Mazur[b], and B. M. Pushkash[b]

[a] *Institute of Applied Physics, Academy of Sciences of Moldova, ul. Academiei 5, Chisinau, MD-2028 Republic of Moldova*
e-mail: bobanova@phys.asm.md

[b] *Center of Metrology and Automation of Scientific Research, Academy of Sciences of Moldova, ul. Academiei 3, Chisinau, MD-2028 Republic of Moldova*

Received August 17, 2007

Abstract—Varying the parameters of the inductance–capacitance device, as well as varying the solution composition and current density, allows obtaining copper coatings with an original surface morphology.

DOI: 10.3103/S1068375508010043

In earlier published works, peculiarities of the electrochemical process of coating deposition in the case of application of inductance–capacitance devices (ICD) have been mentioned [1, 2]. It has been shown that, at variation of the device parameters (inductance and capacitance), the cathode potential may shift towards both a more positive and a more negative range. Thus, there appears the possibility to control the electrochemical process by varying the device parameters L and C with the other electrolysis conditions (the composition and temperature of the electrolyte, current density, etc.) maintained constant.

A correlation between the current density, electrode potential, and spectrum characteristics of the alternating components has been found. At the values of L and C that cause the greatest shift of the cathode potential towards the more positive range, the amount of the spectrum components and the frequency range width grow; their amplitude increases by a factor of 1.5–2 [2].

These conditions of electrolysis favor increasing of the current density and, therefore, the process efficiency. Besides, at optimal deposition conditions, coatings with a more perfect structure and improved physicomechanical properties have been obtained [1].

At the ICD influence on the process of copper deposition from a sulfate electrolyte (250 g/l $CuSO_4 \cdot 5H_2O$, 50 g/l H_2SO_4), the cathode potential varies over a wide range (~100 mV at i_k = 10 A/dm^2); this significantly influences the morphology and structure of the coatings [2]. However, these experiments have been carried out at deposition with a restricted range of variation of the conditions.

Taking into account the widespread use of electrodeposited copper coatings in industry, for increasing the amount of data on the influence of the above mentioned device parameters and electrolysis conditions on the formation of deposits, additional research has been carried out.

EXPERIMENTAL

Coatings were deposited from sulfate (nos. 1–3) and hydrofluoboric electrolytes (no. 4) at the current densities i_k = 1–10 A/dm^2 and the solution temperature 20°C (table).

As well as in the previous research, for the coating deposition, there was used a power supply consisting of a single-phase 40-W transformer, a rectification block,

Composition of the studied electrolytes

Consecutive number	Component composition, g/l				
	copper sulfate	sulfuric acid	copper fluoborate	boric acid	hydrofluoboric acid (free)
1	250	50	–	–	–
2	112	159	–	–	–
3	50	450	–	–	–
4	–	–	35–40	15–20	15–18

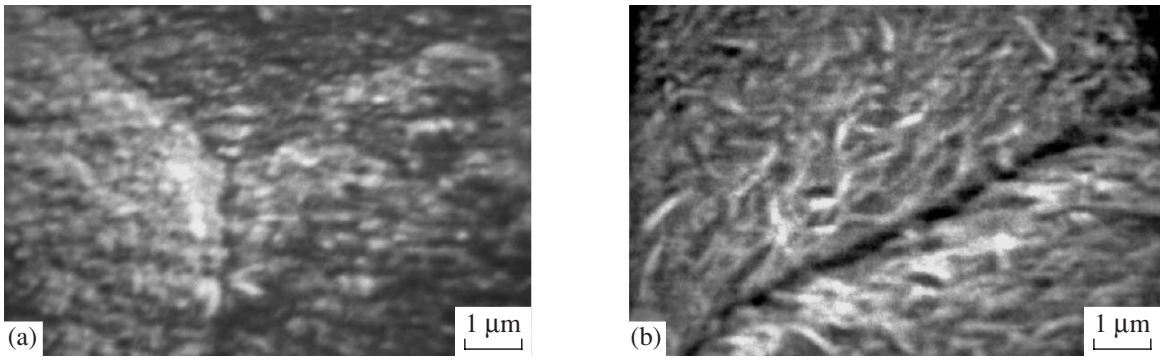

Fig. 1. Morphology of the surface of the coatings obtained from electrolyte no. 1 at i_k = 10 A/dm^2: (a) LC–the device is not connected; (b) the device is connected.

and an induction–capacitance device [2]. The circuit parameters were selected so that the electrode potential shifted the most towards the more positive range.

Polarization variations were carried out in the galvanostatic mode at the stepped variation of the current with a lag of 30 s at each value [2, 3]. The coatings were deposited on a platinum electrode. The current value was setup by a resistance box according to the indications of a voltammeter of the M209 type. The cathode potential was measured by virtue of a B7–27A/1 voltmeter; the alternating components in the power supply–bath circuit were registered using a C4-56 frequency analyzer.

In a standard mode, coatings were deposited on samples of foil-coated fiberglass plastic with a surface area of 0.02–0.04 dm^2 during 1.5 h at a current density of 2 A/dm^2. At other current densities, the time of the experiments was calculated in proportion to the selected current intensity.

For studying the coating morphology, scanning electron microscopes (TESLA BS-340 and TESCAN) were applied. The local chemical composition was determined by the SEM and INCA Energy EDX systems. The X-ray-structural analysis was carried out using a diffractometer (DRON-5) in cobalt radiation.

RESULTS AND DISCUSSION

At coating deposition from general-service sulfate electrolyte no. 1, the ICD connection exerted an appreciable influence on the morphology of the copper coatings: in the deposits obtained at current densities up to 4 A/dm^2, crystalline aggregates with sharply defined faces were formed instead of the pyramidal growth observed on the surface of the coatings deposited without ICD [2]. The current density increase up to 10 A/dm^2 in both cases caused the coating growth in the form of "spherulites"; however, they were generous in size in the case of the device application. Besides, their morphology appreciably differed (Fig. 1): on the "spherulites" obtained with application only of the power supply, small structural elements of hemispheric form were observed (Fig. 1a); they were of "fibrous" type with certain orientation when the ICD was connected (Fig. 1b).

On the surface of the coatings obtained from more dilute sulfate electrolyte no. 2 without the ICD connection, there took place formation of crystalline aggregates appreciably differing from each other (Fig. 2a). At deposition with application of the power supply connected with the circuit, their sizes increased and they were more homogeneous; this signified ordering of the coating growth process (Fig. 2b). The current density increase (3 A/dm^2) resulted in a reduction of the above mentioned aggregates.

A difference richer in contrast was observed for the coatings obtained from the same electrolyte deposited on a polished substrate of stainless steel under operating conditions with a three-phase power supply with connection of a parallel circuit of the earlier described construction [1, 4]. In the first case, the surface of the copper deposit consisted of hemispheres significantly differing in sizes (Fig. 3a). In the second case, the coating was a number of flat crystalline aggregates of identical sizes; this favored decreasing of the surface roughness and increasing of the plasticity and strength (Fig. 3b) (a qualitative estimation of the plasticity and strength was carried out according to the number of bends of the copper foil separated from the substrate). Thus, the given experimental results count in favor of a significant influence of the ICD on the morphology of the copper deposit surface with the other electrolysis conditions being similar.

An unusual behavior of the coating growth was found at further decreasing of the copper sulfate concentration and increasing of the sulfuric acid content (electrolyte no. 3).

In the absence of the induction–capacitance circuit, copper was deposited in restricted-size islands located at a considerable distance from each other and in the form of dendrites as well (Fig. 4a).

When the ICD was connected, on the surface of the copper coatings deposited at a current density of 1.5 A/dm^2, there were formed aggregates of unusual sphericity with a diameter up to 30 μm spaced up to

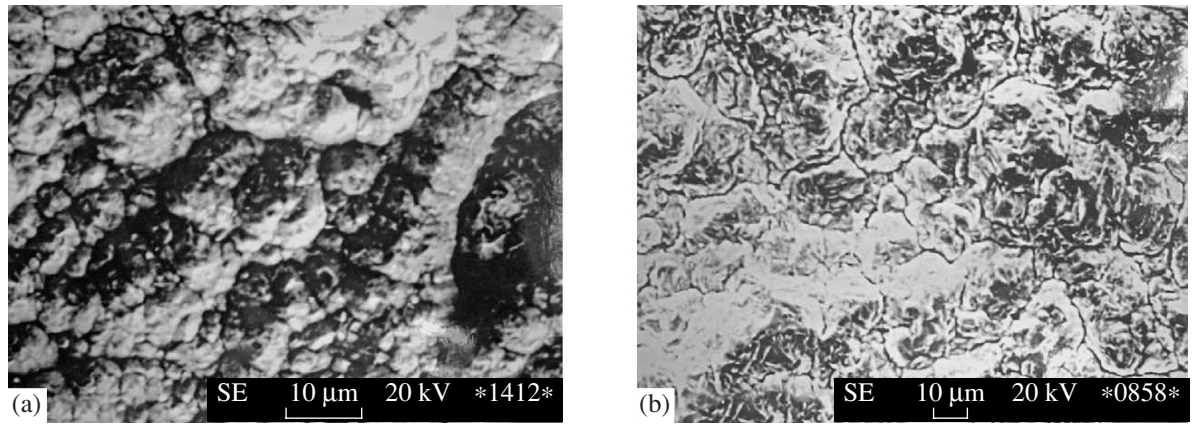

Fig. 2. Morphology of the surface of the coatings obtained from electrolyte no. 2 at $i_k = 2$ A/dm^2: (a) LC–the device is not connected; (b) the device is connected.

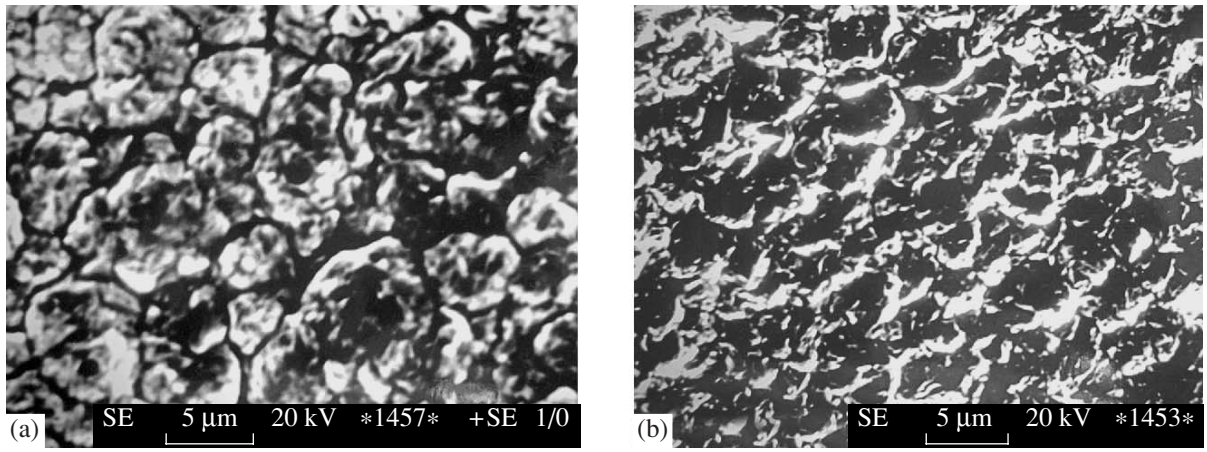

Fig. 3. Morphology of the surface of the coatings on foil obtained from electrolyte no. 2 at $i_k = 2$ A/dm^2: (a) LC–the device is not connected; (b) the device is connected.

15 µm and more apart. As a rule, they did not come in contact with each other; this signifies a limited amount of active crystallization centers and a decrease of the nucleation rate (Fig. 4b). Contacting of surfaces of these aggregates could result in their intergrowth. After formation of the first layer of the coating on their surfaces, active centers appeared favoring formation of a new layer of the "spheres." Crystals with a square cross section were observed in some places of the sample surface (Fig. 4b).

The current density increase ($i_k = 2$ A/dm^2) intensified the processes of growth and destruction of the above mentioned formations, resulting in an increase in the number of crystals of various forms and sizes on the sample surface (Fig. 4c).

"Spheroids" are, apparently, crystalline aggregates consisting of a nucleus and a periphery; at destruction, they are parted into a number of crystals remaining on the sample surface (Fig. 4c). Both "spheres" and crystals could be easily separated from the base with insignificant efforts (by swabbing). It is within the realm of possibility that the separate crystals were a result of continued growth of the formed microcrystals on active centers. In addition, "spheroids" grew on the crystal surfaces too (Fig. 4c). On the polarization curve, a significant shift of the cathode potential towards the more negative range (up to –500 mV at $i_k = 4$ A/dm^2) is observed; moreover, due to the instability of the deposition, the electrode potential varied over a wide range (25–50 mV).

On the crystal surface, there were observed densely spaced growing hemispheric microaggregates (Fig. 4d), which consisted of smaller structural components ~10–15 nm (Fig. 4e). A detailed study of the destroyed section of the crystal has shown that the given surface consists of structural elements of prolate form (Fig. 4f) containing smaller elements; their sizes did not differ from the above-mentioned ones (Figs. 4e and 4g).

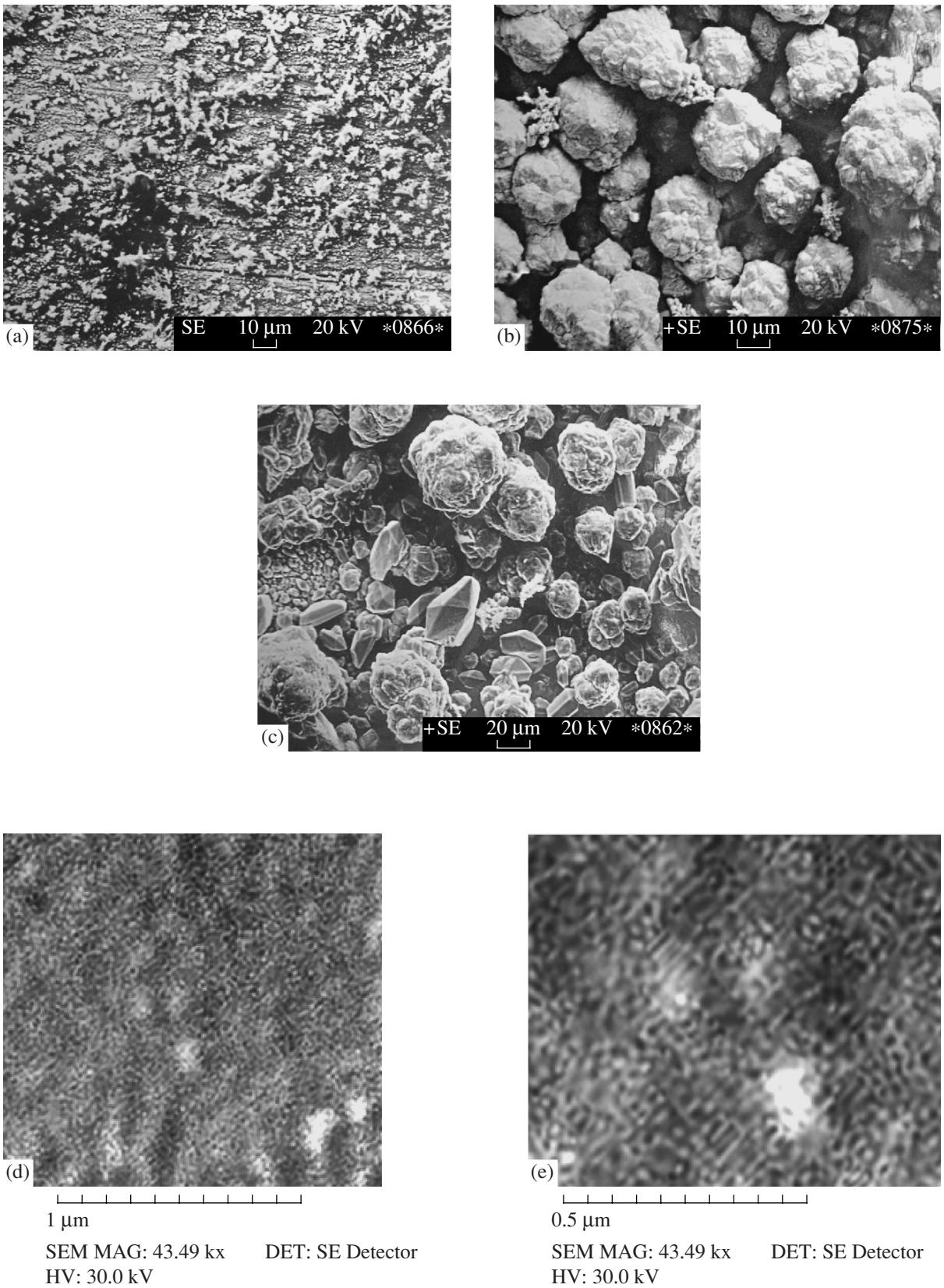

Fig. 4. Morphology of the surface of the coatings obtained from electrolyte no. 3: (a) LC–the device is not connected at $i_k = 2$ A/dm^2; (b) the device is connected at $i_k = 1.5$ A/dm^2; (c) the same at $i_k = 2$ A/dm^2; (d) the same on the crystal surface; (e) the same; (f) the same at the broken crystal surface; (h) the same at the density $i_k = 2.5$ A/dm^2; (i) the same at $i_k = 3$ A/dm^2; (j) the same.

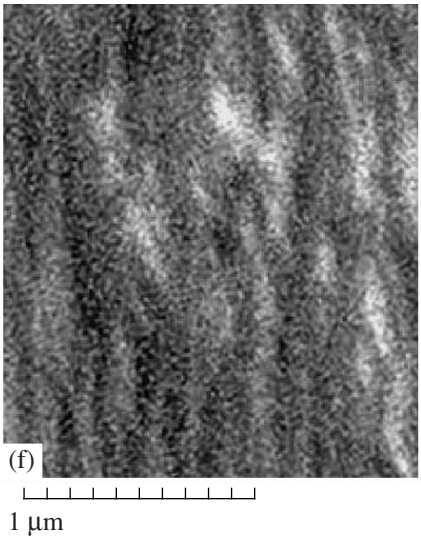
(f)
1 μm
SEM MAG: 25.77 kx
DET: SE Detector
HV: 30.0 kV

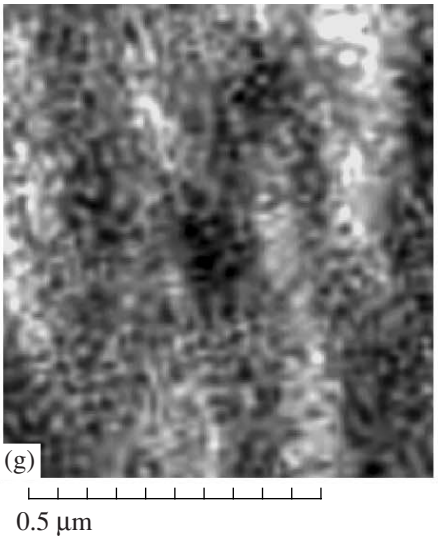
(g)
0.5 μm
SEM MAG: 25.77 kx
DET: SE Detector
HV: 30.0 kV

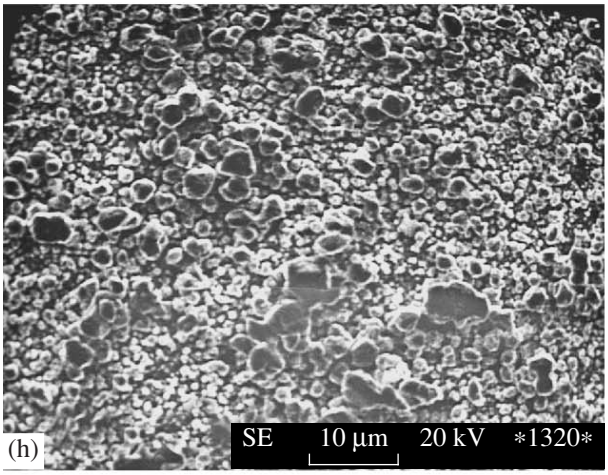
(h)
SE 10 μm 20 kV *1320*

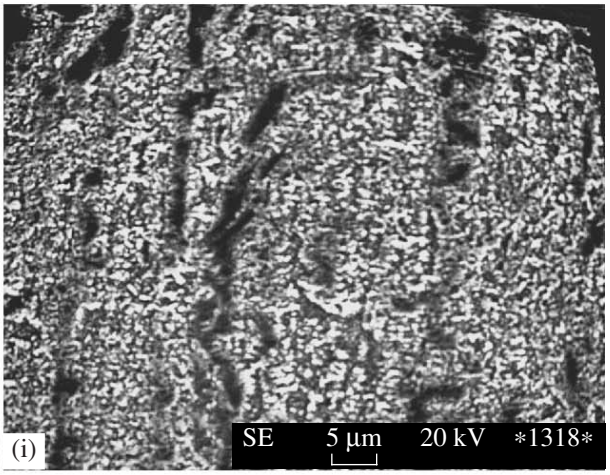
(i)
SE 5 μm 20 kV *1318*

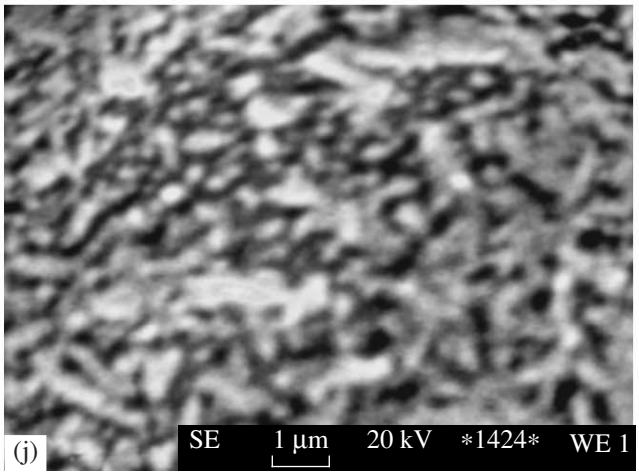
(j)
SE 1 μm 20 kV *1424* WE 1

Fig. 4. (Contd.).

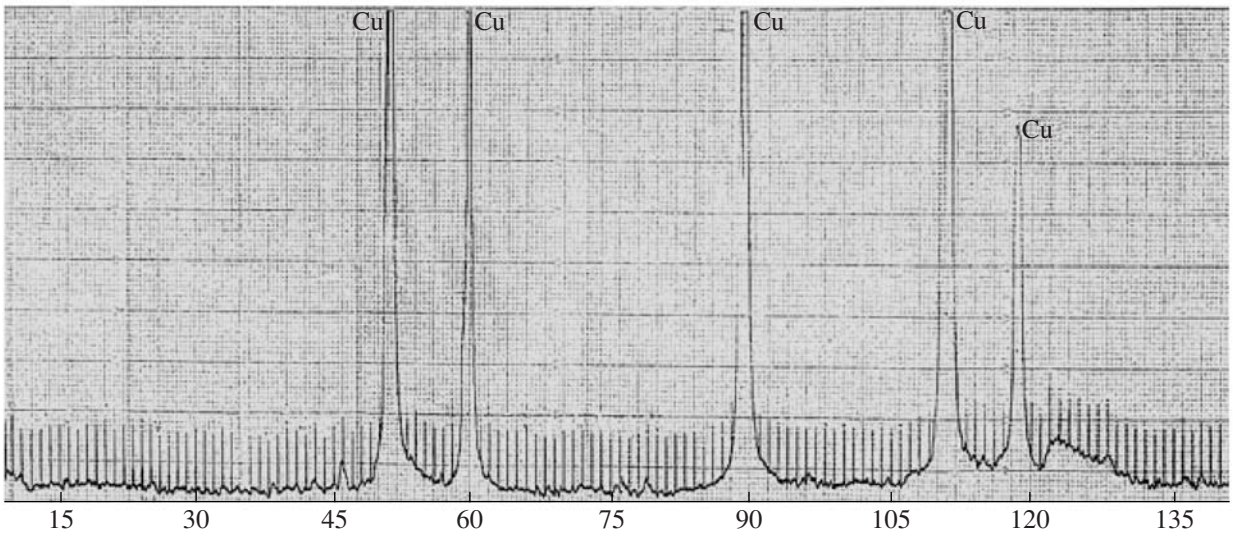

Fig. 5. Diffractogram of the surface of the coatings obtained from electrolyte no. 3 at $i_k = 2$ A/dm^2.

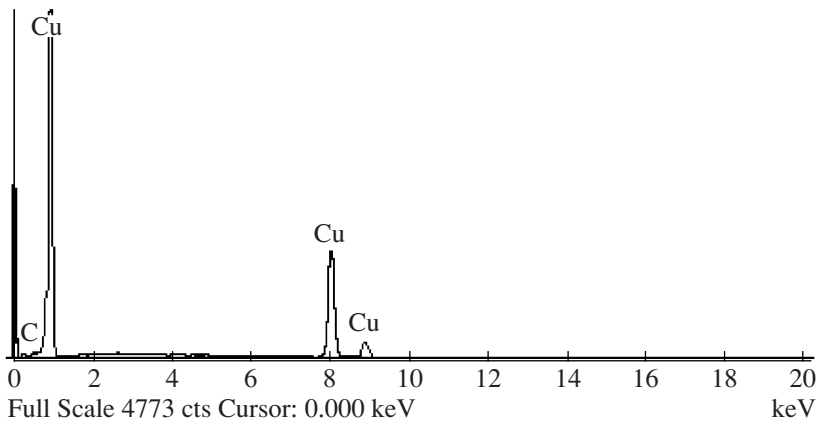

Fig. 6. Local microchemical analysis of the coatings obtained from electrolyte no. 3 at $i_k = 2$ A/dm^2 ($C = 3.47$ wt %).

A more detailed study has shown that the surface is homogeneous and that, on it, there are no separating boundaries between the apparent greater structural components (Fig. 4d); this, probably, is due to the surface roughness and the peculiarities of the photography.

On the studied sample diffractograms, there are only lines of the copper diffraction spectrum (Fig. 5). However, microchemical and X-ray analysis shows the presence of carbon in addition to copper (Fig. 6). It is difficult to explain its inclusion taking into account the selected conditions of the electrolysis. Therefore, additional research is necessary for finding the factors that caused the carbon inclusion.

On the surface of the samples coated at a current density of 2.5 A/dm^2, only crystals of various forms and sizes were found (Fig. 4d). The majority of them had a square cross section. The absence of spheroids confirms the earlier expressed assumption of the possibility of crystal growth from microcrystals on both substrate active centers and newly formed surfaces.

It is apparent that, in this case, due to the overstress intensification, a number of nuclei increased providing growth of a set of various crystals. In some places, great aggregates are observed; they could have been formed as the result of "intergrowth" of neighboring crystals (Fig. 4h).

Further increase of the current density ($i_k = 3$ A/dm^2), probably, resulted in a greater increase of the number of nuclei, which, enlarging, favored copper deposition on great sections of the sample. Other forms of growth were absent. The study of these coatings has shown that they consisted of homogeneous structural components uniformly distributed over the surface (Fig. 4j).

Analysis of the conditions of the formation of a two-dimensional or three-dimensional nucleus has shown that, at the beginning, especially at low overstresses, formation of a nucleus with a noncrystalline structure is

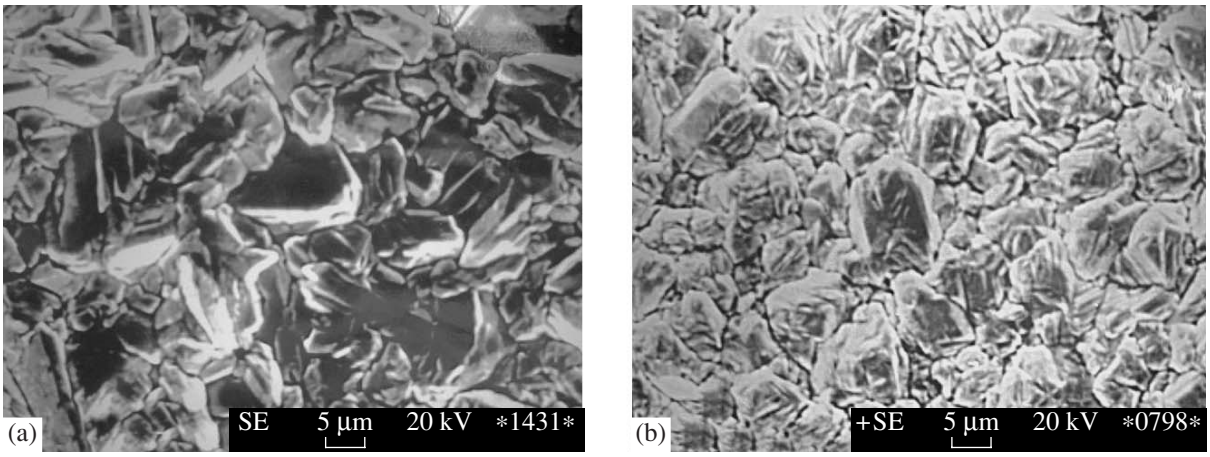

Fig. 7. Morphology of the surface of the coatings obtained from electrolyte no. 4 at $i_k = 2$ A/dm^2: (a) LC–the device is not connected; (b) the device is connected.

energetically preferable [5, 6]. These small particles are more stable than usual crystalline nuclei, and the spherical form is energetically advantageous for them. Due to the nonstationarity of the processes of nucleation and growth, there takes place the cathode potential variation in time; this predetermines the formation of stable nuclei on active centers and their growth due to accumulated adatoms and joining of discharged metal atoms into growing clusters. Variation of the concentration of adatoms affects the overstress value, which, in turn, influences the formation of new nuclei [5].

If clusters of hemispheric form grow at a great distance from each other, then their radius depends on diffusion $(cDzF)^{-1}$ and electrochemical $(\exp(azF\eta)(i_0r)^{-1})$ factors [5, 7]. In this case, the overstress is determined by the cluster size; at their intergrowth, a strong influence on the coating growth may be exerted by the diffusion factors [7] and diffusion layer thickness, causing a further increase of the overstress.

At formation of a great number of small nuclei and at relatively high overstresses, in the beginning, the diffusion factors exert a stronger influence; as a result, there take place overlapping of diffusion bands, smoothing of the potential value, and the current density variation in accordance with the sizes of the newly formed nuclei, leading to matching of their sizes [5, 7].

Henceforth, on amorphous hemispheric islands, microcrystals are formed; their growth results in the formation of crystals of various types [6].

As was mentioned above, under the selected experimental conditions, in the case of coating deposition without ICD, copper was practically not deposited. The same was observed with connection of only the inductance despite the fact that, due to its influence in the power supply–bath circuit, the following took place: principal current pulsation matching, the cathode potential shift towards the more negative range, and suppression of alternating components. After connection of the capacitance, the dynamic conditions of the electrochemical process, apparently, changed. At various current densities, there appeared favorable conditions for new forms of growth of the coatings in the form of spherical crystalline aggregates, large crystals, and thin coating layers.

It is evident that new deposition conditions predetermined the values of the electrochemical and diffusion factors; the mechanism of their influence; and, therefore, the growth morphology.

The above expressed proves that varying of the electrolysis conditions and the ICD parameters allows obtaining of deposits characterized by a structure differing from the known ones. This statement is confirmed by the results of investigation of the morphology of the coatings obtained from hydrofluoboric electrolyte no. 4.

In contrast to the previous experiments, at measurement of polarization curves, the cathode potential varied only in the positive range. Optimal values of L and C caused the electrode potential to shift by 20 mV towards a more positive range at $i_k = 10$ A/dm^2.

On the surface of the coating obtained only from the power supply, at $i_k = 2$ A/dm^2, a tendency for platelike growth was observed; the surface fragments were located chaotically and significantly differed in their configuration (Fig. 7a). This morphology of the coating is probably due to its predominant formation by the mechanism of lateral growth [8].

Connection of the inductance–capacitance device caused a significant change of the coating formation mechanism. On the deposit surface, there were formed crystalline aggregates close in their sizes with obviously pronounced orientation and sharply defined faces (Fig. 7b). Morphological elements of these coatings consisted of separate crystals with a square cross section being generally located perpendicular to the substrate. They resembled the described crystals in many details; however, they were of smaller sizes. The cur-

rent density increase (i_k = 4 A/dm^2) did not change the coating growth behavior; nevertheless, the crystalline aggregates were reduced and some faces were rounded. Formation of these coating is, apparently, related to the electrochemical process ordering, i.e., synchronization of separate stages of deposition due to the ICD influence. This influence of the circuit became possible because the electrochemical process is discrete and it is affected by many factors determining the electrode kinetics and, therefore, structure and physicomechanical properties of the coatings [9, 10].

This research has shown that variation of the L and C parameters of the considered devices and selection of the electrolyte composition, modes, and other conditions of deposition allow obtaining crucially new coatings with original properties; this makes it possible to considerably enlarge the sphere of application of electrodeposited coatings and to develop more efficient technological processes.

REFERENCES

1. Gologan, V.F., Electrochemical Process Control by Induction–Capacitance Devices (Review), *Elektron. Obrab. Mater.*, 2005, no. 6, pp. 39–43.
2. Gologan, V.F., Bobanova, Zh.I., Ivashku, S.Kh., Popov, V.A., and Mazur, V.A., Peculiarities of Galvanic Coating Electrodeposition Process in the Case of Single–Phase Power Supply with Embedded Induction–Capacitance Device, *Elektron. Obrab. Mater.*, 2007, no. 2, pp. 12–16.
3. Vagramyan, A.T. and Zhemagortsyants, M., *Elektroosazhdenie metallov i ingibiruyushchaya adsorbtsiya* (Metal Electrodeposition and Inhibiting Adsorption), Moscow: Nauka, 1969.
4. Gologan, V.F. and Unguryanu, V., USSR Inventor's Certificate no. 1621559, 1990.
5. Vikarchuk, A.A. and Volenko, A.P., Pentagonal Crystals of Copper: Variety of Growth Forms and Peculiarities of Internal Structure, *Fiz. Tverd. Tela* (S.-Peterburg), 2005, vol. 47, issue 2, pp. 339–344 [Physics of the Solid State, vol. 47, issue 2, pp. 352–356].
6. Vikarchuk, A.A., Volenko, A.P., Gamburg, Yu.D., and Snidenko, V.I., Initial Stage of Three–Dimensional Nucleation of Pentagonal Crystals, *Electrokhimiya*, 2005, vol. 41, no. 9, pp. 1120–1124.
7. Gamburg, Yu.D., *Kristallizatsiya metallov i splavov* (Crystallization of Metals and Alloys), Moscow: Yanus–K, 1997.
8. Povetkin, V.V. and Kovenskii, I.M., *Struktura elektroliticheskikh pokrytii* (Structure of Electrolytic Coatings), Moscow: Metallurgiya, 1989.
9. Frumkin, A.N., Andreev, V.N., Boguslavskii, L.I. et al., *Dvoinoi sloi i elektrodnaya kinetika* (Double Layer and Electrode Kinetics), Moscow: Nauka, 1981.
10. Tyagai, V.A., Noises of Electrochemical Systems (Review), *Elektrokhimiya*, 1974, vol. 10, no. 1, pp. 3–24.

ISSN 1068-3755, Surface Engineering and Applied Electrochemistry, 2008, Vol. 44, No. 1, pp. 23–28. © Allerton Press, Inc., 2008.
Original Russian Text © P.S. Orlov, 2008, published in Elektronnaya Obrabotka Materialov, 2008, No. 1, pp. 29–34.

ELECTRICAL PROCESSES
IN ENGINEERING AND CHEMISTRY

Electrochemical Processes on Steel Tube Outer Surfaces of Cathode Protected Underground Gas Pipelines

P. S. Orlov

Yaroslavl' State Agricultural Academy, Tutaevskoe sh. 58, Yaroslavl', 150042 Russia

Received August 24, 2007

Abstract—An electrochemical model of steel corrosion of a cathode protected underground gas supply system and methods of determination of the location and dimensions of corrosive metal damage and the spots of the breaching of hydroinsulation have been suggested.

DOI: 10.3103/S1068375508010055

INTRODUCTION

The visual examination of gas pipeline lengths withdrawn from the ground at the drainage points of cathode protection stations has allowed revealing substantial exfoliation of the film hydroinsulating cover *1* on the lower generating tube *2* in the zone of hydroinsulating tape overlap on the previous loop with some corrugation *1* forming (Fig. 1). The film hydroinsulation within the corrugation ranges to 50–75 mm. The pockets occurring between the hydroinsulation and the tube wall are filled with the ground penetrating through the solidity ruptures of the hydroinsulating cover *1*. In most cases, there are observed numerous local exfoliations of the film cover *3* filled with electrolyte *4* (soil waters) on the tube lateral surfaces (in the event there are no mechanical damages of the hydroinsulating tape and overlap tightness). Under the removed film cover from the ground "pockets" there are most often found local corrosion damages of the tube *5* wall at a depth of 3–6 mm. At the same time, it should be noted that the hydroinsulating cover exfoliation along the upper generating line is absent. The compound (primer) adhesion to the surface in such places is so high that it is easier to separate the primer from the protecting film than from the tube surface.

Such drastic corrosion damage of the gas pipeline near drainage points of the cathode protection stations is at first glance a rather unique phenomena precisely because, after the protecting potential has been superimposed by the cathode protection station (in the case of the breakage of the hydroinsulation), there takes place the polarization of the steel tube surface contacting with the wetted ground or moisture penetrating under the shielding hydroinsulating cover. A high protective potential (1.5–2 V m.s.e. at a distance of one and a half kilometers from the drainage point) gives rise to a high (up to E_P = –1.2 V) polarization potential in heavy wetted soils. The tube surface polarization shifts

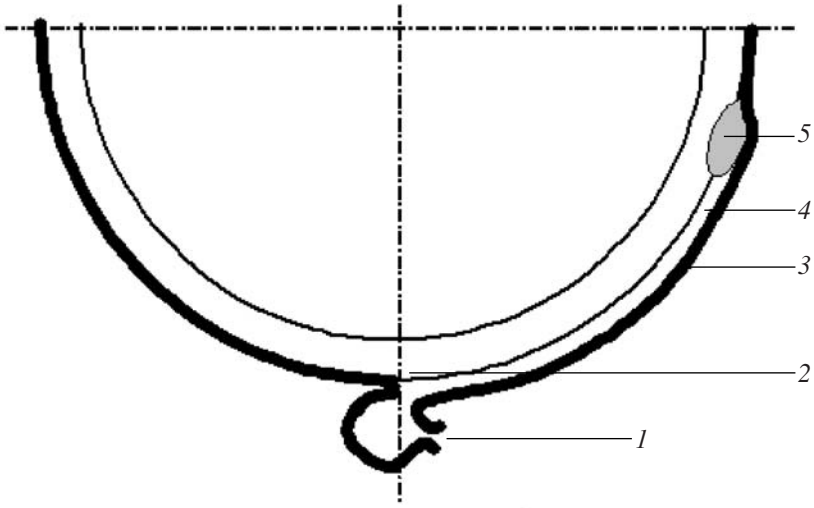

Fig. 1. Corrosion of the underground cathode-protected pipeline at the cathode protection drainage point.

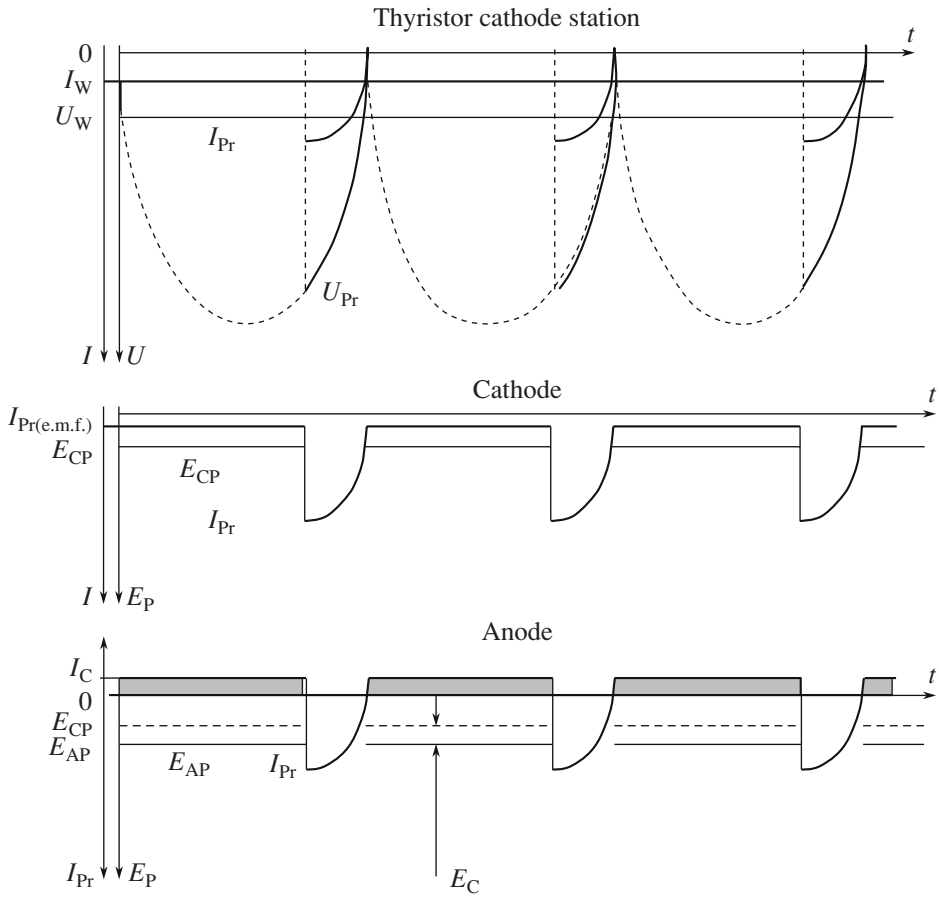

Fig. 2. The scheme of the thyristor cathode station operation.

the equilibrium electrochemical reaction $Fe \longleftarrow Fe^{2+} + e$ to the left, but the absence of iron oxides and hydroxides on the tube surface favors the reaction $H^{1+} + e = H$, resulting in the penetration of hydrogen into the steel and improvement of the iron electrode potential (precisely its reduction) observed at the measurement of the gas main protective potentials, the oscillation amplitude of which along the pipeline length after the protective potential has been superimposed isn't normally more than 0.015 V, and more often it changes even less–thousandths of a volt from the theoretical curve.

THEORETICAL ANALYSIS

The explanation of the probable causes for origination of intensive corrosion processes in tube steel even in the immediate vicinity of cathode protection station drainage points is possible only after elucidation of the operating conditions of such constructions where there are installed thyristor regulators, the work of which is based on the phase pulse principle (Fig. 2). According to this principle, the necessary magnitude of the protecting current and voltage is obtained at the expense of the transformation of the alternating sinusoidal phase pulse current with a frequency of 50 Hz into alternating amplitude unipolar pulses with a recurrence frequency of 100 Hz.

The effective value of the current I_W and voltage U_W in such regulators is determined by the relation between the time of the current passage in the circuit and the time of pauses between separate pulses (I_{Pr}, U_{Pr}). The designed choke can't in full measure fulfill its function to smooth fluctuations as protection currents are rather big at the moments of loads of about half of the maximum permissible ones, and the duration of the pauses between separate impulses is substantial at minimum values of the current and voltage at the exit of the cathode protection station.

In this connection, the fluctuation coefficient remains large. The result is that the pipeline, formally shielded by the effective value of the guard potential, is actually not protected during the pauses between relaying impulses. As in some places (Fig. 1), there exist great local breakages of hydroinsulation *1* and soil and moisture penetrate under the film coating. In the immediate vicinity of the breakage places, the tube surface is efficiently aerated by the air in the soil. So, on the surface of pipeline *2*, there appear some areas of metal where the adsorption of hydrogen and the polarization

is hampered due to the presence of a substantial quantity of air oxygen and nitrogen.

In the immediate vicinity of the regions of great local damages of hydroinsulation, there exist zones of film coating exfoliation *3* filled with soil waters *4* and the access of oxygen into them is highly hampered. As a result, on the tube metal surface (Fig. 2), there appear areas with different potentials E_{AP} and E_{CP} between which, during the pauses between protecting impulses, there is current

$$I_{Pr(emf)} = I_C, \quad (1)$$

and its magnitude depends on the corrosion e.m.f.:

$$E_{(C)} = E_{CP} - E_{AP}, \quad (2)$$

efficiently aerated areas *1* (Fig. 1) being the cathodes of current sources, as for the weakly aerated anode surfaces *5* there take place electrochemical corrosion processes due to the carrying away and loss of iron ions. At the moments of the arrival at the tube of negative shielding impulses (I_{Pr}, U_{Pr}) from the cathode protection station the processes are interrupted, but during pauses between shielding impulses they are excited again.

As the amplitude of the shielding impulse U_{Pr} is an order of magnitude more than the shielding potential U_{AP} of the underground construction, the cathode protection at the delivery of relaying impulses operates under the conditions of overprotection (Fig. 2), causing the decomposition of electrolyte (soil water seeped into the corrugation) with evolution of atomic hydrogen [1], resulting in the further exfoliation of the film hydroinsulation widening the wetted surface of the gas main steel tube.

Cathode polarization "overalkalizes" the electrolyte near-cathode layer. On the surfaces with great local damage of the hydroinsulating coating *1* (Fig. 1), the near-cathode layer pH decreases rather quickly up to the values of pH ≈ 7 because the system is open. At the sites of the minor hydroinsulation exfoliation *4*, where the communication with the environment is hampered, the pH value keeps high (pH = 9–12) for a long time, and there appear areas with different concentration of protons in the electrolyte. As a result, the concentration galvanic cell begins to function; its e.m.f. is defined by the Nernst equation:

$$E_{(C)} = -0.0592[\Delta pH + \log(C_A/C_K)]. \quad (3)$$

The presented mathematical model of the corrosion process determines the e.m.f. of this voltaic cell through the difference of the pH values of the cathode and anode areas and the logarithm of the relations of concentrations C_A of hydrogen, adsorbed by highly dispersed deposits of anode areas at the sites of the local minor exfoliation of the film hydroinsulating cover, to the hydrogen concentration C_{Ka} on the good aerated surfaces of the cathode areas at the sites of a great local damage of the film hydroinsulation. Expendable materials of the differential hydrogenation voltaic cell are hydrogen and tube iron as the potential difference shifts all the oxidation processes rightward [2].

The protective impulses being supplied to the magnetite film, preventing hydrogen from penetration into the tube metal and retarding the corrosion processes, is initially removed [3]:

$$Fe_3O_4 + 2H_2O = Fe(OH)_2 + 2FeO(OH). \quad (4)$$

Magnetite (at the stage of cathodic reduction to iron) is characterized by the lessened electrochemical activity, and the process is complete in about 5 years. Nearly the whole formed iron III metalhydroxide and iron II hydroxide fall from the lower generating tube to the bottom of the corrugation *1* (Fig. 1). The carrying away of the reaction products from the tube lateral surfaces is hampered and they collects *5* under local exfoliations of hydroinsulation *3*, contacting with the tube *2* surface. The pipeline cathodic polarization results in the corrosion product reduction to metal iron according to the scheme

$$FeO(OH) \longrightarrow Fe(OH)_2 \longrightarrow (HFeO_2)^{1-} \longrightarrow Fe; \quad (5)$$

$$FeO(OH) + H_2O + e \longrightarrow Fe(OH)_2 + (OH)^{1-}; \quad (6)$$

$$Fe(OH)_2 + (OH)^{1-} \longrightarrow (HFeO_2)^{1-} + H_2O; \quad (7)$$

$$(HFeO_2)^{1-} + H_2O \longrightarrow Fe + (OH)^{1-}. \quad (8)$$

Iron oxides and oxide hydrate being absent on the tube surface, the electrolyte protons reduce and the metal surface is covered with atomic hydrogen with

$$H^{1+} + e \longrightarrow H, \quad (9)$$

contributing to steel hydrogenation [4].

During pauses between impulses, there occurs steel failure on the anode (strongly hydrogenated) areas alongside with the adsorbed hydrogen oxidation according to the reaction

$$Fe + H_2O = FeO + 2H\uparrow, \quad (10)$$

and at the increased alkalinity in accordance with the reaction

$$Fe + 2H_2O = Fe(OH)_2 + 2H\uparrow. \quad (11)$$

Both processes are attended by evolution of hydrogen, which can penetrate into steel. As different tube surface areas, being under dissimilar conditions, are either an anode or cathode the differential hydrogenation secondary chemical element electromotive force [5] is equal to the potential difference of the tube surface anode areas in relation to cathode ones.

Current-generating process during the pauses between protecting impulses on the iron electrodes of the differential hydrogenation secondary chemical ele-

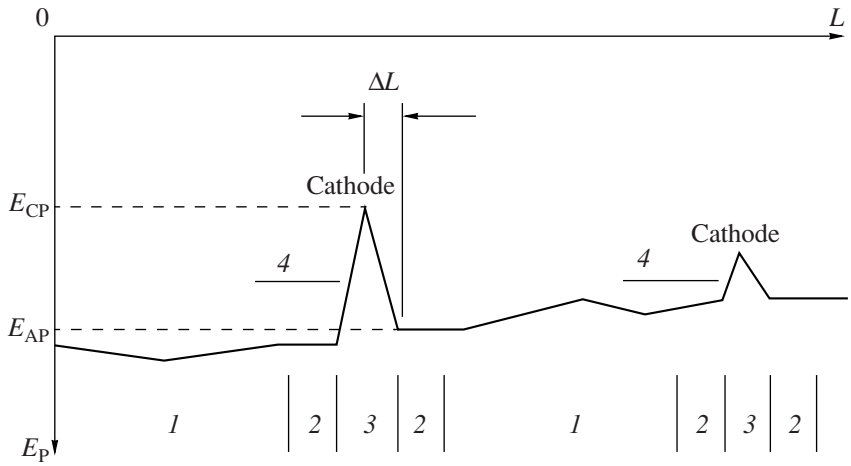

Fig. 3. Polarization potential curve.

ment is defined by one and the same reaction (9), proceeding in different directions

$$0.5H_2 = H^{1+} + e, \quad E_{P-} = -0.00\ \text{V} \quad \text{(anode)},$$

$$H^{1+} + e = 0.5H_2, \quad E_{P+} = 0.00\ \text{V} \quad \text{(cathode)}.$$

E.m.f. $E_{(COR)}$ between the surface cathode and anode areas of the underground gas main, covered with film hydroinsulation, during the pauses between the cathode station protective current pulses depends on three components:

$$E_{(COR)} = \Delta\varphi(COR) + \Delta\varphi(COR) + \Delta\varphi(pH). \quad (12)$$

Concentration component doesn't exceed $\Delta\varphi(COR) \leq 0.25$ V. The value of the medium pH along the pipeline length changes moderately—in the most cases pH value of the anode and cathode surfaces is the same: $\Delta\varphi(pH) = 0.00$ V. The potential difference of two identical iron electrodes $\Delta\varphi(COR)$ is zero. So e.m.f. depends only on $\Delta\varphi(COR)$. Ion exchange being hampered at different values of pH for each of the electrodes (cathode and anode sections of the tube surface), the magnitude of potential difference between two "plates," determined by pH quantities of the areas, will be: $\Delta\varphi(pH) \leq 0.237$ V at $\Delta pH \leq 4$. Then the maximum possible value of potential difference of cathode and anode areas is $E_{(COR)} = 0.487$ V.

Negative protecting impulse being supplied to the tube the electrochemical element in the medium with high alkalinity operates under the conditions similar to ones of the iron accumulator charge. Besides reaction (6)–(8) there can proceed the reaction of iron oxide reduction:

$$2e + FeO + 2H_2O = 2(OH)^{1-} + Fe. \quad (13)$$

Oxidation of iron and hydrogen during the pauses between protective current impulses happens only on the anode of the improvised concentration "hydrogenous" secondary chemical source of electric energy, i.e. on the highly hydrogenated (ennobled) tube surfaces at the sites of the hydroinsulation exfoliation, where water (electrolyte) penetrates and aeration is hampered. Other reactions occur on the whole surface of the cathode-protected tube, where the electrolyte (soil waters and moisture) can find its way.

EXPERIMENT PROCEDURE

Existing standard measuring technique has been used to carry out field actual testing. Polarization potential of the underground cathode-protected gas main has been measured with the interval, defined by the necessary accuracy of the polarization curve plotting along the underground pipeline with the aid of the copper-sulfate reference electrode, the cathode protection station being disconnected, within 5–10 s after its disconnection.

RESULTS

The examination of the results of tube potential actual measurements conducted with the system of gas mains has permitted to reveal "dip funnels" *4* in the polarization potential curves of amplitude 0.2–0.4 V (Fig. 3) even in the immediate vicinity of the cathode protection stations over distances not more than 100–150 m from the drainage points where the pipeline is with certainty protected by the cathode protection station. As practice shows such "dip funnels" of polarization potentials suggest the existence of mechanical damage of the hydroinsulating cover solidity in the places where the measurements display the presence of their peak values in the curves of polarization potentials and gas main wall corrosion breakages along the edges of polarization potential "dip funnels."

DISCUSSION

As hand in hand with oxidation of iron is its intensive reduction there are virtually absent corrosion prod-

ucts at the sites of the direct corrosion rupture during the periods of protective impulse arrival at the tube. The film hydroinsulating coating being withdrawn from the sites of the corrosion damage it could be found easily removable layer of black color—mechanical mixture of a dispersed iron with the impurity of iron oxide FeO and tribasic metahydroxide of iron FeO(OH) together with a minor amount of $Fe(OH)_2$.

Multi-kilometer steel tube though having a substantial surface area possesses very small specific surface, as a result the amount of hydrogen adsorbed by the tube is limited. At the same time when in time there appear a lot of fine-dispersed deposits on the tube surface they take an active part in the corrosion fracture process as they can absorb much hydrogen resulting in the drop of the electrode potential of the steel surface the deposits contacting with; moreover the deposits begin to play the role of the active mass of the iron alkaline accumulator negative electrode. The deposits have thinly dispersed structure due to the sizable specific surface and are more active and reactive than the metal surface somewhat reducing the rate of iron ion carrying away from the tube wall.

The work of the secondary chemical source of the differential hydrogenation current is controlled by the relation of anode and cathode areas. If cathode area is substantially less than anode one, the rate of corrosion is small due to the quick polarization of the positive electrode (the tube cathode section). It is observed more often on the long over-wetted sections of the main. If the area of anode regions is substantially less then the area of cathode one there are observed local corrosion defects of the lateral surfaces of gas main tubes in wet heavy soils.

The secondary chemical current source, namely the steel tube surface, has minimum capacity immediately after banking with ground as necessary conditions haven't formed on its surface yet, appearing as film hydroinsulation exfoliates and soil water (electrolyte) penetrates under insulating cover. Season vertical movements of the gas pipeline in the water-saturated grounds cause the creep of the hydroinsulating coating and penetration of the electrolyte (ground waters) and later ground into space between film and tube, and then there arise conditions for aeration of the surface plots along the lower generating line of the tube between 3–4 and 8–9 h. These conditions develop about 6–12 yr, and then (and simultaneously with these processes) there takes place the formation of the secondary chemical element of the differential hydrogenation with the charge-self-discharge performance using current thyristor sources as cathode protection power supply.

The investigation results show the location and dimensions of corrosion damage of underground gas pipeline metal and its is possible to determine the spots of film hydroinsulation breakage in accordance with the change of the measured magnitude of polarization potentials within 5–10 s after removing the polarization.

Underground construction hydroinsulating cover defects are identified according to the peaks of "dip funnels" *4* of the polarization potential (cathode area *3*), the defect size can be judged from the width of "dip funnels." Anode areas *2* of the metal corrosion damage, proportional to the potential gradient along the pipeline length (Fig. 3), are identified along the margins of "dip funnels" in the polarization curve. The extreme potential difference of two sections of the underground steel construction, indicative of the favorable conditions for intensive corrosion processes on anode surfaces having lower electrode potential, is determined from the polarization curve. The cathode protection is proved by the results of the tube surface overall potential measurements (the whole pipeline total potential is much lower then the polarization potential of the tube metal) to retard efficiently the metal corrosion. To estimate the tube wall corrosion damage depth $\delta_{(COR)}$ mm of the operating gas pipeline which service time proceeds 5 years it is proposed an empirical expression:

$$\delta_{COR} = 2(T_{PL} - 5)\frac{E_{(COR)}}{\Delta L}\frac{I_{max}}{I_{W(AV)}}, \quad (14)$$

where $\frac{E_{(COR)}}{\Delta L}$ is the potential gradient between the top and the base of the "tip funnel" *4* on the section *3* of the polarization potential curve, V/m; T_{PL} is the service time of the gas pipeline, years; I_{max} is the maximum passport current of the cathode protection station, A; $I_{W(AV)}$ is the average working current of the cathode station during the service time, A.

Tube surface corrosion defects are the more the more is uncovered the surface of the underground steel construction as the magnitude of corrosion current (influencing the corrosion damage depth) is determined by the area of the naked (cathode) zone. The length of the pipeline naked sections is the same as the length of cathode zones and is determined according to the polarization potential curve; on the section 1 the corrosion defects are insignificant as the potential gradient is small (Fig. 3).

CONCLUSIONS

1. The influence of the film hydroinsulating cover on creation of conditions for corrosion fracture of the metal of underground pipelines with thyristor cathode protection is shown.

2. The positive effect of the magnetite film on the metal surface inhibiting the corrosion processes and steel hydrogenation is noted.

3. The technique to identify the location of the film hydroinsulating cover defects and corrosion damages of the cathode protected underground pipeline metal is proposed.

REFERENCES

1. Orlov, P.S., Solid State Diagnostics of Locations of the Possible Stress-Corrosion Damages of the Underground Gas Mains with Film Hydroisolation, *Trudy Mezhdunarodnogo foruma po problemam nauki, tekhniki I obrazovaniya (Proc. Int. Forum on the Problems of Science, Engineering and Education)*, Moscow: Izd. Akad. Nauk o Zemle, 2003, pp. 43–45.

2. Orlov, P.S., Influence of Electromagnetic Fields on the Hydrogen Atom Transport in Steel, *Elektron. Obrab. Mater.,* 2007, no. 1, pp. 52–56.

3. Varypaev, V.N., Dasoyan, M.A. and Nikol'skii, V.A., *Khimicheskie istochniki toka* (Current Chemical Sources), Moscow: Vysshaya shkola, 1990, pp. 123–178.

4. Petrov. L.N., Kalinkov, A.Yu., Magdenko, A.N. and Osadchuk, I.P, Element of Differential Hydrogenation, *Zashch. Metal.*, 1990, no 2, pp. 296–299.

5. Orlov, P.S. Reasons for Corrosion Fracture of Cathode Protected Underground Gas PipeLines with Film Hydroisolation, *Trudy Mezhdunarodnogo foruma po problemam nauki, tekhniki I obrazovaniya (Proc. Int. Forum on the Problems of Science, Engineering and Education)*, Moscow: Izd. Akad. Nauk o Zemle, 2006, pp. 99–101.

ISSN 1068-3755, Surface Engineering and Applied Electrochemistry, 2008, Vol. 44, No. 1, pp. 29–32. © Allerton Press, Inc., 2008.
Original Russian Text © G.A. Barbashova, 2008, published in Elektronnaya Obrabotka Materialov, 2008, No. 1, pp. 35–39.

ELECTRICAL PROCESSES
IN ENGINEERING AND CHEMISTRY

Study of Hydrodynamic Processes under Electrical Discharge in a Small Volume of Liquid

G. A. Barbashova

Institute of Impulse Processes and Technologies of the National Academy of Sciences of Ukraine, pr. Oktyabr'skii 43-a, Nikolaev, 54018 Ukraine

e-mail: iipt@iipt.com.ua

Received July 17, 2007

Abstract—The hydrodynamic processes in cylindrical discharge chamber with a small diameter (up to 20 mm) under electrical explosion of a thin wire fixed along its axis are studied using the method of numerical experiment. The dependence of the hydrodynamic loading of the chamber surface upon the kind of boundary conditions of the cylinder butt is particularly considered.

DOI: 10.3103/S1068375508010067

INTRODUCTION

To expand the tubes of heat exchanger grids and in a number of other discharge-pulse technologies, there are used electroexplosive cartridges [1]. The cartridge chamber is most often of cylinder shape. A fine wire is mounted along the symmetry axis of the cylinder, and its cavity is filled with a liquid. Special seals are used to pressurize the liquid, or it is covered with a viscous substance film. Pressure waves generated at the fine wire explosion effect the tube wall and deform it.

The hydrodynamic features of the fine wire electric explosion in a straight ring cylinder of limited length and small (up to 20 mm) diameter filled with water are studied in this work.

STATEMENT OF THE PROBLEM

In the work being carried out, it is suggested that the cylinder (discharge chamber) lateral surface is absolutely stiff and both bases are absolutely stiff (variant 1), the top one is absolutely stiff and the bottom one is a nondeformed disc moving along the tube until an absolutely stiff obstacle is reached that is used to pressurize the liquid (variant 2), or the top of the cylinder is covered with a viscous substance film and a movable rigid disc is the lower base (variant 3). There is a fine wire along the cylinder symmetry axis (Fig. 1). The discharge chamber is filled with an ideal compressible fluid, and the cavity (discharge channel) appearing after the fine wire explosion is filled with an ideal low-temperature plasma.

According to the assumptions, the mathematical problem is formulated as follows. In the region of the fluid limited by the water–plasma contact boundary (the discharge channel wall) and the cylinder with absolutely stiff bases, an absolutely stiff top base and a movable nondeforming lower one, or the free surface at the top base (when the liquid is limited by a film) and a movable disc at the bottom, it is necessary to solve the set of gas dynamics two-dimensional nonlinear equations written in the cylindrical coordinate system [2]

$$\begin{cases} \dfrac{\partial(r\rho)}{\partial t} + \dfrac{\partial(r\tau\upsilon_z)}{\partial z} + \dfrac{\partial(r\rho\upsilon_r)}{\partial r} = 0 \\ \dfrac{\partial(r\rho\upsilon_r)}{\partial t} + \dfrac{\partial(r\rho\upsilon_z\upsilon_r)}{\partial z} + \dfrac{\partial[r(\rho\upsilon_r^2 + p)]}{\partial r} = p \\ \dfrac{\partial(r\rho\upsilon_z)}{\partial t} + \dfrac{\partial[r(\rho\upsilon_z^2 + p)]}{\partial z} + \dfrac{\partial(r\rho\upsilon_z\upsilon_r)}{\partial r} = 0 \\ \dfrac{\partial(re)}{\partial t} + \dfrac{\partial[r(e+p)\upsilon_z]}{\partial z} + \dfrac{\partial[r(e+p)\upsilon_r]}{\partial r} = 0, \end{cases} \quad (1)$$

and closed by the binomial equation of state [2]

$$\varepsilon = [p - c_0^2(\rho - \rho_0)]/[\rho(\kappa - 1)]; \quad (2)$$

where t is the time; r, z are the cylindrical coordinates; υ_r, υ_z are the radial and axial components of the liquid rate vector; p is the pressure; ρ is the density; $e = \rho[\varepsilon + (\upsilon_r^2 + \upsilon_z^2)/2]$; ε is the specific intrinsic energy; ρ_0, c_0 are the sound density and rate in the resting fluid; and $\kappa = 7.15$.

At the internal boundary of the calculated region (the plasma–water contact break), there is prescribed the pressure, which is determined from the energy balance equation [3]

$$\frac{1}{(\gamma - 1)}\frac{d(p_a V_a)}{dt} + p_a\frac{dV_a}{dt} = N(t), \quad (3)$$

where p_a, V_a are the pressure in the discharge channel and its volume; $\gamma = 1.26$; and $N(t)$ is the law of the

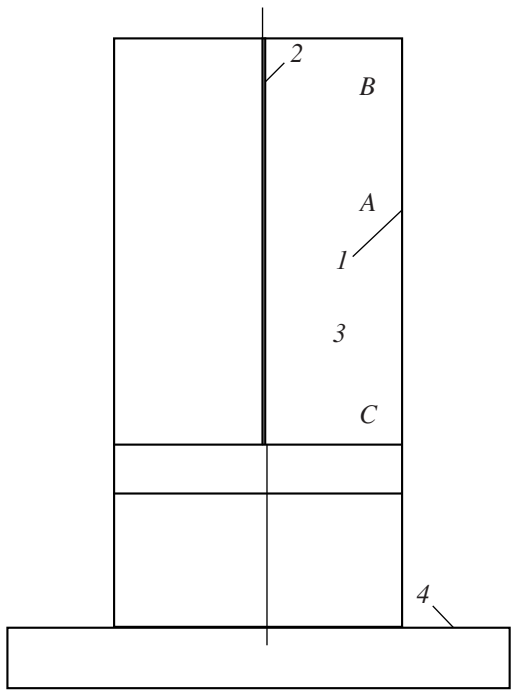

Fig. 1. Electric discharge cartridge diagram: *1*—cylinder surface; *2*—conductor; *3*—stiff disc; *4*—obstacle; *A*, *B*, *C*—points on the cylinder lateral surface.

power admission into the discharge channel, which is given in the following way [3]:

$$N(t) = \begin{cases} 4tE/\tau^2, & 0 \le t \le \tau/2 \\ 4(1 - t/\tau)E/\tau, & \tau/2 \le t \le \tau \\ 0, & \tau < t. \end{cases}$$

Here, E is the amount of energy admitted into the discharge channel, and τ is the duration of the first half-period of the discharge (it is suggested that the total energy is admitted during this time).

On the fixed rigid wall, there is stated the nonleakage condition:

$$\upsilon_n = 0, \tag{4}$$

where υ_n is the normal component of the fluid rate vector.

On the movable rigid disc, the fluid rate is equal to the velocity of the disc movement. The disc travels according to the displacement law for an absolutely hard body:

$$m\ddot{x} = F = 2\pi\int_0^R r(p - p_B)dr. \tag{5}$$

Here, x is the disc displacement, m is its mass, F is the pressure force effecting the disc, R is the cylindrical discharge chamber radius, and p_B is the pressure of the air on the disc. The problem being solved (equation (5)) was rewritten in the form

$$\begin{aligned} m\ddot{x} &\approx 2\pi\sum_{i=1}^{n}\left[(p_i - p_B)\frac{r_{i+1}^2 - r_i^2}{2}\right] \\ &= \pi\sum_{i=1}^{n}[(p_i - p_B)(r_{i+1}^2 - r_i^2)], \end{aligned} \tag{6}$$

where n is the number of partition regions along the disc radius, and p_i is the fluid pressure in the region $[r_i; r_{i+1}]$.

At the free surface,

$$p = 0. \tag{7}$$

At the initial moment of time, the fluid parameters are equal to their values in the undisturbed medium at atmospheric pressure. The discharge channel initial radius is 1 mm, the initial rate is zero, and the discharge channel pressure exceeds the environmental pressure by 1 MPa.

Set of equations (1)–(2) with prearranged boundary and initial conditions is solved by the Godunov relaxation method [2], and differential equation (6) is solved with the help of the explicit scheme of finite differences of the second order of accuracy.

The magnitude of energy E introduced into the discharge channel and the duration of the discharge first half-period were determined by formulas presented in [4] at the following values of the electric circuit parameters: the charge voltage U_0 = 30 kV, the capacitance C = 3 μF, the inductance L = 3 μH, the conductor length l = 45 mm, the cylinder radius R = 10 mm, and the disc mass m = 5 g. The following is obtained: E = 525 J, τ = 10 μs. The power introduction law determined according to these data is depicted in Fig. 2.

THE NUMERICAL EXPERIMENT OUTCOME

Analyzing the results of the problem solution (some of them are presented in Figs. 2–5, where the curve number corresponds to the variant number), the following should be pointed.

In the cylinder with fixed bases, the fluid flow is one-dimensional. After the wave reflected from the lateral surface of the discharge chamber has come to the discharge channel, the pressure versus time (in the fluid and plasma) characteristic has a sinusoid form with an attenuated amplitude and a practically constant period equal to the time of the wave run from the channel to the wall. The pressure magnitude varies about the quantity $p \approx 180$ MPa. The fluid flow tends to be steady.

A different situation arises in the cylindrical discharge chamber with a movable lower base (variants 2 and 3). In this case, the uniformity of the fluid and plasma characteristic distribution along the cylinder symmetry axis is disturbed. The growth of the volume

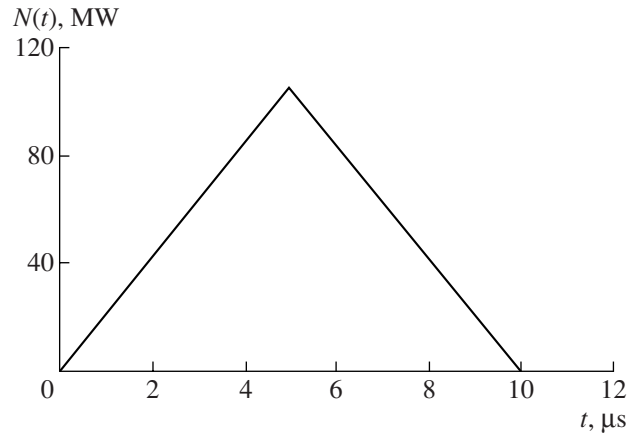

Fig. 2. The law of introducing electric power into the discharge channel.

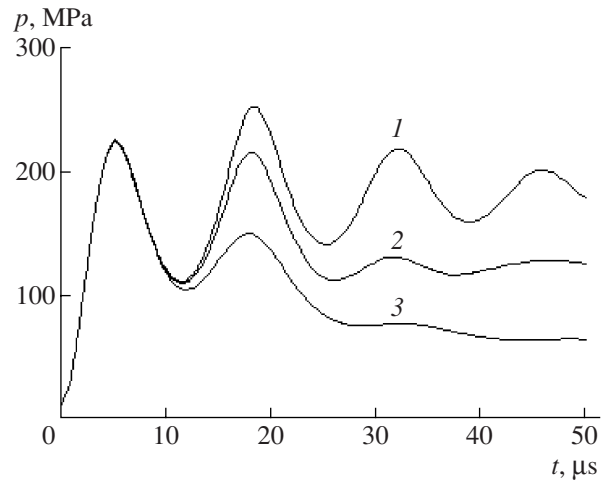

Fig. 3. Pressure in the discharge channel: *1*—the cylinder bases are absolutely stiff; *2*—the top base is absolutely stiff, the lower one is a rigid movable disc; *3*—the top base is a free surface, the lower one is a movable rigid disc.

occupied by the fluid and its issuing out lead to a decrease (compared with variant 1) of the pressure both in the discharge channel (Fig. 3) and in the fluid (Fig. 4). The pressure in the channel drops by nearly one and a half if the top base is a fixed rigid surface and by more than two times when the upper boundary is a free surface (Fig. 3). Approximately the same is the difference between the values of the pressure in the fluid, including the one acting on the cylinder lateral surface (Fig. 4). The oscillation period duration in the pressure curve grows too, and the time of the wave run from the discharge channel to the wall and backward also increases.

Let's compare the results obtained in the calculation of the second and third variants; that is, we'll estimate the influence of the free surface on the flow nature in the discharge chamber (curves *2* and *3* in Figs. 3 and 4). The first pressure peaks in the discharge channel at points *A* and *B* on the chamber wall (Fig. 1) coincide, but the fluid pressure in the vicinity of the free surface is substantially less than the pressure at the absolutely stiff boundary from the very start of the process, which is related to the fluid efflux from the device. With time, the upper boundary influence extends over the whole cylinder volume. For instance, the jump of the fluid pressure on the wall at point *A* connected with the disc reaching the fixed stiff surface in the case when the cylinder top base is absolutely stiff is about 380 MPa, which is 1.6 times more than the value of this very characteristic in the other case (Fig. 4, curves *2* and *3*).

The hydrodynamic load on the disc behaves in a corresponding way (Fig. 5). The first peaks in the curves of the time dependence of the fluid pressure force on the disc for the second and third variants coincide, but, later on, there manifests a fluid efflux through the cylinder top base occurring in the third variant. For instance, the pressure force second maximum in the second variant is more than the second maximum in the third variant

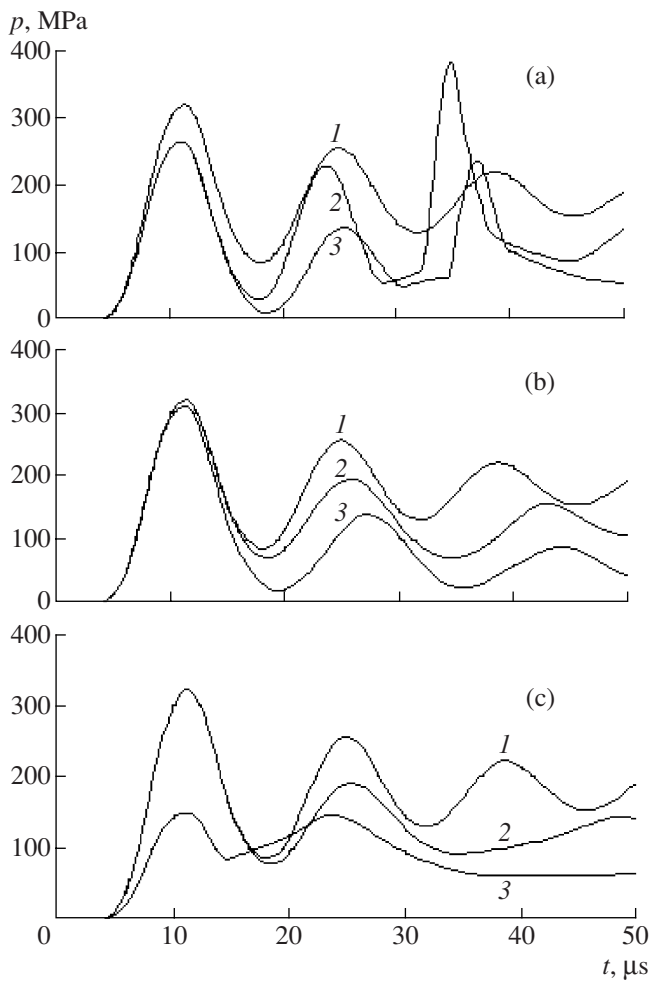

Fig. 4. The fluid pressure on the tube wall at points *A* ([a]), *B* ([b]), and *C* ([c]): *1*—the cylinder bases are absolutely stiff; *2*—the top base is absolutely stiff, the lower one is a rigid movable disc; *3*—the top base is a free surface, the lower one is a movable rigid disc.

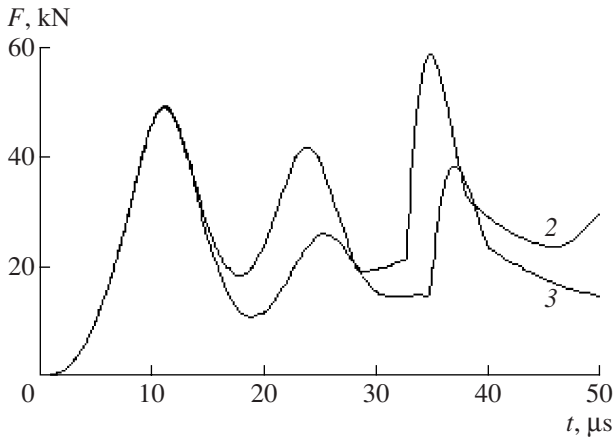

Fig. 5. The force of the pressure on the movable disc: *2*—the top base is absolutely stiff, the lower one is a rigid movable disc; *3*—the top base is a free surface, the lower one is a movable rigid disc.

by a factor of 1.6, and the pressure force jump after the disc impact against the obstacle is half as much. It should also be noted that the influence of the upper boundary kind on the disc motion velocity is not large in the examined case because of the close position of the obstacle. When a stiff surface is the top boundary, the velocity amplitude is ≈205 m/s, and the surface is free, it is ≈175 m/s, i.e., less than the first one by 8%. The rate of the fluid efflux through the cylinder top base is somewhat below 200 m/s.

CONCLUSION

Accordingly, the replacement of the absolutely stiff surface at the electrodischarge cartridge cylinder chamber butt with a movable boundary or free surface causes a rather substantial (by a factor of 1.5–2.5) drop of pressure in the chamber, including one on the lateral surface of the cylinder. Hence, the efficiency of the electric discharge effect on the processed tube surface diminishes.

REFERENCES

1. *Oborudovanie i tekhnologicheskie protsessy s ispol'zovaniem electrogidravlicheskogo effekta* (Equipment and Technological Processes Using Electrohydraulic Effect), Guloi, G.A., Ed., Moscow, 1977.
2. *Chislennoe reshenie mnogomernykh zadach gazovoi dinamiki* (Numerical Solution of Multi-Dimensional Problems of Gas Dynamics), Godunov, S.K., Ed., Moscow, 1976.
3. Naugol'nykh, R.A. and Roi, N.A., *Elektricheskie razryady v vode* (Electric Discharges in Water), Moscow, 1971.
4. Ivanov, V.V., Shvets, I.S., and Ivanov, A.V., *Podvodnye iskrovye razryady* (In-Water Spark Discharges), Kiev, 1982.

ISSN 1068-3755, Surface Engineering and Applied Electrochemistry, 2008, Vol. 44, No. 1, pp. 33–35. © Allerton Press, Inc., 2008.
Original Russian Text © P.N. Pasha, F.P. Grosu, M.K. Bologa, 2008, published in Elektronnaya Obrabotka Materialov, 2008, No. 1, pp. 40–43.

ELECTRICAL PROCESSES IN ENGINEERING AND CHEMISTRY

Charged Particle Motion under the Influence of Crossed Alternative Electric and Magnetic Fields

P. N. Pasha[a], F. P. Grosu[a], and M. K. Bologa[b]

[a] *State Agrarian University of Moldova, ul. Mircheshti 44, Chisinau, MD-2049 Republic of Moldova*

[b] *Institute of Applied Physics of the Academy of Sciences of Moldova, ul. Academiei 5, Chisinau, MD-2028 Republic of Moldova*

Received November 5, 2007

Abstract—Deduction of the formulas for the velocity of charged particles in external crossed electric and magnetic fields synchronously varying according to a cosine law is given. The physical peculiarities of the motions under consideration, as well as their practical applications, are discussed.

DOI: 10.3103/S1068375508010079

INTRODUCTION

Interest in the applications of crossed electric and magnetic fields is caused by the necessity to solve a series of technical problems such as isotope separation, mass electroscopy [1], magnetohydrodynamic separation [2], water cleaning and desalination [3, 4], etc. Use of stationary fields for these purposes is limited by the electrolysis effects, and implementation of alternating synchronous electric and magnetic fields is one of the challenging ways of elimination of undesirable phenomena. In this case, there arises an important problem concerning the particle motion under the influence of the crossed fields. Though there exist some solutions of similar problems, they are absent in the known literature [5–8].

PROBLEM DEFINITION AND SOLUTION

Let the vectors of the electric field intensity $\vec{E}$ and magnetic induction $\vec{B}$ be set by the following equalities:

$$\vec{E} = \vec{k}E_0\cos\omega t, \quad \vec{B} = \vec{i}B_0\cos\omega t, \tag{1}$$

where E_0 and B_0 are the amplitudes of the fields; ω is their frequency; and $\vec{i}$ and $\vec{k}$ are single orts of the coordinate axes x and z, respectively.

We consider the particle with charge q and mass m at the initial moment $t = 0$ to rest at the coordinate origin; i.e.,

$$\vec{r}\big|_{t=0} = 0; \quad \vec{V}\big|_{t=0} = 0. \tag{2}$$

The particle motion equations in terms of (1) take on the form

$$V_x' = 0,$$
$$V_y' = \frac{qB_0}{m}V_z\cos\omega t, \tag{3}$$
$$V_z' - \left(\frac{qE_0}{m} - \frac{qB_0}{m}V_y\right)\cos\omega t.$$

From the first equation of set (3), in view of (2), it follows that $V_x = \text{const} = 0$ is the particle motion occurring in the plane *yoz*.

To solve the remaining two equations, we assume

$$\xi = \sin\omega t. \tag{4}$$

By doing so, we exclude from (3) $\cos\omega t$:

$$V_y' = \frac{\omega_0}{\omega}V_z,$$
$$V_z' = \frac{qE_0}{\omega m} - \frac{\omega_0}{\omega}V_y, \tag{5}$$
$$\omega_0 \equiv qB_0/m,$$

where the prime means the new variable ξ derivative. Excluding V_z from the first equation of set (5), we obtain

$$V_y'' + \frac{\omega_0^2}{\omega^2}V_y = \frac{qE_0\omega_0}{\omega^2 m}. \tag{6}$$

Having defined V_y and V_z from (5), in view of initial conditions (2), we conclusively find the following:

$$V_y = \frac{2E_0}{B_0}\sin^2\left(\frac{\omega_0}{2\omega}\sin\omega t\right),$$
$$V_z = \frac{E_0}{B_0}\sin\left(\frac{\omega_0}{\omega}\sin\omega t\right). \tag{7}$$

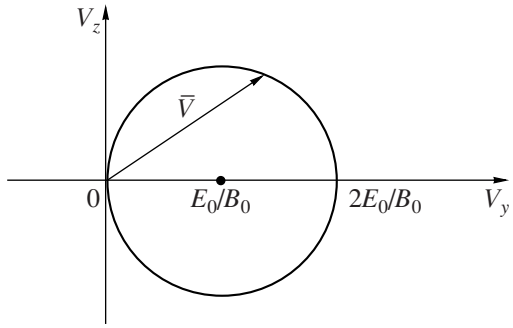

Fig. 1. The velocity hodograph curve.

In the limit of $\omega \longrightarrow 0$, we obtain the case of stationary fields [5]:

$$V_y = \frac{2E_0}{B_0}\sin^2\left(\frac{\omega_0 t}{2}\right),$$
$$V_y = \frac{E_0}{B_0}\sin\omega t. \tag{8}$$

From (7) and (8), it is seen that, as in the case of stationary fields and for alternating synchronous ones too, there is an average (nonzero) component of the particle drift towards OY normal to the field direction defined by the sign of the relations $\frac{E_0}{B_0}$ and not depending on the charge sign, whereas, in the direction of the z axis, the average velocity $V_z = 0$.

In order to gain a better impression of the character of the motion, we'll find the velocity hodograph curve from (7) by rewriting V_y in the form

$$V_y = \frac{E_0}{B_0}[1 - (\cos\delta\sin\varphi)], \tag{9}$$

where $\delta = \omega_0/\omega$; $\varphi = \omega t$.

Then, from (8) and (9), it follows that

$$\left(V_y - \frac{E_0}{B_0}\right)^2 + V_z^2 = \left(\frac{E_0}{B_0}\right)^2, \tag{10}$$

i.e., the velocity hodograph is a circle (Fig. 1).

It is seen from the picture that the particle V_z vertically drifts towards V_y ($E_0/B_0 > 0$) while executing oscillations.

Then, we find the average value of the drift velocity V_y, as it defines the efficiency of the field effect on one or another process.

Time averaging (9), we obtain

$$\bar{V}_y = \frac{E_0}{B_0}[1 - \overline{\cos(\delta\sin\varphi)}],$$

where the line means the average value in the time $t \longrightarrow \infty$. Now, we use the relation for Bessel functions [9]:

$$\cos(\delta\sin\varphi) = I_0 + 2\sum_{n=1}^{\infty} I_{2n}(\delta)\cos 2n\varphi.$$

Taking into account the rules of averaging and the fact that $\overline{\cos 2ny} = 0$, we finally find

$$\bar{V}_y = \frac{E_0}{B_0}[1 - I_0(\delta)], \tag{11}$$

where $I_0(\delta)$ is a Bessel function of the first kind of zero order of the real argument δ. In the case of stationary fields, in (11), it should be taken that $\omega = -0$; i.e., $\delta = \frac{\omega_0}{0} = \infty$. Hence, for stationary fields,

$$\bar{V}_y = \frac{E_0}{B_0},$$

as $I_0(\infty) = 0$.

The $(\bar{V}_y B_0)/E_0$ versus δ characteristic diagram is presented in Fig. 2. As is seen, the average velocity passes via a series of peaks with decreasing magnitude. The average velocity achieves the largest value at $\delta = 3.8$, when

$$\bar{V}_{y\max} \cong 1.403 E_0/B_0. \tag{12}$$

The particle drift direction being independent of its charge sign means that both positive and negative particles migrate in one direction, thus making possible the application of crossed alternating fields with the aim of separating the charged subsystems using a more constructive procedure, including the method of division of charges on opposite sides when there appears a potential difference obstructing the motion.

The maximum average velocity of the particles motion is nearly half as much again as in the case of stationary fields. We estimate the frequency ω, wherein there is the first peak. Assuming $m \sim 10^{-26}$ kg, $q \sim 1.6 \times 10^{-19}$ K, and $B_0 \sim 10^{-3}$ T, we find $\omega_0 = 5$ kHz.

Such a frequency is easily achieved in actual practice.

Note that the growth of the particles' mass requires a proportional increase of the magnetic field induction to gain the maximum ($\delta = 3.8$), which, on the other hand, results in a decrease of the average velocity because of the multiplier E_0/B_0; therefore, the application of alternating fields is more preferable in order to remove microparticles from the medium, for instance, for demineralization.

If the masses are great and an increase of the magnetic field induction is undesirable, the process can be carried out at the further peaks, the next being achieved at $\delta \approx 10$, when $\bar{V}y_{\max} \sim 1.25E_0/B_0$.

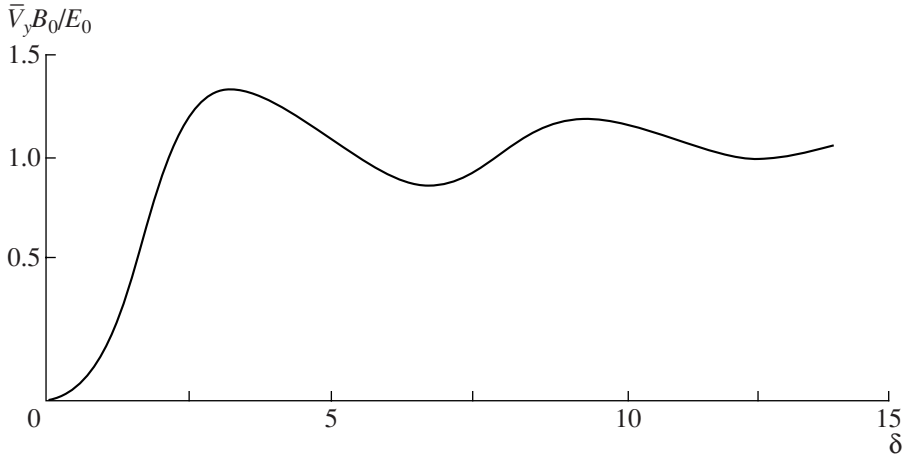

Fig. 2. The $(\bar{V}_y B_0)/V_0$ versus δ characteristic.

The particle velocities themselves reach a substantial magnitude with the field intensity being negligible. Thus, in the case of the above-mentioned numerical example at $E_0 \sim 1$ V/m, $V_{y\max} \sim 1.4$ km/s. Of course, it is a big quantity caused, first of all, due to the neglect of viscosity forces at the particle motion in real media. Therefore, the described effects should first and foremost show themselves in gases.

Finally, there is one more peculiarity of the effect of the crossed alternating synchronous fields on media, namely, the dependence of the average velocity V_y on the particle mass. Such a dependence makes it possible to withdraw one or another fraction from the closed phase through governing the frequency and induction of the magnetic field.

REFERENCES

1. Artsimovich, A.A. and Luk'yanov, S.Yu., *Dvizhenie zaryazhennykh chastits v elektricheskikh i magnitnykh polyakh* (Motion of Charged Particles in Electric and Magnetic Fields), Moscow: Nauka, 1972.
2. Povkh, I.L. and Chekin, B.V., *Magnitogidrodinamicheskaya separatsiya* (Magnetohydrodynamic Separation), Kiev: Naukova Dumka, 1978.
3. Slesarenko, N.N., *Sovremennye metody opresneniya morskikh i solenykh vod* (Modern Methods of Desalination of Sea and Salty Waters), Moscow: Energiya, 1973.
4. Usatenko, N.T., The Effect of Electrophysical Action on Water-Containing Liquid Systems, in *Magnitnaya obrabotka vodnykh system* (Magnet Treatment, Moscow), 1981.
5. Landau, L.D. and Lifshits, E.M., *Teoriya polya* (Field Theory), Moscow: Nauka, 1978.
6. Rossi, B.S. and Ol'bert, S., *Vvedenie v fiziku kosmicheskogo prostranstva* (Introduction into Space Physics), Moscow: Atomizdat, 1974.
7. Acasofu, S.I. and Chepmen, S, *Solnechno-zemnaya fizika* (Sun-Earth Physics), Part 2, Moscow: Mir, 1975.
8. Grosu, F.P., Bologa, M.K., and Kozhukhar', I.A., Charged Particle Motion in the Stationary Field of Plate Nonparallel Capacitor, *Elektron. Obrab. Mater.*, 2004, no. 3, pp. 28–36.
9. Yanke, E., Emde, F. and Let, F., *Spetsial'nye funktsii* (Special Functions), Moscow: 1977.

ISSN 1068-3755, Surface Engineering and Applied Electrochemistry, 2008, Vol. 44, No. 1, pp. 36–42. © Allerton Press, Inc., 2008.
Original Russian Text © N.I. Kuskova, V.Yu. Baklar', V.I. Gordienko, S.A. Khainatskii, 2008, published in Elektronnaya Obrabotka Materialov, 2008, No. 1, pp. 44–50.

ELECTRICAL PROCESSES
IN ENGINEERING AND CHEMISTRY

On Obtaining of Ultrafine Metal Powders at Electric Explosion of Conductors in Liquid Part I. Peculiarities of Explosion of Conductors in Liquid

N. I. Kuskova, V. Yu. Baklar', V. I. Gordienko†, and S. A. Khainatskii

Institute of Pulse Processes and Technologies of the National Academy of Sciences of Ukraine, pr. Oktyabr'skii 43-a, Nikolaev, 54018 Ukraine

e-mail: iipt@iipt.com.ua

Received October 1, 2007

Abstract—The features of electric explosion and dispersion in a liquid of metallic conductors with their thermodynamic and electric parameters differing over a wide range were investigated. The experimental data analysis allowed selecting three pairs of metals being the closest in the obtained parameters of the explosion. It is obvious that the size of the obtained particles depends on the density of the energy injected into the conductor mass unit by the moment of explosion. A reverse dependence between the energy of the arc stage of the explosion and the size of the particles is found. The distribution of the obtained particles by size is more homogeneous than at the explosion of conductors in gases.

DOI: 10.3103/S1068375508010080

One of the important practical applications of the electric explosion of conductors (EEC) is the possibility to obtain ultrafine powders (UFP) of various substances characterized by sufficient conductivity, in particular, metals. The EEC method allows rather simple obtaining of fine powders of chemical compounds uncontaminated by foreign impurities. It is possible to realize a number of reactions between substances relatively nonreactive to each other (that is, to synthesize chemical compounds that can hardly be obtained by other methods).

The EEC method consists of evaporation in a certain medium (air, liquid) of a metal sample with subsequent rapid cooling of the formed small metal particles (SMP) in this medium. The cooling rate may achieve values of 10^{10}–10^{15} K/s [1]. The conditions of the conductor explosion and cooling of its products determine both the sizes of the obtained particles and their chemical composition.

CONDITIONS OF THE EXPLOSION HOMOGENEITY

Depending on the rate and quantity of the injected energy, the explosion process may proceed in different modes. For copper conductors at current densities $j \leq 10^{11}$ A/m^2, the conductor destruction mechanism is realized, being due to development of constriction magnetohydrodynamic instability [2]; that is, the conductor explodes nonhomogeneously along the axis. In the process of its destruction, rather large fragments are formed, their sizes being comparable with the initial conductor diameter. At considerably higher current densities ($j \sim 10^{13}$ A/m^2), there is realized the explosion mechanism connected with the pressure inhomogeneity over the conductor cross section [3], whereat the conductor begins to evaporate from the surface. At the same time, it is indubitable that, at UFP obtaining, for obtaining of the minimal sizes of particles, it is important to establish conditions of the axial and radial homogeneities of the conductor explosion due to selection of the EEC mode and the conductor parameters.

Conditions of homogeneous (along the axis and over the cross section) explosion of cylindrical conductors in air and water have been studied in [3–6]. For semiconductor explosions in air, it is shown in [4] that all the parameters are homogeneous up to the moment of the explosion only for very thin conductors (with a diameter ≤0.1 mm). Experiments in this work were carried out at the current density $j \cong 1 \times 10^7$ A/cm^2. In [5, 6], there are studied radial conductor homogeneity (skin, magnetic pressure) and the axial one (the so-called "force"—screw and constriction as well as overheating) at underwater electric explosions. It is shown in [6] that, at selection of the "optimal" length and diameter, all the conductor parameters are homogeneous in the explosion process at all the stages of heating up to the transition into the plasma state; that is, the condition of the optimum is the condition of homogeneity.

Optimum conditions of semiconductor explosion, when the energy stored in the bank of capacitors is

† Deceased.

evolved during the first pulse of the discharge current with the maximal rate, were obtained in [1] from the requirement of the power maximum

$$\begin{cases} d_{\text{opt}} = 2\left[\dfrac{W_0}{z\rho_s\sigma_{s0}(\lambda_s+\gamma_s)}\right]^{1/4} \\ l_{\text{opt}} = 2\times 10^{-3}U_0\sqrt[4]{LC}. \end{cases} \quad (1)$$

Here, W_0 is the stored energy of the bank of capacitors, where $W_0 = CU_0^2/2$; ρ_s is the density; σ_{s0} is the specific electric conductivity; λ_s is the specific melting heat; γ_s is the specific heat of evaporation of the conductor metal; z is the wave (or characteristic) resistance of the circuit; $z = \sqrt{L/C}$; U_0 is the initial voltage on the bank of capacitors; C is the capacitance of the bank of capacitors; and L is the inductance of the discharge circuit. At the transition through the optimal mode (for example, voltage decrease), the explosion mechanism changes; that is, it becomes inhomogeneous. As one can see from (1), the optimal conductor length does not depend on the conductor characteristics, and, at similar parameters of the circuit, it is equal for all the exploded conductors, whereas the optimal diameter d_{opt} significantly depends on the physical characteristics of the conductor.

In addition to the optimum conditions of the conductor explosion, for the analysis of each stage of the explosion, we have used the similarity criterion of the electric characteristics of the explosion obtained by the author of [1]: S_1 (characterizing an approximate similarity of the initial stage of the explosion), S_2 (determining the phase of the explosion), and S_3 (determining the similarity of the stage next to the explosion stage). The latter criterion considerably depends on the conductor length; therefore, at adequate selection of the parameters, one can expect that the "arc" stage of the explosion will be similar or close for all the conductors.

Strictly speaking, ratios (1) and similarity criteria were obtained for aluminum and copper conductors; it is necessary to specify their applicability for the explosion of conductors of other materials.

BEHAVIOR OF METAL DISPERSION AT CONDUCTOR EXPLOSION

Calculation of the parameters of the circuit and the conductor carried out according to formulae (1) allows selection of the explosion mode providing uniform heating of the conductor both along its length and over its cross section up to the beginning of evaporation. Moreover, the rate of the energy evolution in the conductor is the maximum possible for all the parameters satisfying these ratios.

According to the data of [7], at optimal parameters for copper conductors in water, the energy evolved by the moment of the explosion exceeds by approximately 50% the sublimation energy. It is natural to suppose that all the metal mass has transited into the vapor phase by this time, and a situation may be realized when the phase trajectory envelops the critical point. Further growth of fine particles occurs by two possible mechanisms: either, at broadening of the explosion products, the vapor is overcooled and the process of homogeneous formation of the liquid phase develops or, at vapor cooling, collision of atoms, molecules, or molecular complexes leads to the appearance of the bound state and a subsequent increase of nuclei. In any case, small metal particles appearing as the result of volume condensation or cluster formation usually have a spherical form and average sizes in the range of 10–100 nm [8]. Detailed analysis of works concerned with consideration of electric conductor explosion as a method of dispersed powder obtaining and the results of experimental research given in [7] allowed us to find that the average SMP size is determined by the time–energy parameters of the given method; their phase composition and structural state are determined by the size of the formed particles and the physicochemical properties of the actuation medium. By changing these parameters, one can obtain SMP in various structural states: crystalline, quasi-crystalline, amorphous, and amorphous–crystalline. Application of various liquids as an actuation medium allows obtaining of SMP in the form of pure initial metals or their chemical compounds with products of decomposition of these liquids.

The dependence of the number–average diameter of the particles on the energy injected into the conductor obtained in [8] is approximated by the expression

$$\bar{a} = 0.3\times 10^{-6}(e/W_s)^{-3}, \text{ m}, \quad (2)$$

where $\bar{a}$ is the number–average diameter of the particles, e is the density of the energy injected into the conductor, and W_s is the energy of the metal sublimation. The experiments were carried out for aluminum and copper conductors in argon and hydrogen gases at pressures of $(1–9)\times 10^5$ Pa. The form of the particles that appeared is spherical (including the experiments where chemical reactions proceeded), and the pressure and nature of the gas surrounding the conductor do not influence the particle size. In [9], there is a statement that the transition from explosions with $e/W_s > 1$ to explosions with $e/W_s < 1$ may lead to a change of the particle formation mechanism from the condensation to coagulation one; this will be shown in their sizes and form. Taking into account that the explosion mechanism can also change (appearance of instabilities, inhomogeneous explosion, etc.), this will be shown more appreciably.

The experiment results in [10] show that, at $e/W_s \sim 2$, the average size of the obtained particles is $\bar{a} \sim 30$ nm; it is 50–60 nm at 1.5, 300 nm at 1, and >600 nm at 0.7–0.8. Taking into account the results of [7], for a copper conductor explosion in liquid, according to (2), it is possible to obtain SMP of about 50–60 nm. However,

Table 1

Metal	d_{opt}, mm	S_1	S_2	W_0/m, MJ/kg	W_a, J	I_m, kA	U_m, kV	R_{max}/R_0
Cu	0.3	0.12	0.21	27.0	787.9	15	50.7	200
Ni	0.44	0.21	0.91	27.3	783.1	11	41.5	35
Ti	0.71	0.67	6.46	53.6	673.5	8	24.6	7.7
NiCr	0.79	1.37	9.68	29.8	753.6	10	35.4	13.8
ЭИ	0.72	1.48	6.55	26.1	607.1	6	29	4.5
ВЖ	0.63	0.93	3.84	26.0	719.7	9	30	4.4

taking into consideration that the particle cooling rates at the conductor explosion in liquid are higher by several orders of magnitude than in gases, one can expect that these sizes will achieve values of 0.5–1 nm.

Application of ratio (2) for preliminary estimations and comparison of the results of experiments in liquid and gases is, to some extent, justified due to the following. According to [1], the form and value of the first current pulse at explosion are determined by the processes taking place in the conductor itself; they weakly depend on the surrounding medium nature. Therefore, they are identical for explosion in liquid and gases. Unfortunately, ratio (2), which according to the results of the cited works properly approximates the experimental results, contains an a priori undefinable parameter e. Hence, one of the aims in the research of the peculiarities of conductor explosion in liquid could be the definition of a number of macroscopic parameters or their combination that would allow determination of the approximate particle distribution by size for various metals proceeding from a priori specified electrotechnical parameters of the circuit and properties of the conductor or finding a correlation with these parameters.

EXPERIMENTAL RESULTS

For determination of the peculiarities of metal conductor explosion in liquid, conductors with thermophysical and electrophysical parameters differing over a wide range were taken. They were copper conductors, which are studied thoroughly enough, and conductors containing alloys of nickel (including chemically pure Ni) and titanium. The conductor explosion was carried out in distilled water; the RLC–circuit parameters were the following: the initial voltage on the bank of capacitors U_0 was 30 kV, the capacitance of the bank was C = 3 μF, and the circuit inductance L was 3 μH (the circuit characteristic oscillation period $T = 2\pi\sqrt{LC}$ was 18.85 μs, the characteristic impedance was 1 Ω, and the stored energy was W_0 = 1350 J). For cylindrical conductors (copper, nickel, or nichrome), the diameter $d \cong$ 0.3 mm was selected; for the foil (titanium and heat-resistant steels of the ЭИ-868 (ВЖ98]) and ВЖ100 brands), the width was selected so that the cross sectional area was equal to that of wires of about 7×10^{-8} m^2. The length of all the conductors was l = 80 mm. These parameters are close enough to the optimal ones for all the conductors applied in the experiments. Their certain difference from the optimal parameters was allowed with the intent to estimate the arc stage influence on the average sizes of the obtained SMP. For registration of the current and voltage, a resistance voltage divider, a low-inductance shunt, and an oscillograph (S8-17) were applied. The experiments for each exploded conductor were repeated not less than 5 times. The electric measurement spread was less than 2–3%. Copper and nickel conductors were used to verify the correspondence of the electrophysical parameters of the explosion for the conductors of round cross section and narrow foil ($l \gg h$). They appeared to be practically identical at the parameters selected by us.

The energy the parameters of each of several stages of the explosion were calculated from oscillograms of the current and voltage. According to [7], we considered the moment of the conductor explosion in the liquid to be the moment of the overvoltage peak.

Table 1 shows some results of the measurements and the explosion parameters calculated by them: the optimal conductor diameter d_{opt}, the similarity criteria S_1 and S_2, the ratio of the stored energy W_0 to the conductor mass m, the energy evolved at the active discharge stage W_a (without taking into account losses in the circuit elements and reactive losses), the maximal values of the current I_m and voltage U_m, and the maximal value of the exploded conductor resistance reduced to the initial one.

The optimal length for all the conductors is equal to l_{opt} = 104 mm, and the similarity criterion S_3 = 0.024 differs in the sixth decimal place; that is, the arc stage of the explosion does not strongly vary for all the conductors, since their lengths are equal. As one can see from the table, the optimal conductor diameters considerably differ. The similarity criteria "responsible" for the initial stage and the explosion phase are also appreciably different; this is in good agreement with the behavior of these processes for different conductors. One can argue this using superimposed oscillograms of the current and voltage at the explosion of the copper and steel (ВЖ100) conductors presented in the figure.

The row constructed for different conductors by decreasing W_a (Cu > Ni > nichrome > ВЖ > Ti > ЭИ)

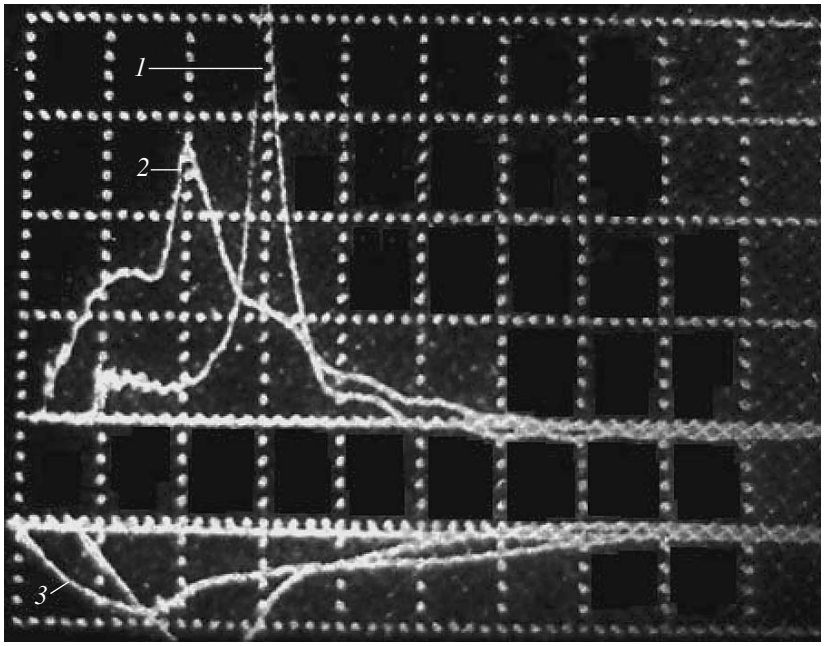

Superimposed oscillograms of current and voltage at explosion of copper and steel (ВЖ100) conductors: *1*—voltage oscillogram, copper; *2*—voltage oscillogram, steel; *3*—current oscillogram, copper.

is identical to the row by I_m and correlates with the row by R_{max}/R_0; here, differences are observed only for the "tail" row. The quantity of the energy evolved on the conductor and discharge channel in the explosion process (we call it the active discharge stage) and the maximal current must certainly depend on the character of the conductor resistance change, since this determines what part of the energy dissipates on elements of the accumulator and the discharge circuit. A peculiarity of the U_m row is that the titanium conductor shifts into the last position. Explosion of copper, nickel, and nichrome conductors is characterized by the overvoltage peak; for copper it is higher. The titanium conductor explodes at a voltage significantly lower than the initial voltage of the bank of capacitors.

The ratio of the maximal resistance to the initial one for copper and nickel properly correlates with the known results [1, 6]. For nickel, the second order phase transition and variation of the resistance temperature coefficient in the region of 630 K do not influence the resistance curve run. For the steel, titanium, and nichrome conductors, an obvious kink of the $R(t)$ curve at the moment of the beginning of the melting does not exist.

The time characteristics of the explosion process are presented in Table 2. Here, t_i is the time of the achievement of the first current maximum, t_{ex} is the explosion time (corresponding to the overvoltage peak), and t_m is the time of achievement of the energy evolution rate maximum W_i/t_i. Since the time corresponding to the power peak N_{max} for all the metals practically coincides with the explosion time t_{ex}, it is not given in Table 2.

Analysis of the experimental data presented in Tables 1 and 2 allows us to distinguish three pairs of metals being the closest in the explosion parameters. They are Cu and Ni, nichrome and ВЖ100 steel, and Ti and ЭИ-868 steel. The third pair of metals considerably differs from each other in all the thermo and electrophysical parameters. These metals are characterized by the following: the conductors prepared from them explode at a voltage less than U_0, and the explosion stage, for which S_2 is "responsible," insignificantly differs for them. Therefore, the forms of the oscillograms of the current and voltage for these conductors are almost identical. It should also be noted that, if the row by decreasing W_a is identical to the row by I_m, then the row by N_{max} corresponds to the row by U_m.

Table 3 gives values of the energy evolved at different stages of the conductor explosion. Here, W_1 is the energy consumed for the conductor heating up to the melting temperature; W_2, for melting; W_3, for heating

Table 2

Metal	t_i, μs	t_{ex}, μs	N_{max}, 10^8 W	t_m, μs	W_i/t_i, 10^8 J/s
Cu	3.9	4.5	6.7	5	1.5
Ni	3.0	3.0	4.2	3.9	1.5
Ti	2.8	3.03	1.6	3.9	1.1
NiCr	3.6	3.73	2.72	5	1.3
ЭИ	2.7	2.89	1.61	3.5	1
ВЖ	3.4	3.81	2.51	4.6	1.3

Table 3

Metal	W_1, J		W_2, J		W_3, J		W_4, J		W_s		
	exp.	theor.	exp.	theor.	exp.	theor.	exp.	theor.	exp.	theor.	
										b	s
Cu	23.5	21.1	27.5	10.3	66.9	29.5	329.2	241.6	447.1	302.5	415.4
Ni	47.1	31.6	30.2	15.0	82.1	29.3	161.5	320.8	320.9	396.6	560.1
Ti	18.9	22.0	20.4	8.2	16.8	21.2	214	226.2	270.1	277.6	389.6
NiCr	22.8	31.1	12.2	14.5	35	31.9	301.5	339.3	371.8	416.7	581.8
ЭИ	26.3	28.0	22.4	25.1	26.9	27.0	191.3	562.3	266.9	642.5	763.9
ВЖ	22.8	29.2	21.1	25.5	25.4	27.7	296.9	575.1	366.2	617.1	733.5

Table 4

Metal	W_s/W_0			W_{ex}/W_s		W_s/W_{arc}			W_{sa}	$\bar{a}$, 10^{-6} m	
	exp.	theor.				exp.	theor.				
		b	s	b	s		b	s		b	s
1	2	3	4	5	6	7	8	9	10	11	12
Cu	0.39	0.23	0.32	1.64	1.2	0.65	0.3	0.47	1.71	0.07	0.18
Ni	0.25	0.31	0.44	0.81	0.57	0.34	0.46	0.8	0.78	0.57	1.61
Ti	0.20	0.21	0.29	0.97	0.69	0.25	0.26	0.41	0.67	0.33	0.9
NiCr	0.28	0.31	0.43	0.89	0.64	0.38	0.45	0.76	0.97	0.42	1.1
ЭИ	0.18	0.48	0.57	0.38	0.32	0.22	0.91	1.3	0.66	5.59	9.4
ВЖ	0.27	0.49	0.58	0.56	0.47	0.37	0.95	1.38	1.04	1.74	2.93

up to the boiling temperature; and W_4, for boiling. The experimental values of the given quantities were calculated from oscillograms, and the theoretical values are an approximate calculation with constant coefficients. The energy of the conductor sublimation (complete evaporation) W_s was calculated for two possible (limiting) cases: when the conductor evaporates equilibrium wise (by the bimodal line (b)), and when the spinodal conductor destruction occurs (s). The energy evolved in the conductor by the moment of the explosion was taken as the experimental value of W_s. In a number of cases, on voltage oscillograms for various conductors, there were absent obvious characteristic kinks corresponding to phase transitions; this caused difficulties in determination of the respective characteristics. This, together with some difficulties in determination of the required time intervals, could cause discrepancies between the theoretical and experimental data.

According to the data of Table 3, one can suppose that the conductors most likely evaporate equilibrium wise (probably, excluding the copper ones), although it is well known that the theoretical calculation in our approximations gives overestimated values of the sublimation energy. The problem is the accuracy of the thermophysical tabular data for "extreme" states of the metals, for example, the critical temperature or specific heat of evaporation for refractory metals. Therefore, the results given in Table 3 may be considered as estimated ones only.

Table 4 shows a number of energy ratios determining both the explosion nature and the possible size of the metal particles obtained. Columns 2–4 give the ratio of the sublimation energy W_s (calculated by two possible processes and experimental ones) to the stored energy W_0. Columns 5 and 6 present ratio of the energy evolved in the conductor by the moment of the explosion W_{ex} (determined by the oscillograms) to W_s calculated by the two processes. The ratio of the sublimation energy to the "arc discharge" energy estimated as $W_s/(W_0 - W_s)$ is given in columns 7–9. Column 10 contains the ratio of the explosion energy to the "arc discharge" energy calculated by the ratio $W_{sa} = W_{ex}/(W_a - W_{ex})$, where W_a is the experimentally determined total energy evolved at the active stage in the discharge channel (without taking into account losses in the discharge circuit elements). Columns 11 and 12 give values of the number–average diameter of the particles calculated by (2). The density of the energy injected into the conductor by the moment of the explosion was calculated from the oscillograms of the current and voltage; the sublimation energy was taken as bimodal and spinodal.

According to Table 4, the closest parameters of the explosion are still observed for the same pairs of conductors: copper and nickel, titanium and ЭИ-868, nichrome and ВЖ100. This is also confirmed by the oscillogram form. For titanium and ЭИ-868, the forms of the oscillograms of the current and voltage are almost identical; for nichrome and ВЖ100, they are very close. The voltage oscillograms for copper and nickel are similar in form; however, they strongly differ in the value and duration of the "shelf" corresponding to the melting.

The data of Table 4 confirm once again that, at the parameters selected in the experiment, the process of the conductor evaporation proceeds equilibrium wise. Taking into account the losses in the circuit at the conductor explosion, one can suppose that, for conductors of copper, nichrome, and steel (ВЖ100), the main part of the energy is evolved at the stage of the explosion, whereas, for the other three conductors, the explosion products are significantly "additionally heated" at the arc stage. It is probable that, for them, it is necessary to determine the moment of explosion by other criteria, for example, by the moment of a kink appearance on the decaying voltage part.

As to the calculated values of the average size of the particles, they are the lowest for copper conductors. The row by decreasing $\bar{a}$ (ЭИ > ВЖ > Ni > nichrome > Ti > Cu) coincides for calculation of W_s by both possible processes. The statement that $\breve{a}$ monotonously decreases as the density of the energy injected into the conductor increases [9] is not confirmed in our case: the row by W_s has the form ЭИ < Ti < Ni < ВЖ < nichrome < Cu (let us remember that all the conductors had equal volume). Only extreme points of both rows coincide; the other conductors do not obey this regularity. The calculated (and, accordingly, experimental) size of the particles correlates more accurately with the density of the energy injected into the conductor mass unit by the moment of explosion; in this case, only Ti "falls out" of the row. Nevertheless, it is early to make a final conclusion on the correlation of the value of the number–average diameter of the particles calculated by (2) with the thermo- or electrophysical metal parameters. Only the minimal size of the particles for Cu could be understood through insight: in comparison with the other metals, it is characterized by the lowest boiling temperature and evaporation heat. For Ti, due to the relatively low density, all the specific characteristics are high enough; however, this did not influence the particle sizes in our experiment. We failed to reveal a dependence on any parameter "inside" the group of Ni alloys—neither on the nickel concentration nor on the characteristics of impurities.

It was of interest to verify the influence of the arc discharge stage on the particle sizes, which was mentioned in [9], for our results on conductor explosion in water. According to the data of Table 4, the ratio of the energy evolved by the moment of explosion W_{ex} to the energy evolved at the arc stage W_{arc} tentatively divides the conductors into 3 groups. The first one consists of the copper conductor only, for which $W_{sa} = 1.71$; here, the value of W_{arc} is hardly significant. The second group contains nichrome and ВЖ, for which the energy W_{arc} (including, naturally, the energy of the second breakdown ignition being high) is approximately equal to the conductor explosion energy. At last, the third group consists of Ni, Ti, and ЭИ, for which $W_{arc} > W_{ex}$. That is, the row by W_{sa} takes the following form: ЭИ > Ti > Ni > nichrome ≈ВЖ > Cu; again Ti and ВЖ have interchanged places. Thus, it can be considered that the correlation between the arc stage and the particle size must take place for ЭИ > Ni > nichrome > Cu (Ti and ВЖ have fallen out); moreover, the dependence is inverse to that given in [9]—the less the energy evolved at the arc stage the less the particle size. It is no wonder that the formula for calculation of $\breve{a}$ does not contain the arc stage parameters.

Comparison of the obtained results with the experimental data of [10] shows that, at $e/W_s \sim 1.7$ for copper, the average size of the obtained particles calculated by us is $\bar{a} \sim 70$ nm, approximately the same as in this work. Photographs of the material of the conductor explosions in air and water at identical parameters made by the device "Neofot 1000" have shown that, in the second case, the particle distribution by size is more homogeneous. Indirect techniques of calculation of the number–average diameter of the particles according to these photographs have given values for $\bar{a}$ less by a factor of 3–4 than those given in Table 4; this counts in favor of significant differences in the conditions of SMP formation at conductor explosion in gases and condensed media.

Taking into account that, in the aspect of the energy characteristics of the explosion, our data on the conductor explosion in water differ strongly enough from the data given in [8–10] for explosion in gases, the differences (and similar features) of the explosion parameters in dependence on the properties of the surrounding medium should be revealed in detail.

REFERENCES

1. Krivitskii, E.V., *Dinamika elektrovzryva v zhidkosti* (Dynamics of Electric Explosion in Liquid), Kiev: Naukova Dumka, 1986.
2. Kolgatin, S.N., Lev, M.L., Peregud, B.P., Stepanov, A.M., Fedorova, T.A., Furman, A.S., and Khachatur'yants, A.V., Destruction of Copper Conductors at the Current of a Density Higher Than 10^7 A/cm^2 Passing in Them, *Zh. Tekh. Fiziki*, 1989, vol. 59, issue 9, pp. 123–133.
3. Kuskova, N.I. and Tkachenko, S.I., Theoretical Study of Dynamics of Phase Transitions in the Result of Microsecond Electric Explosions of Cylindrical Conductors, *Ukrains'kii Fizichnyi Zhurnal*, 1999, vol. 44, no. 3, pp. 351–356.

4. Lebedev, S.V. and Savvatimskii, A.I., Metals in the Process of Rapid Heating by High Density Electric Current, *Usp. Fiz. Nauk*, 1984, vol. 144, issue 2, pp. 215–250.
5. Kuskova, N.I., Tkachenko, S.I., and Koval, S.V., Investigation of Liquid Metallic Wire Heating Dynamics, *Journ. Phys.: Condens. Matter,* 1997, vol. 9, pp. 6175–6184.
6. Kovavl', S.V., Krivitskii, E.V., and Rakovskii, G.B., Research of High Temperature Properties of Metals by the Method of Underwater Electric Explosion of Conductors, *Preprint of Electrohydraulics Design–Construction Department, Acad. Sci. Ukrainian SSR,* Nikolaev, 1989, no. 7.
7. Litvinenko, V.P. and Koval', S.V., To the Problem of Correlation of the Electric and Space–Time Characteristics of Electric Explosion of Conductors, *Zh. Tekh. Fiz.,* 1983, no. 4, pp. 770–773.
8. Yavorovskii, N.A., Electric Explosion of Conductors as a Method of Obtaining of Ultrafine Powders, *Extended Abstract of Cand. Sci. (Eng.) Dissertation*, Kirov Polytechnical Institute, Tomsk, 1982.
9. Lerner, M.I., Control of the Process of Fine Particle Formation in Conditions of Electric Explosion of Conductors, *Extended Abstract of Cand. Sci. (Eng.) Dissertation*, Kirov Polytechnical Institute, Tomsk, 1988.
10. Kotov, Yu.A. and Yavorskii, N.A., Research of Particles Formed at the Electric Explosion of Conductors, *Fiz. Khim. Obrab. Mater.*, 1978, no. 4, pp. 24–29.

ISSN 1068-3755, Surface Engineering and Applied Electrochemistry, 2008, Vol. 44, No. 1, pp. 43–49. © Allerton Press, Inc., 2008.

ELECTRICAL PROCESSES
IN ENGINEERING AND CHEMISTRY

Effect of Heating on Palygorskite and Acid Treated Palygorskite Properties[1]

N. Frini-Srasra[a, b] and E. Srasra[a]

[a] *Unité Matériaux, CRTE, Technopole Borj Cedria, B.P.95-2050 Hammam-Lif Tunisia*
e-mail: nfrini@gmail.com
[b] *Département de Chimie, Faculté de Sciences de Tunis, 1060 Tunis, Tunisia*

Received September 10, 2007

Abstract—The behavior of palygorskite as an adsorbent or catalyst support is governed mainly by the magnitude of its surface areas and degree of surface activity. Most heterogeneous catalytic reactions take place at elevated temperatures. It is important and necessary to known the possible changes in the physicochemical properties and hence the catalytic activity due to the thermal treatment. The present work investigates the effect of heat treatment on the surface and textural properties of palygorskite and acid activated palygorskite. Samples were heated at the required temperatures (150°C, 350°C, 550°C and 750°C) for four hours. The chemical analysis, X-ray diffraction, thermal analysis, and textural properties evaluated on the basis of the nitrogen adsorption have been reported for different samples. Acid-treated samples showed a shift of the DTA curves maxima to low temperatures with increasing acid treating time. The weight loss observed between 300–900°C was approximately half of the value observed for the untreated mineral over the same temperature range. On heating, water molecules are removed causing changes in the BET surface area and the porosity. The modification as a function of the temperature differs with the samples. However, at 750°C, a noticeable decrease of the surface area, which is attributed to closure of the mesoporosity, was observed for all the samples.

DOI: 10.3103/S1068375508010092

INTRODUCTION

Palygorskite has a fibrous structure consisting of talc-like ribbons parallel to the fibre axis assembled in such way that the tetrahedral sheet is continuous throughout but inverts in apical directions in adjacent ribbons, each ribbon alternating with channels along the fibrous axis. Octahedral cations present at the edges of the ribbons complete their coordination with water molecules (coordination water). Additional water molecules are hydrogen bonded to the water of coordination both at the external surfaces and within the channels (zeolitic water) [1].

Important characteristics relating to palygorskite applications are the particle size, particle shape, surface area, porosity, acidity, and surface chemistry, together with other physical and chemical properties specific to a particular application. All of these mineral properties are affected by thermal and chemical treatment such acid activation.

Since the diffusion mechanism in solids depends on the pore size distribution, knowledge of its surface, texture, and porosity is necessary to determine the sorptive response to the molecules of different size and shape.

The dehydration of palygorskite has been studied by many authors [2–7] and showed that water is present in three different structural positions: adsorbed and zeolitic water, bound water or crystal water, and hydroxyl water. The bound and hydroxyl water are more strongly held in the palygorskite structure and require a higher temperature for their expulsion. All these studies were concerned with the structural changes taking place above 300°C, which are due to the loss of bound and hydroxyl water, because loss of zeolitic water was considered to have no affect on the structure.

The temperature at which bound water begins to be expelled varies from sample to sample and is probably dependent on a number of factors, one of which is the Al/Mg ratio; samples rich in Mg generally lose their bound water at higher temperatures [8].

Table 1. Chemical compositions of untreated and acid treated samples expressed in the oxide form/100 g of the calcined sample

Samples	SiO_2	Fe_2O_3	MgO	Al_2O_3
Paly	63.69	7.023	14.34	14.26
Paly2M2h	69.72	6.11	12.54	11.96
Paly2M17h	71.4	5.96	11.89	11.09
Paly2M40h	80.90	3.37	8.12	8.01

[1] The text was submitted by the authors in English.

Acid activation of sepiolite and subsequent heat treatment were investigated by several authors. Study of the specific surface area and determination of the surface acid centers during thermal treatment of acid preactivated samples was established respectively by Lopez Gonzalez et al., 1981 [9] and Bonilla et al., 1981. [10]. Changes in the pore structure were investigated by Rodriguez et al., 1981 [11] and Balci, 1996 and 1999 [12, 13]. However, similar studies for palygorskite are missing.

The aim of this research is to study by the technique ATG-ATD, DRX, and adsorption isotherms of N_2 the textural and textural changes caused by thermal treatment of palygorskite and acid activated palygorskite. In order to prove such changes, we first verified the temperatures at which there is mass loss by thermal analysis and then every sample was subjected to thermal treatment at a fixed temperature for four hours. The effects of the thermal treatment on the pore structure of the palygorskite and acid treated palygorskite were investigated.

MATERIAL AND METHODS

Red palygorskite from south Tunisia was used as the starting material. Its chemical composition is the following: SiO_2 53.5%, Al_2O_3 11.98%, MgO 12.05%, Fe_2O_3 5.9%, K_2O 0.72%, Na_2O 0.03%, CaO 0.09% and 16% lost weight; its structural formula established according to Bailey in 1980 [14] is as follows:

$$(Si_{7.324}Al_{0.676})(Mg_{2.459}Al_{1.257}Fe_{0.608})(K_{0.125}Na_{0.008}Ca_{0.013})O_{20}(OH)_2(H_2O)_44(H_2O).$$

The cation exchange capacity (CEC) carried out by the Rjeldahl method is 23 meq /100 g and its specific surface is 67.4 $m^2\ g^{-1}$. The purified palygorskite sample was subjected to an acid treatment. The acid activation of the fibrous clay was obtained by contacting the clay with a 2 M solution of hydrochloric acid (the solid/liquid ratio was 10/100 wt %) at boiling temperature under reflux for different periods. After the treatments, the resulting solids were washed with distilled water until no chloride anions could be detected and no increasing pH was observed. The chemical compositions of the untreated and acid treated samples in octahedral and tetrahedral cations expressed in the oxide form/100 g of the calcined sample were given in Table 1.

The resulting samples and the purified palygorskite were heated at the required temperatures (150°C, 350°C, 550°C, and 750°C) after each water loss for 4 h. The DTA and ATG curves were recorded simultaneously at an average heating rate of 10°C/min with a simultaneous thermobalance analyser (Setaram 92).

Activated and nonactivated palygorskite before and after heating at different temperature were characterized by chemical analysis [15], X-ray diffraction (using a Pan analytical X'Pert High Score Plus diffractometer equipped with a Cu anticathode), and the specific surface area (using a Micrometric Autosorb 2050 Analyser). The last was determined from the nitrogen adsorption isotherms at 77 K by the BET method and after out degassing the samples at 150°C with a residual pressure of 10^{-5} mm Hg.

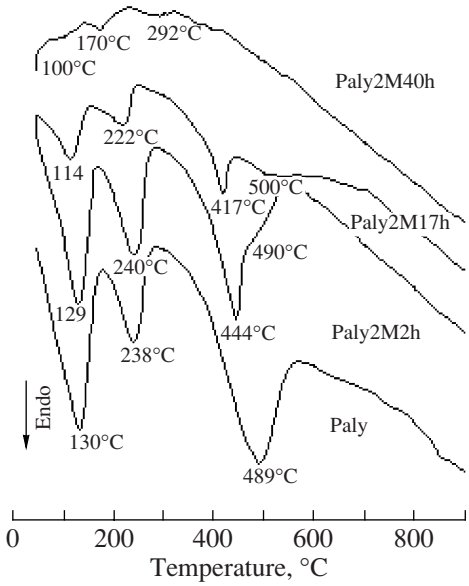

Fig. 1. DTA curves of untreated and acid treated palygorskite.

RESULTS AND DISCUSSION

DTA Curves

DTA curves of untreated and acid treated palygorskite are presented in Fig. 1. The DTA curve of the untreated palygorskite shows three endothermic reactions with peak maxima at 130°C, 238°C, and 489°C. The maxima shifted to low temperatures with increasing acid treatment time. The DTA curve of the Paly2M40h sample was different: the peaks were broad and appear at low temperatures of 100, 170, and 292°C, respectively, indicating that, at this stage of the acid treatment, the crystal structure undergoes drastic change.

TGA-DTGA Curves

Figure 2 shows the relative loss of weight of the original and acid treated palygorskite. The loss of weight was caused by the release of the different water

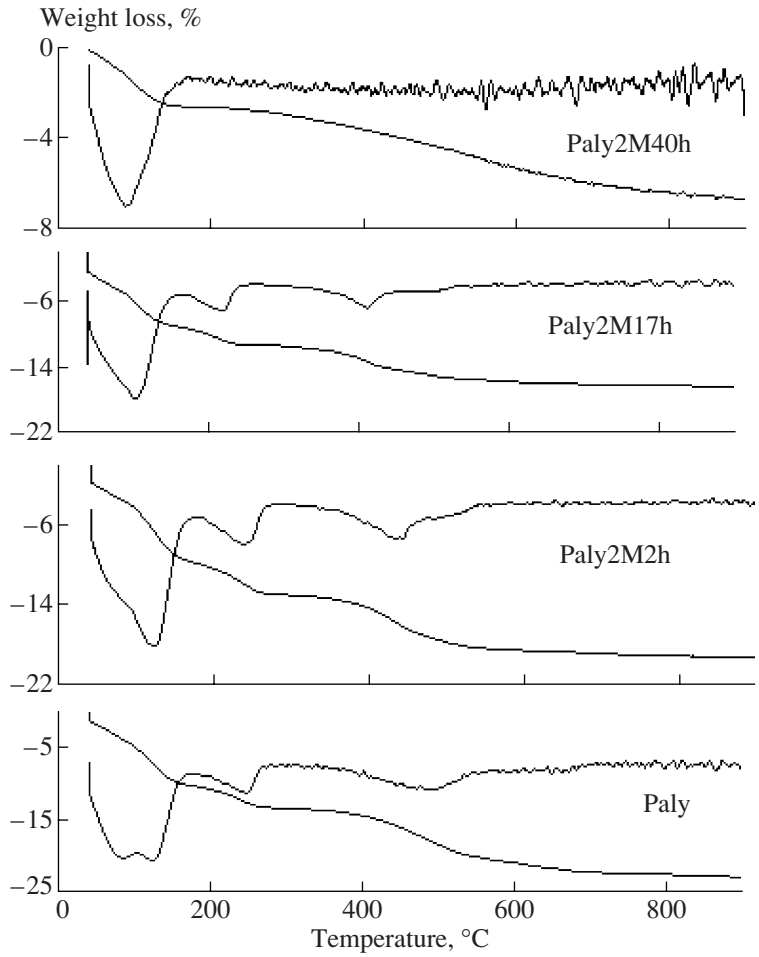

Fig. 2. TGA and DTGA curves of palygorskite before and after acid activation.

molecules in palygorskite (hygroscopic water, zeolitic water, bound water, and structural water), all of which leave the mineral at different temperatures up thermal treatment. The dehydration was completed at about θ = 750°C. In the low temperature region (<180°C), the DTGA curve shows two clear peaks corresponding to the weight losses of 7.8 and 5.34%. The two effects have been attributed to loss of Hydroscopic water and of some zeolitic water.

Theoretically, palygorskite contains four zeolitic water molecules, four bound water molecules, and two hydroxyl groups owing the loss of one molecule of

Table 2. Thermal weight loss (%) at various stages of the thermal analysis of untreated and acid treated palygorskite

	θ_1 = 25–180°C		θ_2 = 180–300°C	θ_2 = 300–750°C
Paly	θ < 120°C	120°C < θ < 180°C	4	12.4
	7.8	5.34		
	$3H_2O$	2.05	$1.54H_2O$	$4.77H_2O$
	H_2O_{Zeol}		$0.33H_2O_B + 1.21H_2O_{Zeol}$	$3.77H_2O_B + H_2O_{Hyd}$
	$2.36H_2O_{Hyg} + 0.74H_2O_{Zeol}$			
Paly2M2h	11.76		3.92	6.86
Paly2M17h	10.87		3.08	5.52
Paly2M40h	2.75		4.33	

Note: H_2O_{Hyg}—hygroscopic water; H_2O_{Zeol}—zeolitic water; H_2O_B—bound water; H_2O_{Hyd}—hydroxyl water.

Table 3. Textural data of different samples as a function of the thermal treatment temperature

θ, °C	Paly		Paly2M2h		Paly2M17h		Paly2M40h	
	S_{BET} $m^2 g^{-1}$	Vp $cm^3 g^{-1}$	S_{BET} $m^2 g^{-1}$	Vp $cm^3 g^{-1}$	S_{BET} $m^2 g^{-1}$	Vp $cm^3 g^{-1}$	S_{BET} $m^2 g^{-1}$	Vp $cm^3 g^{-1}$
25	67.4	0.0662	136.9	0.1123	279.1	0.0096	317.6	0.2902
350	74.2	0.074	114.9	0.0929	266.5	0.2090	365.9	0.3225
550	85.9	0.0763	116.2	0.1003	149.1	0.1398	384.2	0.3445
750	60.7	0.0566	99.4	0.0891	136	0.1232	276	0.2539

water. On the other hand, according to the chemical formula, one molecule of water presents 2.6% of the weight of the calcined sample. Experimental data (Table 2) show an overlapping of different losses. Determination of the water molecule number released at different stages shows that more than half of the zeolitic water is lost by 180°C. The rest of the zeolitic water is lost between 180–300°C. The loss of structural water occurred at higher temperature. The corresponding weight loss on the TGA curve (12.4%) has been assigned to the release of 3.77 molecules of bound water together with water from hydroxyl groups.

The acid-treated samples showed different thermal behavior due to their rearranged crystal structure and their chemical composition. Acid activation caused the removal of some parts of the hydroscopic and zeolitic water before the heat treatment. Consequently, the observed weight loss up to 300°C was about 14% instead of 17.14%. Moreover, acid treatment causes the removal of Mg and Al, during which some of the bound water and structural water associated with the Mg and Al coordinate may be taken away before thermal dehydration. The weight loss observed between 300–900°C was approximately half of the value observed for the untreated mineral over the same temperature range. Similar behavior was observed for sepiolite [12, 13, 16, 17].

The water content in the fully amorphized sample (Paly2M40h) is lower than in the original and not totally destroyed samples. In this case, the TGA curve shows only two weight losses (corresponding to 7.08%) and the DTGA curve enables the detailed determination of the dehydratation and dehydroxylation steps.

X-RAY DIFFRACTION

The X-ray diffractograms of the purified and acid treated samples heated at different temperatures are presented in Fig. 3. The untreated palygorskite has sharp strong reflections at 10.5, 6.4, 5.4, 4.5, 3.68, and 3.23 Å. With increasing acid treating time, the crystallinity of the palygorskite decreased with the concomitant formation of an amorphous phase. The latter can be observed by the appearance and increase of broad reflections at 16°–30° 2θ. After 40 h of treatment, only this is observed indicating the complete destruction of the clay. When the untreated material was heated at 350°C for 4 h, the 10.5 Å reflection decreased and the new reflections at 9.05 and 4.49 Å appeared. These reflections were considered to be due the presence of palygorskite anhydride [18]. The presence of both sets of reflections in the diffraction pattern implies that dehydration is nonuniform, part of the structure being dehydrated, while part remains intact. The 10.5 and the 9.05 Å reflections disappeared at 550°C. After treatment at 750°C, the structure was broken into an amorphous phase. The diffractograms of both the Paly2M2h and Paly2M17h samples show the presence of palygorskite anhydride only after heating at 550°C, while Paly2M40h isn't affected by the thermal treatment.

SPECIFIC SURFACE

The change in the pore structure and properties resulting from treatment with the HC1 2 M solution for various periods of time were investigated. Nitrogen adsorption–desorption isotherms of the original and acid treated samples are shown in Fig. 4a. Data resulting from the adsorption isotherms concerning the textural characteristics are given in Table 3. Nitrogen adsorption–desorption isotherms for natural and activated palygorskite correspond to type II in the IUPAC classification with a small hysteresis loops. The type of these isotherms is the same in palygorskite and activated solids and persists even in the 2M40H sample, which is mainly formed by the silica generated during the acid attack. The value of the surface area (calculated by application of the BET equation) increases as the treatment progresses. Natural palygorskite has a surface area of 67.4 $m^2 g^{-1}$. The increase in the surface area from the natural palygorskite to the sample treated with 2 M at a different time is mainly related to the elimination of octahedral cations and the generation of silica. No creation of microporosity is observed, but the activation increases the total pore volume from 0.0662 to 0.2902 $cm^3 g^{-1}$ due to the development of mesoporosity.

The thermal treatment doesn't affect the type of adsorption–desorption isotherm (Fig. 4b). However, during dehydration, the pore structure and the surface area of the mineral are affected due to changes in the

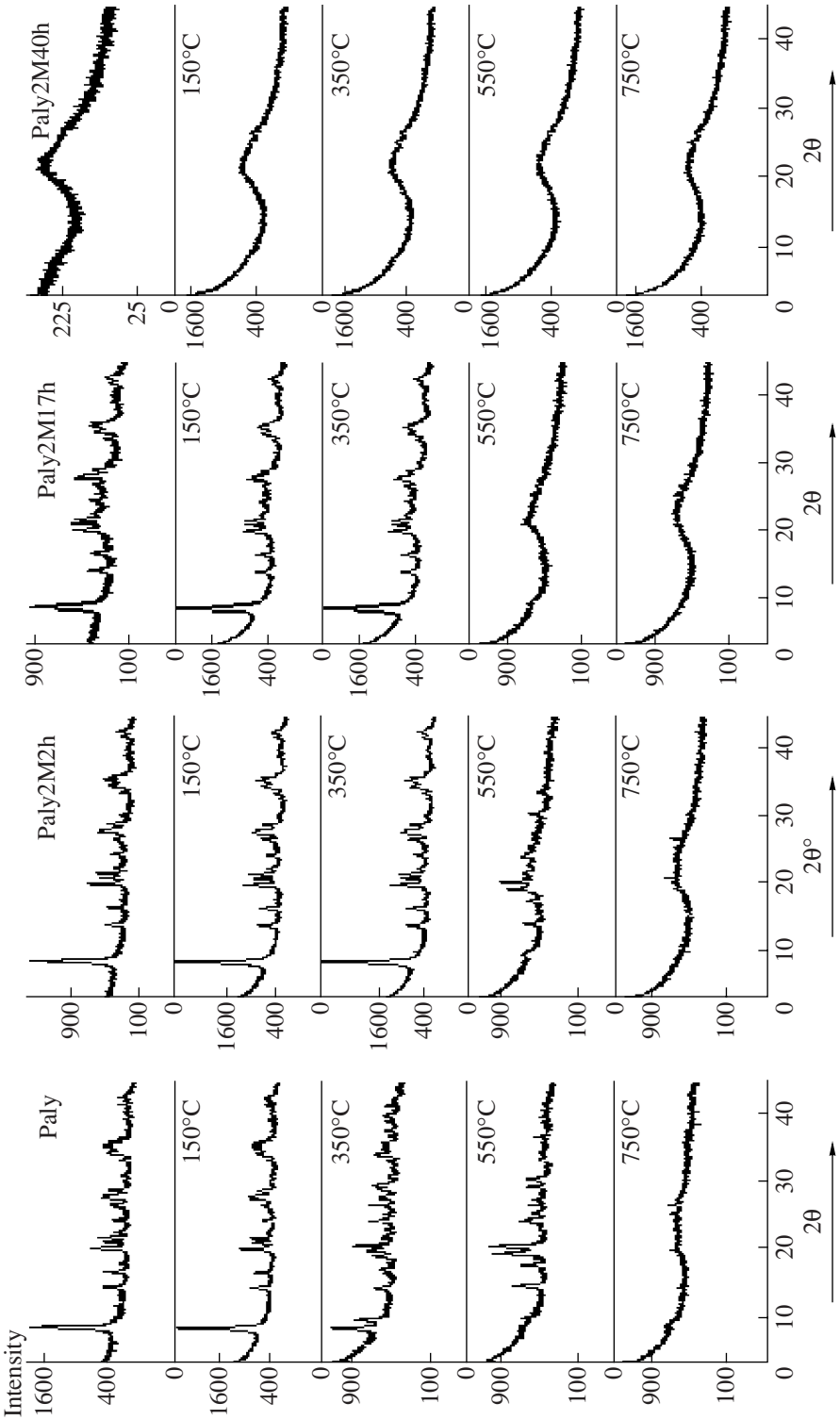

Fig. 3. X-ray diffraction patterns of different samples as a function of the temperature of the thermal treatment.

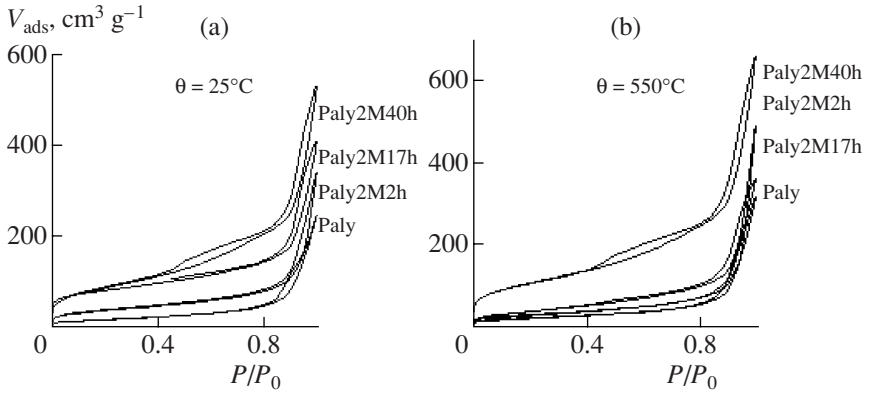

Fig. 4. Nitrogen adsorption–desorption isotherms of the original and acid treated samples at 25°C (a) and 500°C (b).

crystal structure (Table 3). The evolution of the specific surface area and pore volume given in Fig. 5 shows the different behaviors with the thermal treatment. In both the natural and 2M40h samples, the surface increases first as adsorbed and zeolitic water are eliminated until a maximum is reached. Next, up to 550°C, a sudden drop occurs. For the Paly2M2H and Paly2M17h samples, the surface area and porosity decrease continually. The heat treatment at 750°C produces a noticeable decrease of the surface area caused by closure of the mesoporosity for all the samples.

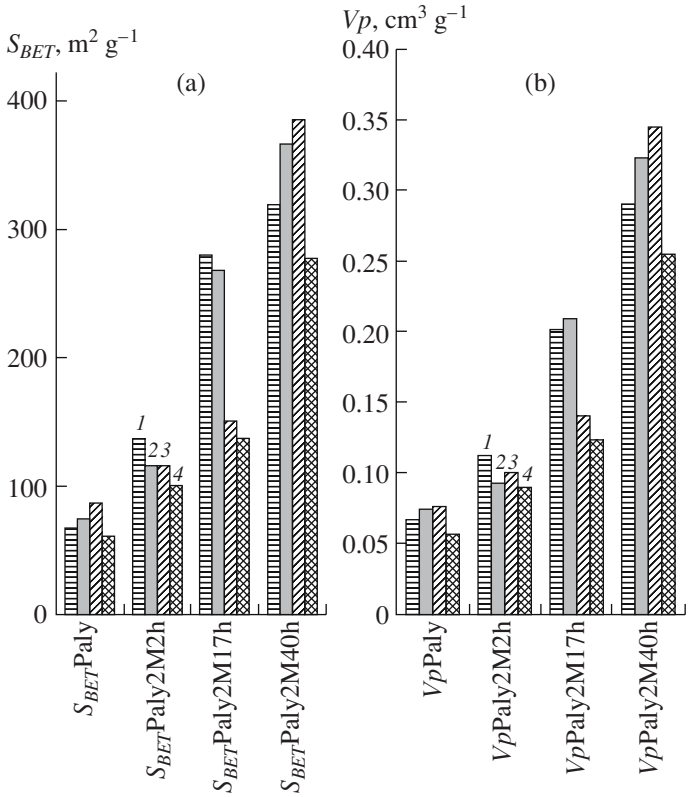

Fig. 5. Specific surface area (a) and pore volume (b) evolution with thermal treatment. *1*—25; *2*—350; *3*—550; *4*—750°C.

Comparing the unheated samples to the ones treated at 750°C, we notice that the Paly2M17h sample has the most altered structure; its specific surface area decrease to 136 from 279 m^2 g^{-1}.

CONCLUSIONS

The XRD study shows that the dehydratation is non-uniform. The thermal analysis shows an overlapping of different water losses. The N_2 adsorption–desorption data reveal textural modifications by the chemical and thermal treatment. The removal of zeolitic water molecules from the channels of the mineral causes an increase both in the BET surface area and porosity. On the other hand, the acid treatment caused the leaching of some inorganic parts of the mineral other than the removal of water. This leaching might decrease the strength of the pore walls, which results in the pore wall opening. Hence, acid pretreatment might increase the amount of meso- and macropore volume. The presence of macropores and mesopores (pores with larger dimensions) play a significant role where adsorption and/or chemical reaction take place.

REFERENCES

1. Serratosa, J.M., *Int. Clay Conference*, 1969, vol. 99.
2. Caillère, S. and Henin, S., *The X-ray Identification and Crystal Structures of Clay Minerals*, Brown, G., Ed., 1961, ch. VIII, IX.
3. Mifsud, A., Rautureau, M., and Fornes, M., *Clay Miner.*, 1978, vol. 13, pp. 367–374.
4. Shuali, U., Yariv, S., Steinberg, M., Muller-Vonmoons, M., Kahr, G., and Rub, A., *Clay Miner.*, 1990, vol. 25, pp. 107–119.
5. Shuali, U., Yariv, S., Steinberg, M., Muller-Vonmoons, M., Kahr, G., and Rub, A., *Clay Miner.,* 1991, vol. 26, pp. 497–506.

6. Cases, J.M., Grillet, Y., François, M., Michot, L., Vlliéras, F., and Yvon, J., *Clays Clay Miner.*, 1991, vol. 39, no. 2, pp. 191–201.
7. Frost, R.L. and Ding, Z., *Thermochim. Acta,* 2003, vol. 397, pp. 119–128.
8. Nathan, Y., *Int. Clay Conference*, 1969, vol. 91–98.
9. Lopez-Gonzalez, J. De D., Ramirirez-Saenz, A., Rodriguez-Reinoso, F., Valenzuela-Calahorro, C., and Zurita-Herrera, L., *Clay Minerals* (in Spanish), 1981, vol. 16, pp. 103–113.
10. Bonilla, J.L., Lopez-Gonzalez, J. De D., Ramirirez-Saenz, A., Rodriguez-Reinoso, F., and Valenzuela-Calahorro, C., *Clay Miner.*, 1981, vol. 16, pp. 173–179.
11. Rodriguez-Reinoso, F., Ramirirez-Saenz, A., Lopez-Gonzalez, J. De D., Valenzuela-Calahorro, C., and Zurita-Herrera, L., *Clay Miner.*, 1981, vol. 16, pp. 315–323.
12. Balci, S., *J. Chem. Tech. Biotechnol.*, 1996, vol. 66, pp. 72–78.
13. Balci, S., *Clay Miner.*, 1999, vol. 34, pp. 647–655.
14. Bailey, S.W., *Structures of Layer Silicates: in Crystal Structures of Clay Minerals and Their X-ray Identification,* Brindley, G.W. and Brown, G., Eds., London: Mineralogical Soc., 1980, pp. 2–123.
15. Solgic, Z. and Marjanovic-Krajovan, Y., *Chimie Analytique*, 1968, vol. 50, pp. 122–127.
16. Corma, A., Perez-Pariente, J., Fornes, V., and Mifsud, A., *Clay Miner.*, 1984, vol. 19, pp. 673–676.
17. Campelo, J.M., Garcia, A., Luna, D., and Marinas, J.M., *Mater. Chem. Phys.*, 1989, vol. 24, pp. 51–70.
18. Preisinger, A., *Clays Clay Miner.* (Proc. 10th Nat. Conf., 1963), Pergamon Press, 1963, pp. 356–371.

ISSN 1068-3755, Surface Engineering and Applied Electrochemistry, 2008, Vol. 44, No. 1, pp. 50–54. © Allerton Press, Inc., 2008.
Original Russian Text © S.A. Chulovskaya, V.I. Parfenyuk, 2008, published in Elektronnaya Obrabotka Materialov, 2008, No. 1, pp. 58–63.

ELECTRICAL PROCESSES
IN ENGINEERING AND CHEMISTRY

Influence of the Electrolytic Solution Composition on the Process of Electrochemical Synthesis of Nanodimensional Cupriferous Powders

S. A. Chulovskaya[a] and V. I. Parfenyuk[a, b]

[a] *Institute of Chemistry of Solutions, Russian Academy of Sciences, ul. Akademicheskaya 1, Ivanovo, 153045 Russia*
e-mail: vip@isc-ras.ru

[b] *Ivanovo State Chemicotechnological University, pr. Engel'sa 7, Ivanovo, 153000 Russia*

Received October 4, 2007

Abstract—The cathode reduction ability of nanodimensional cupriferous powders consisting of nanodimensional particles was shown. The smallest crystalline spongeous formations are deposits obtained at limiting current density. The organic cosolvent role in the process of electrochemical deposition of ultrafine metal-containing powders from water–isopropanol alcohol copper dichloride solutions was shown. Geometrical parameters of the obtained particles were determined by transmission electron microscopy.

DOI: 10.3103/S1068375508010109

INTRODUCTION

For the last ten years, nanomaterial science has been widely developed. Nanostructure compositions with dimensions of the constituent elements not exceeding ~100 nm at least in one direction possess essentially new functional characteristics differing from those of the respective condensed materials; they hold great possibilities for efficient development of many domains of chemistry, electronics, medicine, etc. Therefore, at present, the problem of obtaining of these particles with prespecified properties is relevant. Many existing technologies of obtaining of nanodimensional particles are labor-intensive and multistage [1–3]. An urgent problem is the synthesis of fine particles with a narrow size distribution, which is not always possible for a number of reasons. An alternative approach to the solution of this problem is the application of the simple and inexpensive method of electrochemical synthesis [4]. Practical realization of the process presupposes knowledge of the factors that influence the process of electrolysis and deposit formation and determine the physicochemical properties of the final product.

A material for obtaining of fine powders is a spongeous cathode deposit formed at limiting currents. The spectrum of the physicochemical properties of the powders may be varied over a wide range by changing the electrolyte composition, the electric modes, and other factors of the process. The possibility to obtain ultrafine particles with high thermodynamic stability is also an important problem. A high excess of energy on the particle surface favors adhesion of the particles and their integration into greater agglomerates. This process is hindered by introduction into the electrolyte of various stabilizers, their action being shown in the redistribution of the ratios of the rates of formation and growth of the new phase due to blocking of active centers and changing of the surface energies at interfaces.

Copper and its compounds are most often used for preparation of new generation materials. Introduction of fine cupriferous powders into lubricant compositions allows widening of the operation load interval and their application in various friction assemblies; bactericidal properties of cupriferous powders are used for preparation of medical materials of wide action spectrum; the ultradispersed state of the metal in the powder shows high catalytic activity in various oxidation–reduction reactions [5, 6].

The present work is concerned with revealing of conditions for electrodeposition of fine copper powders from copper dichloride solutions in mixed water–isopropanol solutions of various compositions, the determination of the cosolvent influence on the degree of dispersion of the cupriferous powders, and the study of the dimensional properties of the powder particles by the electron-microscopy method.

EXPERIMENTAL

The values of the currents required for realization of electrochemical synthesis of nanodimensional cupriferous powders were found from polarization curves (Fig. 1). For this purpose, using the potentiostat PI-50-1 complete with the programming device PR-8, in solutions of electrolytes of various compositions, polarization measurements were carried out. The potential variation rate was 5 mV/s. The working electrode for the polarization research was a copper disk (the active area $S_{el_2} = 8.55 \times 10^{-4}$ dm^2). The subsidiary electrode was a

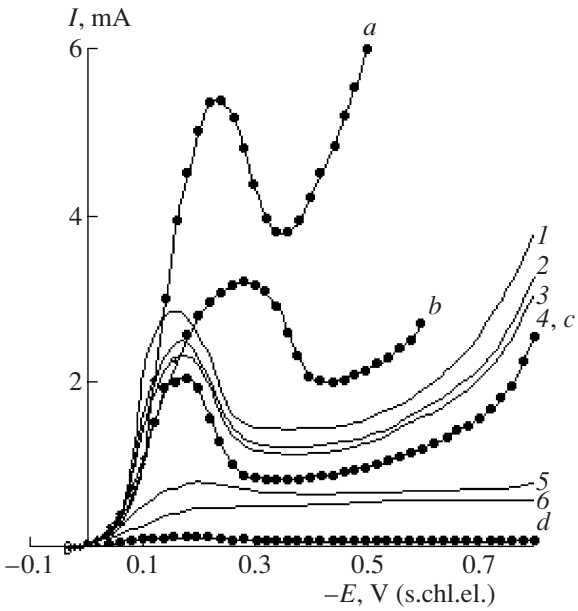

Fig. 1. Cathode polarization curves obtained from water–isopropanol solutions of copper dichloride. Lines with spherules: i-C_3H_7OH content—0.04 ppm; copper dichloride concentration (m): *a*—0.4; *b*—0.2; *c*—0.1; *d*—0.01. Continuous lines: copper dichloride concentration 0.1 m; i-C_3H_7OH content (ppm): *1*—0.00; *2*—0.01; *3*—0.03; *4*—0.04; *5*—0.08; *6*—0.12.

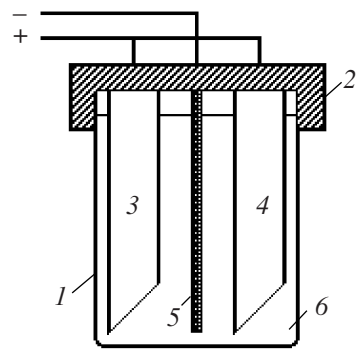

Fig. 2. Scheme of the experimental installation. *1*—electrochemical cell; *2*—vinyl chloride plastic cover; *3* and *4*—anodes; *5*—cathode; *6*—electrolyte solution

platinum electrode, and the reference electrode was a saturated silver chloride electrode. Taking into account the ratios of the areas of the electrodes applied for the polarization measurements and electrolysis, the current intensity value required for the electrosynthesis of cupriferous powders was calculated by the formula

$$i_n = \frac{i}{S_{el_2}} S_{el_1},$$

where i_n is the current intensity at which the powder electrolysis was carried out, i is the current intensity taken from the polarization curves, S_{el_1} is the active area of the steel cathode applied at the electrolysis, and S_{el_2} is the active area of the copper electrode applied at the polarization measurements.

The electrochemical synthesis of copper powders was carried out in a glass cell with a steel cathode (the active area S_{el_1} = 0.16 dm^2) and with titanium–ruthenium–oxide anodes (Fig. 2) at a constant electrode potential. A water–isopropanol solution of copper dichloride ($CuCl_2$) was used as the electrolyte.

Electric crystallization was carried out from nondiaerated solutions without forced mixing. The cathode deposit formed at the electric synthesis was a spongeous dendrite formation. At specified intervals, the cathode was shaken; the deposit spilled on the cell bottom. A small amount of hydrogen evolved during the concurrent process providing natural stirring of the solution in the circumcathode space volume and favored aeration of the growing deposit. The process termination criterion was hydrogen effervescence; therefore, the duration of the deposition for each experiment had its own value. The evolved hydrogen did not influence the quality and was not a component of the formed deposit composition. The electrolytic deposit appeared on the cathode in the form of a sponge at t = 25°C. After the electrolysis termination, the obtained deposit was separated from the electrode, thoroughly washed with distilled water up to a constant value of electric conductivity in the mother residue, and dried up to the powderlike state. Before each experiment, the glass part of the electrolyzer was washed with distilled water and then with the electrolyte solution. The anode surface was cleaned with fine abrasive paper, degreased, and washed. For the electrolyte preparation, there were used reagents of the "chemically pure" grade.

Information on the dimension and form of the micropowder particles was obtained by the method of transmission electron microscopy by virtue of an electron microscope (EMV-100 L) in the high resolution mode. For adequate construction of the histograms characterizing the disperse composition of the powders, electron micrographs were made on various microparts of the sample at various magnifications.

RESULTS AND DISCUSSION

Figure 1 shows results of the polarization research of the metal deposition. The polarization curves have a classical form characteristic of multistage processes proceeding with diffusion control. The rate of the ion transit to the electrode surface has a practically constant value, its maximum being determined by the stationary diffusion rate. In the conditions of the achieved limiting current intensity, there occur the appearance and initial development of crystalline nuclei of the spongeous deposit. Then, there takes place growth of the earlier formed crystalline nuclei, that is, formation of the

structure of the spongeous deposit particles being the most rational form of efficient use of the diffusion space. Under the passivation influence, the potential of the side faces of the growing crystal achieves a value sufficient for formation of new crystalline nuclei.

The dependences shown in Fig. 1 have "horizontal areas" where the current intensity value does not depend on the impressed voltage. These areas existing at certain potential values correspond to the limiting current values. Similar areas are observed on all the polarization curves, but they have different lengths along the axis of the abscissa depending on the electrolyte composition. In particular, they are minimal on curves *a* and *b*, and they are sufficiently pronounced on curves *5*, *6*, and *d*.

The presence of maxima on some polarization curves is explained below. The sharp increase of the cathode current on the last parts of the curves corresponds to the process of hydrogen ion reduction.

Realization of the powder synthesis at 0.4 m $CuCl_2$ and mixture composition H_2O—*i*-C_3H_7OH 0.04 ppm isopropanol (Fig. 1) is difficult, since the region of fine deposit appearance is small. As the copper dichloride concentration decreases from 0.4 to 0.1 m, there increases the region of potentials at which the rate of ion transit to the circumcathode area lags behind the rate of their discharge; this is one of the basic reasons of fine cupriferous deposit formation. The optimal concentration providing stable process of electric synthesis of nanodimensional particles of copper and its compounds is 0.1 m. At further decrease of the salt concentration, the electrochemical deposition realization is inexpedient for a number of reasons: the low rate of deposition, low product yield, and increase of dimensions of the particles constituting the composition of the obtained cathode deposits.

Admixtures of isopropanol (Fig. 1) decrease the values of the limiting currents; this contributes to realization of the process of metal-containing structure deposition at higher overvoltage and to formation of fine deposits.

In the process of spongeous cathode deposit formation, surface-active substances adsorbed on the cathode influence all the stages of formation and growth of the spongeous cathode deposit. Depending on the nature and concentration of the introduced admixtures, the effects of their action are different: some of them mainly influence the diffusion kinetics and others directly affect the cation discharge. In the region of the isopropanol concentration up to 0.12 ppm, on the polarization curves maxima are observed; they are due to cathode passivation connected with formation of intermediate products of low solubility: copper monochloride (CuCl) and oxide (Cu_2O) [7]. As the concentration of the organic component increases, the values of the limiting cathode currents decrease; this may be attributed to the increase of the water–alcohol electrolyte viscosity [8] and, as a consequence, to the decrease of the copper ion diffusion coefficients, as well as to the change of the charge transfer conditions.

There is another hypothesis explaining the decrease of the cathode current maxima up to their complete disappearance on the polarization curves with increasing of the organic cosolvent content in the water–organic mixture.

Earlier [9, 10], on the basis of measurements of compensating voltages of volt circuits in electrolyte solutions of various compositions, values of the changes of the surface potentials of organic and water–organic solvents [11, 12] at the liquid–gaseous phase interface were calculated. The obtained results allowed reaching the conclusion that, at a certain concentration of the nonaqueous component in a water–organic mixture (from 0.08 to 0.12 ppm for solvents of various classes), a complete blocking of the water solution boundary surface by molecules of organic solvents is observed. This fact may be explained by the following. The studied nonaqueous solvents (some aliphatic alcohols from methyl to n-butyl, acetone, methyl cyanide, dimethylsulfoxide, dimethylformamide, etc.) show surface–active properties with respect to water. Since molecules of nonaqueous solvents and water at the liquid–gaseous phase interface are oriented differently, this leads to the sign inversion of the surface potentials at transition from water to nonaqueous solvents: from +0.10 V (for water) to –0.275 V for isopropanol, 0.434 V for dimethylformamide, etc. In contrast to molecules of water, the ones of organic solvents are oriented with the dipole positive pole towards the gaseous phase; this explains the negative values of the surface potentials in comparison with water.

Something of the kind may be expected for the description of the electrode–solution boundary. At the isopropanol concentration ~0.12 ppm, the diffusion layer in the circumelectrode space almost completely consists of alcohol molecules. A scientific confirmation of this fact is Jakuszewski's work [13]; on the basis of the direct immersion method, he has shown that, for the water–ethyl hydroxide system, the metal electrode surface (diffusion layer of the circumelectrode space) is completely blocked by molecules of organic solvent.

A high content of *i*-C_3H_7OH in the electrolyte solution leads to reduction of the dielectric permeability; a decrease of the electric conductivity of the given part of the solution; and, as a consequence, to a decrease of the values of the limiting cathode currents with an increase of the isopropanol concentration in general and to a decrease of the cathode current maxima with their complete disappearance in particular (at the alcohol content higher than 0.12 ppm). At the isopropanol content ~0.04 ppm, the values of the limiting cathode currents contribute the most to obtaining of fine deposits.

Thus, the optimal electrolyte composition favoring obtaining of fine copper deposits is the following one: concentration of $CuCl_2$—0.1 mol/kg (m); *i*-C_3H_7OH—0.04 ppm.

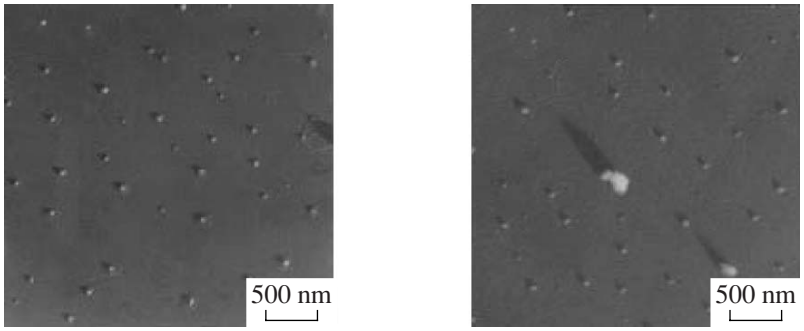

Fig. 3. Microphotographs of nanodimensional cupriferous powder.

Figure 3 presents microphotographs of nanodimensional cupriferous powder obtained by electrodeposition from a water–isopropanol solution of the following composition: 0.1 m $CuCl_2$; 0.04 ppm i-C_3H_7OH at 4 V and 0.25 A. One can see from the micrographs that the powder particles with dimensions ~100 nm have a spherical form; they are not aggregated. The powder contains a small amount of aggregates of nonspherical form appearing as the result of adhesion of lesser particles due to weak physical interactions. Data on the particle distribution by dimension are given in the form of a histogram in Fig. 4. The maximal quantity of the particles is located in the range of 40–80 nm.

The qualitative composition of the synthesized cupriferous powders is determined by the thermogravimetric, mass-spectrometric, and electron-diffraction methods of analysis [14]. The obtained product is multicomponent; it contains unoxidized copper, oxides of copper (I, II), and an insignificant amount of copper monochloride.

With the view of practical application of nanodimensional cupriferous powders, a complex of laboratory tests was carried out.

Application of the synthesized powders as admixtures to industrial lubricants gave positive results in increasing the antifriction and antiwear characteristics of the studied lubricating compositions.

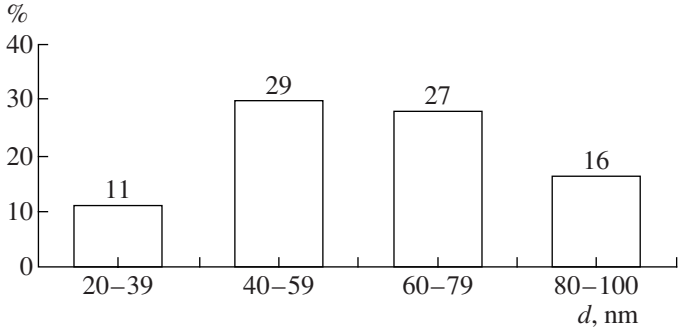

Fig. 4. Histograms of the distribution of nanodimensional cupriferous particles in powder.

The catalytic activity of the powder in the reaction of low-temperature conversion of carbon monoxide by water vapor was studied. Catalysts based on cupriferous powders were shown to be considerably superior to the industrial ones at the low-temperature stage. Modification of hydroxyethylcellulose was carried out by intercalation (the mechanochemical dispersion method) of nanodimensional cupriferous particles into the polymer matrix. Results of microbiological research showed that the modified hydroxyethylcellulose gained essentially new properties: the polymer composite showed antimicrobial (antibacterial) activity to many kinds of bacteria.

Detailed analysis of the results of the carried out research will be a subject of further publications.

CONCLUSIONS

The carried out research has shown the possibility to obtain nanodimensional cupriferous powders by the method of electrochemical cathode reduction from water–isopropanol solutions of electrolytes. It has been found that the process of electrochemical crystallization of cupriferous deposits from copper dichloride solutions in a water mixture with isopropanol is significantly influenced by the organic cosolvent. Admixtures of low-molecular surfactants into water solutions of electrolytes lead to a decrease of the limiting cathode current values and contribute to optimization of the dimensional characteristics of cupriferous powders.

REFERENCES

1. Pomogailo, A.D., Rozenberg, A.S., and Uflyand, I.E., *Nanochastitsy metallov v polimerakh* (Metal Nanoparticles in Polymers), Moscow, 2000.
2. Gubin A.P., Koksharov, Yu.A., Khomutov, G.B., and Yurkov, G.Yu., Magnetic Nanoparticles: Obtaining Methods, Structure, and Properties, *Usp. Khim.*, 2005, vol. 74, no. 6, pp. 539–569.
3. Shabanova, N.A., Popov, V.V., and Sarkisov, P.D., *Khimiya i tekhnologiya nanodispersnykh oksidov* (Chemistry and Technology of Nanodispersed Oxides), Moscow, 2006.

4. Murashova, I.B., Taushkanov, P.V., and Burkhanova, N.G., Change of Structure Characteristics of Spongeous Copper Deposit at Galvanostatic Electrolysis, *Elektrokhimiya*, 1999, vol. 35, no. 7, pp. 835–840.
5. Mel'nikov, V.G., Working Efficiency and Kinetic Regularities of Tribochemical Transformations of Lubricants in the Rolling Friction Zone, *Zashch. Met.*, 2005, vol. 41, no. 2, pp. 168–181.
6. Il'in, A.A. and Smirnov, R.R., Mechanical Activation Influence on Structure and Catalytic Properties of Copper Oxide, *Khim. Khim. Tekhnol.*, 2006, vol. 49, no. 5, pp. 42–45.
7. *Spravochnik khimika* (Handbook of Chemist), Leningrad, 1971, vol. 2.
8. Afanas'ev, V.N., Efremova, L.S., and Volkova, T.V., *Fiziko–khimicheskie svoistva binarnykh rastvoritelei. Vodosoderzhashchie sistemy* (Physicochemical Properties of Binary Solvents. Water–Containing Systems), Ivanovo, 1988, Part II.
9. Chankina, T.I. and Parfenyuk, V.I., Thermodynamic Characteristics of Resolvation of Sodium and Potassium Ions in Mixed Water–Dimethylsulfoxide Solvent, *Zh. Fiz. Khim.,* 2004, vol. 78, no. 9, pp. 1592–1595.
10. Chankina, T.I, Chulovskaya, S.A. and Parfenyuk, V.I., Thermodynamic Parameters of Resolvation of Chlorine and Sodium Ions in Water–n–Propyl Alcohol Mixtures at 298.15 K, *Zh. Fiz. Khim.,* 2004, vol. 78, no. 6, pp. 992–996.
11. Parfenyuk, V.I., *Voda: struktura, sostoyanie, sol'vatatsiya. Dostizheniya poslednikh let* (Water: Structure, State, and Solvation. Achievements of Last Years), Moscow: Nauka, 2003, p. 378.
12. Parfenyuk, V.I., Surface Potential at the Nonaqueous Solution–Gaseous Phase Interface, *Kolloidn. Zh.*, 2004, vol. 66, no. 4, pp. 1–5.
13. Jakuszewski, B., Partyka, S., and Przasnyski, M., Potencjaly ladunku zerowego rteci w mieszaninach etanolowo–wodnych, *Roczniki Chemii Ann. Soc. Chim. Polonorum.*, 1972, vol. 46, pp. 921–927.
14. Chulovskaya, S.A., Lilin, SA., Parfenyuk, V.I., and Girichev, G.V., Physicochemical Properties of Ultrafine Cupriferous Powders Obtained by the Cathode Reduction Method, *Zh. Fiz. Khim.,* 2006, vol. 80, no. 2, pp. 332–335.

ISSN 1068-3755, Surface Engineering and Applied Electrochemistry, 2008, Vol. 44, No. 1, pp. 55–59. © Allerton Press, Inc., 2008.
Original Russian Text © V.G. Ciobanu, 2008, published in Elektronnaya Obrabotka Materialov, 2008, No. 1, pp. 64–69.

ELECTRICAL TREATMENT
OF BIOLOGICAL OBJECTS AND FOODSTUFFS

Foundations of Energetics of Electroplasmolysis of Vegetable Raw Materials

V. G. Ciobanu

Institute of Applied Physics, Academy of Sciences of Moldova, ul. Akademiei 5, Chisinau, MD-2028 Moldova
e-mail: lpepv@phys.asm.md

Received February 5, 2007

Abstract—Energetics of low-voltage pulsed electroplasmolysis of vegetable raw materials was theoretically and experimentally substantiated for various ways of connection of the working chamber to the power source. The main electrical and technical requirements for designing and realization of the process of electroplasmolysis of cell tissues in various areas of application ensuring electrical safety during work, optimal modes of working, and efficiency are outlined.

DOI: 10.3103/S1068375508010110

INTRODUCTION

Various technological processes are known in which an electric field is applied for the contact effect on raw materials of vegetable and animal origin [1–4] and suppression of vital functions of microflora of food media [5, 6] and microorganisms or pathogenic flora [7, 8].

This effect is based on the processes of the direct effect of the electric field on the living tissue, which causes structural variations at the cellular and subcellular levels [9, 10] and the subsequent increase in cell penetrability. One of such processes is electroplasmolysis of vegetable raw materials [11, 12, 13], which is of specific scientific interest and wide spread in the food industry [3, 14–16, 17].

However, for a more reliable and substantiated introduction to production of this perfect instrument that varies the structure of the cell tissue, there are no sufficient data and recommendations for the energetics and technological character in the literature, especially since the voltage applied for the electrical treatment of the plant tissue is different in the value and form. Depending on the strength of the electric field generated by the supply unit at which the raw materials are treated, electroplasmolysis should be subdivided into **high-voltage** ($E \geq 1000$ V/cm) and **low-voltage** ($E \leq 1000$ V/cm).

The effective value of the field strength in the vegetable mass during the contact treatment equals

$$E_{ef} = E/\varepsilon,$$

where ε is the permittivity of the raw material.

The quantity E_{ef} is the potential gradient between the electrodes, and, in practice, it is purposeful to divide it into three steps:

low gradient (lower than 500 V/cm);

moderate gradient (500–1000 V/cm);

high gradient (higher than 1000 V/cm).

Electroplasmolysis of raw materials is associated with a functional dependence with the ratio of the main physical quantities characterizing the process being

$$A = \sigma_{av} E^2 \tau_p,$$

where A is the specific work necessary for the electroplasmolysis, J/m^3; E is the strength of the applied electric field, V/m; σ is the average electrical conductivity of the raw material, S/m; and τ is the treatment time, s.

ANALYSIS OF CONNECTION CIRCUITS OF ELECTRODES TO ELECTRIC NETWORKS

Notice [7, 18] certain variants of possible connection circuits of systems of electrodes for the contact effect on the raw material:

(i) In the case of triangle connection of electrodes, the plasmolysis current flows between the phase electrodes (I_p is the load current). However, in addition to this current, the leakage current I_u will flow from the outer electrodes to the neutral grounding electrode of the power transformer. This current determines the energy losses.

(ii) If the electrodes are star-connected with the alternation of the phase and null electrodes connected to the grounded neutral point of the transformer, then such a circuit, from the viewpoint of safety, is most acceptable since the load is more symmetric in this case. However, the electroplasmolysis time τ_p increases on average by a factor of three, and, consequently, the productivity of the apparatus decreases to the same degree.

(iii) In the case of triangle connection of the main electrodes, if the additional outer electrodes are connected with the grounded neutral point of the trans-

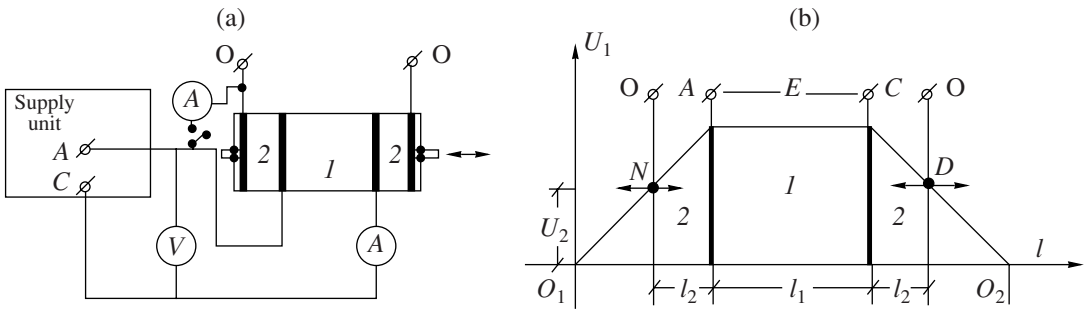

Fig. 1. (a) Layout of the experimental stand with the use of supply units (LUP-1, BP-125A) and the electroplasmolysis cell, and (b) zones of the unit cell with different voltage drops between the electrodes. (*1*) Plasmolysis zone of the interelectrode space l_1 (phases *A* and *C*); (*2*) plasmolysis zones behind the electrode space l_2 of the phase *A* and *O*, phase *C* and *O*.

former, these electrodes become screening from the viewpoint of electric safety. However, because of the phase asymmetry, the process intensity at the outer interelectrode gaps decreases more than at the other gaps (main). This phenomenon can be eliminated by varying the distance between the screening and main electrodes and decreasing it by a factor of $\sqrt{3}$.

POWER ESTIMATION OF THE PROCESS

For the quantitative estimation of the power consumption in the main interelectrode gap and its leakage during electroplasmolysis, we measured the power consumption W_0 on an experimental stand and under production conditions.

We used a compact LUP-1 setup [19] possessing a wide range of possibilities for controlling the electrical and time parameters during the treatment of various types of raw materials. It consists of the supply unit, the cell for displacement of the treated object, and the remote control panel.

The supply unit allows one to select a wide spectrum of various modes by the duration of the treatment and pause, by the number of treatment pulses and pulse polarity, and by registration of the used electrical power.

The cell comprises rectangular vessels made from plexiglass, inside which it is possible to arrange electrodes differing by the shape and amount. Electrodes (phase and null) are easily connected to each other by various circuits as well as to the supply unit and allow one to control the interelectrode gap (Fig. 1).

Under the production conditions, the current source involved a BP-125A supply unit [2] and a flow cylindrical experimental chamber equipped with electrodes (Fig. 2). The supply unit was connected to a three-phase network with a neutral main, which allowed us to control and select the optimal treatment modes of a milled raw material and to control the electrical parameters for registration of the power consumption. The main electrodes of the chamber had outputs connected to the supply unit by various electric circuits, while screening electrodes were mounted at the input and the output of the flow of the raw material.

The working chamber of the plasmolysis was connected to a flow processing line using rubber hoses between the pump of the raw material and the facility for separation of the juice (Fig. 2b).

We investigated the variants of the connection of the electrodes by circuits: (a) phase–null; (b) phase–null–phase; (c) null–phase–null; (d) the star and triangle connection with screening electrodes and without them.

The consumed power W_0 was measured directly or determined by the formula

$$W_0 = \left(\frac{U_{AB}}{\sqrt{3}}I_A + \frac{U_{BC}}{\sqrt{3}}I_B + \frac{U_{CA}}{\sqrt{3}}I_C\right) \times 10^{-3} \text{ kV A},$$

where U_{AB}, U_{BC}, and U_{CA} are the phase-to-phase voltages, V; and I_A, I_B, and I_C are the currents of the corresponding phases, A.

The power consumptions were determined by the ratio to the power consumed for the optimal performance of the electroplasmolysis and are constant. For a concrete type of raw material and identical conditions of carrying out the plasmolysis process, W_p = const [2, 20, 21].

Under identical conditions of carrying out the plasmolysis of one type of raw material with constant electrical and structural–technological parameters in circuits (a) and (b), the value of W_p is larger than the power consumption by the circuit (c) by a factor of 1.5–2.6. In the circuit (c), the outer electrodes are connected to the neutral point, and no leakage current is observed due to their screening functions.

The actual power consumption in circuits (c) and (d) exceeds W_p by 5–10% if the neutral point is connected to rounded outer electrodes, near whose edges the electric field is distorted. This phenomenon is eliminated via the use of parallel-sided electrodes, and the total power consumption is approximately equal to W_p if we neglect the losses for heating in contacts and connecting cables ($W_0 = W_p$).

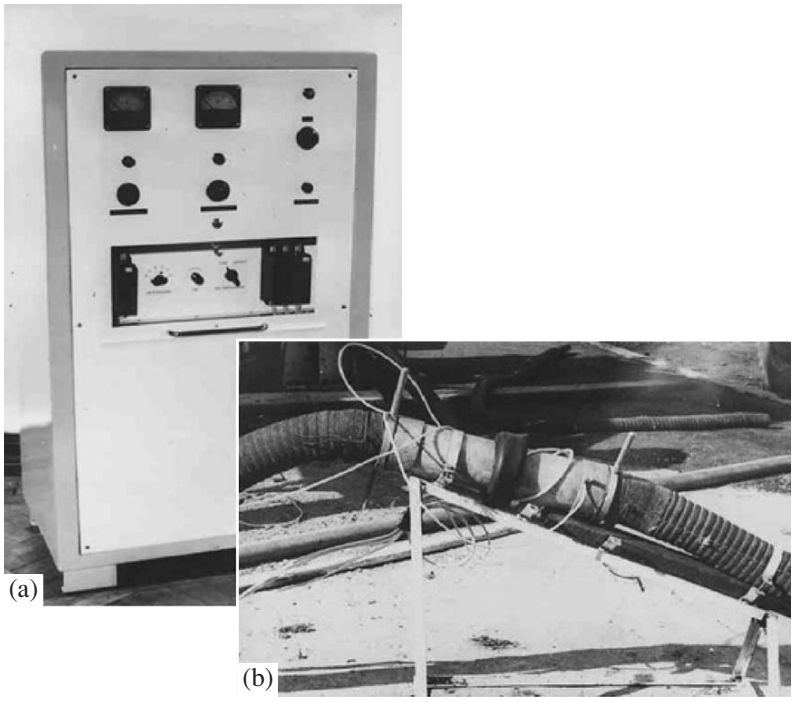

Fig. 2. (a) Supply unit BP-125A and (b) working chamber for electroplasmolysis of raw materials.

The over expenditure of electric power compared with W_p is larger by a factor of 1.5–2.6 in circuits (a) and (b), where the phase is connected to the outer electrodes, and is caused by current leakage through the raw material to the neutral point of the transformer.

If leakage from one electrode proceeds to the gap connected between the phase and the neutral point, the losses reach 90% of the consumption in the interelectrode spacing.

If electrodes are star-connected by the circuit C-0-B-0-A-0-C, leakage from two outer electrodes at six gaps connected between the phase and the neutral point, or one electrode per three gaps, which is the same, will cause losses less than in the previous case by a factor of three, which will constitute 30%.

For the triangle connection of electrodes (first circuit), the absolute losses for leakage from the outer electrodes will remain the same as for the star connection with the phase supply to the outer electrodes. Since the power in the interelectrode gap is higher by a factor of three, the losses for leakage will decrease to the same extent compared with the losses in the variant where the electrodes are star-connected (the outer electrodes are connected to the phase) and will be 10% of the consumption in the interelectrode gap.

Moving electrodes consume 4–6% less power than stationary ones. These losses are reduced to zero if reliable electrical contact is provided between the particles of the raw material as well as between the electrode and the raw material. If it is impossible to perform this measure technically, then the treatment time is correspondingly increased in order to provide complete plasmolysis of all the cells of the raw material.

As the null electrodes are moved apart from the phase electrodes (*A* and *C*) by the sides in the direction to points O_1 and O_2, the plasmolysis zones are formed behind the electrode spacing *2* (Fig. 1b). These zones can be extended depending on the value of the applied voltage, treatment time, and type of the raw material. As the interelectrode spacing l_1 and l_2 increases, the value of the field strength in this zone drops and tends to zero. In Fig. 1, this value corresponds to the location of points *N* and *D* and equals U_2, which constitutes a part of the value of the applied voltage between the electrodes U_1.

It follows from the pattern of the field distribution that the zones of plasmolysis (main interelectrode spacing *1* and behind the electrode spacing *2*) (Fig. 1) can also be extended due to an increase in the number of electrodes in the working chamber [22, 23].

The experiments on determination of the distribution of the field strength between the electrodes for various connection circuits allow us to substantiate the apparatus design and select processing parameters of electroplasmolysis of the vegetable raw materials and its safe realization.

Therefore, possibilities appear to solve the problems of development and designing of various electrode chambers for apparatuses, and, in some cases, investigations can be performed with the use of comparatively simple models of electrode cells.

ELECTRICAL AND TECHNICAL REQUIREMENTS FOR THE PROCESS REALIZATION

The circumstance should be also noted that the star connection of the load is used only at identical loads of all three phases [24]. It is known from practice that not in all designs of electroplasmolysis apparatuses are the conditions of the uniform load of the phases fulfilled; therefore, the voltages over the resistances of the beams of the load star turn out different. In addition, connection or disconnection of one phase of the load is inadmissible for this circuit.

In this respect, the triangle connection of the load is advantageous. Phase resistances can be different, and, in exclusive cases, they can be connected and disconnected irrespective of one another (**traditional construction of the apparatus**).

The same possibility is present in the case of star connection of generator windings and the load if their neutral points are connected directly or through the ground (**sea modification of the apparatus**).

To provide safety during implementation of the process, the working electrodes of the apparatus are enclosed into electrically isolated cases, and additional screening electrodes are mounted at the input and output of the flow of the raw material. These electrodes are connected to the grounded neutral point of the transformer. Thereby the plasmolysis zone is completely confined in the closed chamber ($I_u = 0$) [2, 25].

The working chamber of the apparatus for electroplasmolysis should contain a terminal box connected to the case, which allows one to group and connect the outputs of the electrodes by one or another electric circuit. On the opposite sides of the case, along the flow of the raw material, branch pipes of flanges are installed for easy and convenient connection of the apparatus to the flow of the raw material of production lines differing by productivity and destination [2, 15]. In the case of the absence of additional screening electrodes, branch pipes or flanges of the apparatus are grounded.

If the electrodes are combined into packets [26], the number of packets of the working chamber is proportional to the number of phases of the supply source, while the number of electrodes in the packet is determined by the formula

$$N = k\frac{D}{l}\sin\left(\frac{\pi}{n} - \frac{l}{D}\right),$$

where N is the number of electrodes in the packet; n is the number of packets (3, 6, 9, etc.); D is the inner diameter of the apparatus body, mm; l is the distance between the electrodes in the packet, mm; $\pi = 3.141$; and $k = 0.6–1.4$.

The distance between the electrodes in the packet is equal to the distance between the packets and strip electrodes and is determined by the formula

$$l = (0.06 - 0.3)U,$$

where U is the voltage between the electrodes, V.

CONCLUSIONS

It follows from the aforesaid that the energetics and exploitation characteristics of electroplasmolysis of the cell tissue of raw materials largely depend on the type of electrical mains to which the apparatus is connected, on the electric field strength, and on the connection circuit of the electrodes of the working chamber.

The performed analysis of the power consumption and technical analysis should be taken into account in investigation and modeling of electrode chambers as well as in designing and development of installations for electric treatment of vegetable raw materials of various destinations. With the proviso of fulfillment of the technical requirements, it is possible to provide safe operation of the installation and its exploitation in the optimum mode of power consumption and high efficiency in private life; at tinned food factories and wine plants; and on aircraft, seacraft, and spaceships.

REFERENCES

1. Bologa, M.K., Electrical and Chemical Investigations and Technologies at the Institute of Applied Physics of Academy of Sciences of Moldova, *Elektron. Obrab. Mater.,* 2004, no. 2, pp. 4–13.
2. Ciobanu, V.G., An Increase in Efficiency of the Treatment of Vegetable Raw Materials by Electroplasmolysis, *Cand. Sci. Dissertation*, Kiev, 1988.
3. Ciobanu, V., Tehnologii De Utilizare Rațională a Fructelor în Medium Rural, *Conferența Națională "Comunitățile rurale și Renașterea Satului,"* Chișinău, 2005, pp. 121–122.
4. Rogov, I.A., *Elektrofizicheskie metody obrabotki pishchevykh produktov* (Electrical Methods of Treatment of Food Products), Moscow: VO Agropromizdat, 1988.
5. Gulyi, I.S., Ukrainets, A.I., Debelinskii, S.N., Botoshan, N.I., Ciobanu, V.G., Kovbasa, V.N., and Berzoi, S.E., Effect of High-Voltage Electric Field on the Physicochemical Properties of Bear, *Elektron. Obrab. Mater.*, 1991, no. 4, pp. 50–55.
6. Nanii, E.P., *Elektropasterizatsiya* (Electropasteurization), Chisinau: Kartya Moldovenyaske, 1979.
7. Akopyan, R.A. and Mikaelyan, E.G., Effect of the Connection Circuit of Electrodes on Disinfection of the Soil, *Trudy Ar. NII MESKh*, 1975, no. 4, pp. 14–16.
8. Yarovoi, P.I., Chebanu, V.G., Stanku, M.L., et al., *Disinfection of Sewage by the Alternate Electric Current*, *Elektron. Obrab. Mater.*, 1985, no. 6, pp. 76–78.
9. Ciobanu, V.G., Ultrastructural Analysis of the Cell during Electroplasmolysis, Trudy *4-i respublikanskoi konferentsii po elektronnoi mikroskopii "Elektronnaya mikroskopiya i sovremennaya tekhnologiya"* (Proc. 4th

Republican Conf. on Electron Microscopy "Electron Microscopy and Modern Technology," Chisinau, 1990, pp. 125–126.

10. Ciobanu, V., Studiul Structurii Ţesutului Suculent Vegetal Tratat Prin Electroplasmoliză, in *Lucrările Conferinţei Naţionale cu Participare Internaţională "Cercetarea Ştiinţifică în Condiţiile Integrării Europene,"* Brăila, 2004.
11. Rudkovskaya, G.V., Botoshan, N.I., Ciobanu, V.G., Berzoi, S.E., and Poplavskii, P.P., USSR Inventor's Certificate no. 1 524 214, Moscow: PPP Patent, 1988.
12. Papcenco, A., Botoşanu, N., Berzoi, S., and Ciobanu, V., Fenomenul Histerezei în Mediul Biologic la Prelucrarea Termică Sau Electrică, *Lucrările Conferinţei Naţionale de Termotehnică, Ediţia a-7*, Braşov, 1997, vol. 3, pp. 309–317.
13. Lazarenko, B.R., Fursov, S.P., Shcheglov, Yu.A., Bordiyan, V.V., and Ciobanu, V.G., *Elektroplazmoliz* (Electroplasmolysis), Chisinau: Kartya Moldovenyaske, 1977.
14. Ciobanu, Vasile, Intensificarea Procesului De Deshidratare a Masei Verzi Fărâmiţate a Plantelor Prin Electroplasmoliză, *Comunicări Ştinţifice, Bucureşti: Ediţia Tehnică*, 1993, vol. 1, pp. 45–50.
15. Bordiyan, V.V., Intensification of Drying of Vegetable Raw Materials by Electroplasmolysis*, Cand. Sci. Dissertation*, Moscow, 1991.
16. Botoşanu, N., Berzoi, S., and Ciobanu, V., Electrodifuzia *şi Transferul de Masă Sau Căldură în Medii Biologice, Lucrările Conferinţei Naţionale de Termotehnică, Ediţia a-7*, Braşov, 1997, vol. 3, pp. 251–257.
17. Kupchik, L.A., Kartel', N.T., and Kupchik, M.P., Electrochemical Method of Obtainment of Oxidized Cellulose Sorbents, *Elektron. Obrab. Mater.*, 2003, no. 6, pp. 70–73.
18. Ciobanu, V., Unele Aspecte Energetice de Efectuare a Procesului de Electroplasmoliză, *Lucrările Conferinţei Naţionale de Termotehnica*, Reşiţa, 2003, pp. 279–280.
19. Chiebanu, V.G., Berzoi, S.E., Rozental', Ya.Sh., Govberg, M.G., and Simon, M.V., Laboratory Setup LUP-1 for the Investigation of the Electroplasmolysis Process, *Elektron. Obrab. Mater.*, 1990, no. 2, pp. 81–82.
20. Bologa, M., Ciobanu, V.G., Berzoi, S.E., and Botoshan, N.I., Optimization of the Electroplasmolysis Process of Apple Fiber, *Elektron. Obrab. Mater.*, 1988, no. 140, pp. 70–72.
21. Ciobanu, V.G., Berzoi, S.E., and Botoshan, N.I., Effect of Free Liquid Phase of Raw Materials on Efficiency of Electroplasmolysis, *Trudy 4-i Vsesoyuznoi nauchnoi tekhnicheskoi konferentsii "Elektrofizicheskie metody obrabotki pishchevykh produktov i sel'skokhozyaistvennogo syr'ya"* (Proc. 4th All-Union Sci. Tech. Conf. "Electrical Methods of Treatment of Food Products and Agricultural Raw Materials), Moscow, 1989, pp. 210–211.
22. Shcheglov, Yu.A. and Bogdan, K.N., Zonal Plasmolysis of Plant Tissue, *Elektron. Obrab. Mater.*, 1968, no. 5, pp. 92–93.
23. Shcheglov, Yu.A. and Chiebanu, V.G., USSR Inventors Certificate no. 446 266, Moscow: TsNIIP, 1975.
24. Atabekov, G.I., *Teoreticheskie osnovy elektrotekhniki* (Theoretical Foundations of Electrotechnique), vol. 1, Moscow: GEI, 1988.
25. Ciobanu, V.G., Shcheglov, Yu.A., Koval', N.P., and Ryabov, V.P., USSR Inventor's Certificate no. 1 045 445, Moscow: PPP Patent, 1983.
26. Shcheglov, Yu.A., Koval', N.P., Bobrakov, B.P., Ryabinskii, F.B., Furer, L.A., and Chiebanu, V.G., USSR Inventor's Certificate no. 747 462, *Byull. Izobret.*, 1985, no. 26.

ISSN 1068-3755, Surface Engineering and Applied Electrochemistry, 2008, Vol. 44, No. 1, pp. 60–63. © Allerton Press, Inc., 2008.
Original Russian Text © V.I. Netsvetov, K.L. Metlov, V.A. Khokhlov, Yu.V. Medvedev, V.N. Varyukhin, 2008, published in Elektronnaya Obrabotka Materialov, 2008, No. 1, pp. 70–74.

EQUIPMENT AND DEVICES

Experience of the Use of a Magnetosensitive Sensor in a Rolling Mill

V. I. Netsvetov, K. L. Metlov, V. A. Khokhlov, Yu. V. Medvedev, and V. N. Varyukhin

Donetsk Physicotechnical Institute, National Academy of Sciences of Ukraine, ul. Rozy Lyuksemburg 72, Donetsk, 83114 Ukraine

e-mail: ayup@levch.fti.ac.donetsk.ua

Received November 15, 2007

Abstract—A device allowing one to measure the speed of rotation of rollers in a rolling mill using magnetic markers is proposed. The device involves an accessory that marks the rollers magnetically and a magnetic field sensor (Hall probe). Simulation provided the determination of the minimal number of markers, their geometry, and their arrangement for obtaining a sinusoidal signal from the sensor. The device was successfully tested in production conditions.

DOI: 10.3103/S1068375508010122

During operation of section and wire mills, especially at rolling speeds reaching 100 m/s, because of the complex conditions of their exploitation, breakages can appear that not only lead to defects but also, in the case of "drill-in" (sticking) of the rolled metal, lead to breakage of mill units and its prolonged stoppage. One of the possibilities to avoid emergency conditions is continuous control over the kinematic parameters of the mill [1].

The most important of these parameters is the speed of rotation of guide rollers V. The deviation of this speed from the nameplate value V_n can serve as a warning of an approaching break. In principle, by the character of the deviations of V from V_n, we can judge the causes of the appearing danger.

The operation conditions of the mills (high temperature, water cooling, the presence of finely dispersed abrasive, magnetic pickups, etc.) abruptly limit the selection of reliable sensors for monitoring of the speed of rotation of guide rollers. Additional limitations appear because of the confinement of the space in which the sensors can be arranged. In addition, the operating mode of the mills is such that, in the case of sensor breaking, rapid exchange of the sensor should be provisioned. The existing foreign means of control of the kinematic properties of mills are too high-cost; therefore, the necessity appears to find a lower-cost method of monitoring.

For the first time within the Commonwealth of Independent States, attempts to develop an accessory for monitoring the speed of rotation of guide rollers were made at a Belarussian metallurgical plant [2]. A magnetic marker was applied on a roller in one punched place. Under the repeated magnetization, it was not always possible to superpose the center of a constant magnet with the center mark. As a result, the signal from the marker was blurred, and indefiniteness appeared during reading of the signal due to the presence of additional peaks. The operation of demagnetization of the previous topology was not carried out. In addition, a coil in which an emf was induced during passing the magnetic marker near the coil was used as a sensor. Such a system abruptly limits its application in low-speed stands since the value of the emf is proportional to the variation in the magnetic flux. In addition, the use of an inductive sensor under the condition of an intense electromagnetic disturbance abruptly reduces the signal/noise ratio.

The most appropriate sensor, which allows one to go beyond these limitations, is a Hall sensor. However, for its use, it is necessary that

(i) the roller material has residual magnetization (during application of the magnetic marker on the roller) sufficient for its detection by the sensor,

(ii) the sensor sensitivity provides detection of the signal from the magnetic marker at a distance 5–10 mm,

(iii) the sensor comprises a sealed accessory with the size providing its arrangement in immediate proximity of the roller, and

(iv) the sensor accessory should be packed into a case attached to the mill protecting it from harmful effects.

Electronic facilities are much more convenient for processing the sinusoidal signal. This provides the detection of not only its frequency but also of its phase shift, i.e., finally, the detection of the speed of rotation of the roller with a higher accuracy. It is shown below (see Appendix) that, in order to obtain such a sinusoidal signal from the sensor, it is necessary to apply not one marker on the roller but a certain even amount (S-N) of magnetic markers. The results of our theoretical calcu-

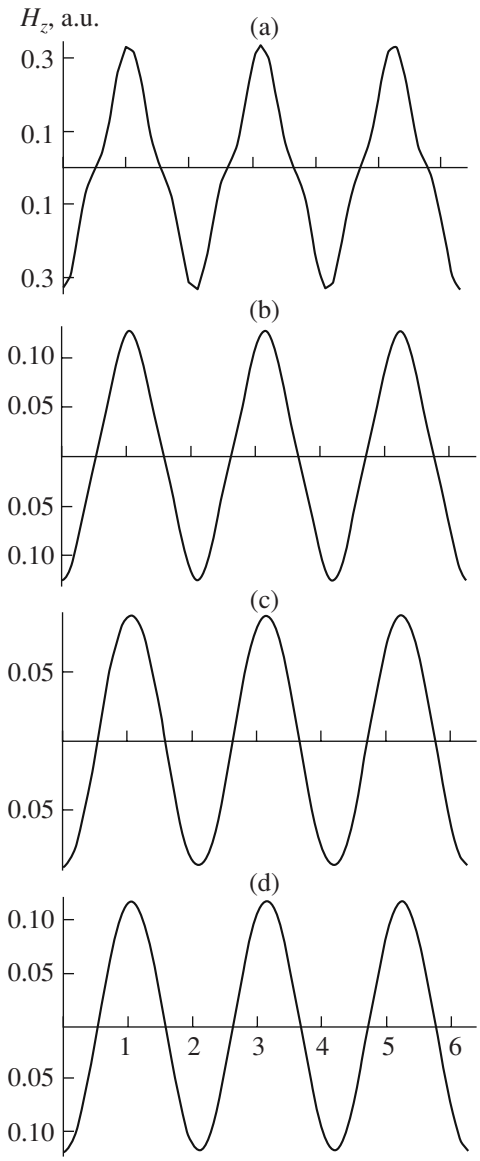

Fig. 1. Calculation of the system of arrangement of magnets over the circle of rolling cylinders. (a) $b/d = 1$, $r_m = 26/7$, $h = 5/7$; (b) $b/d = 1$, $r_m = 26/7$, $h = 10/7$; (c) $b/d = 0.5$, $r_m = 20/7$, $h = 10/7$; and (d) $b/d = 2$, $r_m = 0/7$, $h = 10/7$.

lations of the profile of a system of magnets arranged over a circle of radius r_m at a distance b from one another are presented in Fig. 1. The optimal residual magnetization of the roller marker (taking into account the sinusoidal character of the field distribution) is obtained with the use of cylindrical magnets with a base radius R and height l, which are arranged over the circle at a distance b approximately equal to $2R$. It is also evident from Fig. 1 that as b decreases the field amplitude decreases.

To determine the optimal parameters of the magnets and the minimum amount of necessary markers and the geometry of their arrangement, we analyzed theoretical calculations. The analysis showed that, for rollers about

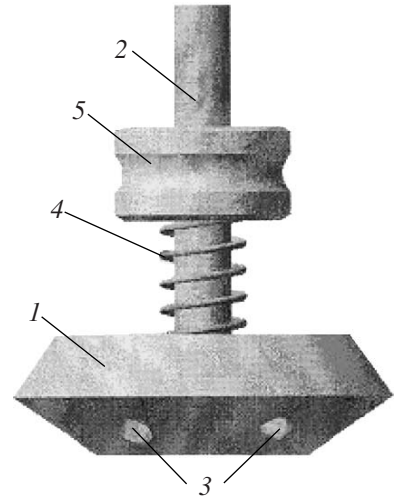

Fig. 2. Accessory for magnetization of the rollers. (*1*) Holder, (*2*) rod, (*3*) constant magnets, (*4*) spring, and (*5*) roller.

52 mm in diameter, which are used in the mill (see table), the optimal arrangement of the magnetization accessory of the magnets with $R = 7$ mm and a height of 10 mm, which were at our disposal, will be a distance of 14 mm between them.

In the experiment, magnetic markers were applied on the roller by touching the surface of cylindrical constant magnets. The markers were applied on the roller at its outer side using the accessory shown in Fig. 2. The method of magnetization assumes the mirror magnetization of the roller with respect to the magnets arranged in the accessory (Fig. 2) taking into account the ratio between the magnetic field on the surface of the magnets and the coercive force of the roller material. Since nearby arranged magnets decrease the residual field due to the demagnetization fields, we carried out the experiment on investigation of the distribution of the magnetic field of the roller as a function of the ratio $b/2R$ and compared the experimental results with the calculated data. The experimental results are presented in Fig. 3, from which it is evident that, at the ratio $b/2R = 1$ and $b/2R = 0.05$, the signal from the sensor is sinusoidal, although the value of the signal from the sensor decreases more considerably than is predicted by the theory as the distance between the magnets decreases.

Table

Stand no., roller d	V_n, m/s	V_m, m/s	Deviations, %
No. 19, $d = 49.6$ mm	11.86	12.15	+5.4
No. 21, $d = 47.6$ mm	17.99	17.20	–4.6
No. 23, $d = 50.4$ mm	28.67	29.45	+2.7
No. 25, $d = 51.2$ mm	45.30	44.15	–2.6
No. 27, $d = 51.5$ mm	70.31	70.38	–0.01

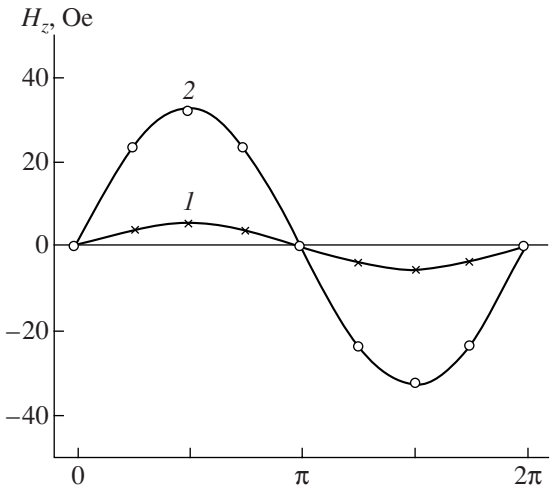

Fig. 3. Experimental angular dependences of the field H_z at various ratios b/D. (*1*) $b/D = 0.05$; (*2*) $b/D = 1.0$.

Prior to application of the magnetic markers, we studied the magnetic properties of the roller material (steel CT95X18). We investigated the residual field H_{res} of the material after its magnetization in a field of 2000 Oe, the penetration depth h of the field into the material, the temperature dependence of these parameters, and the degree of their aging under the mill operation conditions. We obtained the following results: $H_{res} = 90$ Oe, $h = 5$ mm. The values of the above-mentioned quantities in the range of the mill working temperatures (35–85°C) varied by no more than 10%. Therefore, the roller material is quite suitable for application of magnetic markers. The obtained data also allowed us to develop the method of repeated application of magnetic markers, including removing the traces of previous application in the case of redressing of the roller.

Experiments on the use of the suggested procedure were carried out at finish stands of the 150 mill at the Makeevka metallurgical plant (Ukraine). In the table, we present the nameplate data of the rolling speed V_n for several stands and their speeds determined by us.

It is evident from the table that the deviations of the measured values of the rolling speed virtually correspond to the admissible deviations (±5%) of their nameplate values. However, the roll at the 19th stand already requires replacement.

APPENDIX

In order to calculate the profile of the field of the system of magnets arranged over the circle, let us calculate the field of one cylindrical magnet with a base radius R and height $2L_z$. Under the assumption of uniform magnetization, let us represent the field as the superposition of the fields of two oppositely charged discs (the charge density is constant and equals M_S).

Let us write a scalar potential of the magnetic field that is induced by the charged disc of radius R arranged in the plane $z = z_1$ at the point with polar coordinates ρ, φ, and z in the SI system as

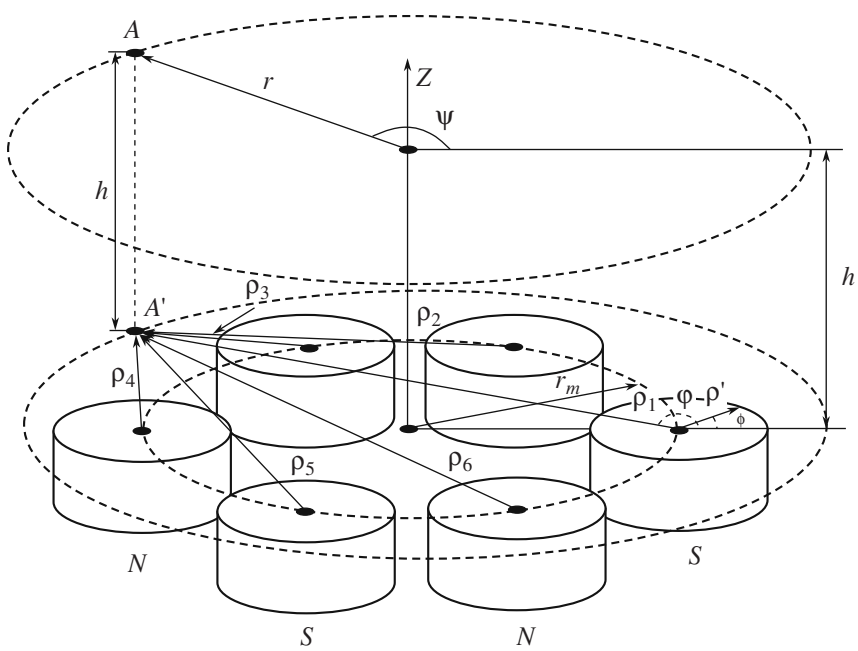

Fig. 4. Schematic diagram of the arrangement of magnets over the circle of radius r for which the field is calculated. Radius-vectors and angles used in the formulas of the Appendix are given ibidem.

$$\Phi(\rho, \varphi, z) = \frac{\mu_0 M_S R}{4\pi} \times \int_0^{2\pi}\int_0^1 \frac{\rho'}{\sqrt{(z-z_l)^2 + \rho^2 + \rho'^2 - 2\rho\rho'\cos(\phi-\varphi)}} d\rho' d\phi. \quad (1)$$

Henceforth, all the spatial coordinates are normalized to R, and M_S is the uniform magnetization of the magnet.

Using the Lipshits integral, let us write expression (1) as

$$\Phi = \frac{\mu_0 M_S R}{4\pi}\int_0^\infty \exp\left(-k|z-z_l| \times \left(\int_0^{2\pi}\int_0^1 J_0(k\sqrt{\rho^2+\rho'^2-2\rho\rho'\cos(\phi-\varphi)})\rho' d\rho' d\phi\right)dk, \quad (2)$$

where J_0 is the usual Bessel function.

Then, applying the addition formula for the Bessel functions, we obtain the following expression for the total potential of two oppositely charged discs (with $z_1 = 0$ and $z_1 = -2l_z = -2L_z/R$) at $z > 0$:

$$\Phi(\rho, z) = \frac{\mu_0 M_S R}{2}\int_0^\infty \frac{e^{-zk}(1-e^{-2kl_z})J_0(k\rho)J_1(k)}{k} dk. \quad (3)$$

Since $H = \text{grad}\Phi$, then

$$H_z(\rho, z) = \frac{\mu_0 M_S R}{2}\int_0^\infty e^{-zk}(1-e^{-2kl_z})J_0(k\rho)J_1(k)dk. \quad (4)$$

It is convenient to calculate this integral numerically since it converges well away from the magnet surface. As for the near-surface conditions, not only numerical problems appear but also the role of inhomogeneities of the magnetization of the constant magnet increases physically (the noncollinearity of its distribution, the domain structure) [1]. Therefore, we will obtain correct results at the distances h equal to or larger than R from the magnet surface.

Let us now start the calculation of the field above the system of magnets arranged uniformly over the circle of radius r_m. At each point of space (for example, on the circle of radius r, which is parametrized by a polar angle ψ and arranged at a height h from the plane of magnets), it is necessary to calculate the contribution of all the magnets. If we take six magnets (see Fig. 4) and their polarity varies periodically, then

$$\begin{aligned} H_z(\psi) &= H_z[\sqrt{r^2 + r_m^2 - 2rr_m\cos\psi}, h] \\ &- H_z[\sqrt{r^2 + r_m^2 - rr_m\cos\psi + \sqrt{3}\sin\psi}, h] \\ &+ H_z[\sqrt{r^2 + r_m^2 + rr_m\cos\psi - \sqrt{3}\sin\psi}, h] \\ &- H_z[\sqrt{r^2 + r_m^2 + 2rr_m\cos\psi}, h] \\ &+ H_z[\sqrt{r^2 + r_m^2 + 2rr_m\cos\psi + \sqrt{3}\sin\psi}, h] \\ &- H_z[\sqrt{r^2 + r_m^2 - rr_m(\cos\psi - \sqrt{3}\sin\psi)}, h]. \end{aligned} \quad (5)$$

The results of numerical calculation of the field profile above six magnets with $R = 7$ that are arranged over a circle of radius 26 (the distance b between the magnets equals $2R$ in this case) are presented in Fig. 1. Figure 1a shows the field profile (in relative units) at a distance $h = 5/7$ ($h < R$) from the plane of magnets, and Fig. 1b—at a distance 10/7 ($h > R$). It is evident that, in the first case, the field profile is periodic but not sinusoidal, and, in the case $h > R$, it is purely sinusoidal, although the field amplitude decreased substantially. Figures 1c and 1d present the field profiles at the height $h = 10/7$ with $b = 4R$ and R, respectively. At $b = 4R$, as at $b = R$, the field profile remains sinusoidal. Even at b close to zero, the field profile is sinusoidal, although the field amplitude decreases as the distance between the magnets decreases.

ACKNOWLEDGMENTS

We thank the collaborators of the NPTs DONIKS and mill 150 at the Makeevka metallurgical plant for assistance in carrying out the experiment on the industrial use of the above-given procedure of measurement of rolling speeds.

REFERENCES

1. Aharoni, A. and Gunders, E., Empirical Expression for the Axial Field of Cylindrical Bar Magnets, *IEEE Trans. Magnet.*, MAG-3 (4), 1967, p. 587.
2. RF Patent 2 013 151.

ISSN 1068-3755, Surface Engineering and Applied Electrochemistry, 2008, Vol. 44, No. 1, pp. 64–68. © Allerton Press, Inc., 2008.
Original Russian Text © V.I. Zelentsov, T.Ya. Datsko, E.E. Dvornikova, 2008, published in Elektronnaya Obrabotka Materialov, 2008, No. 1, pp. 75–80.

OPERATING EXPERIENCE

Fluorine Adsorption by Aluminum Oxihydrates Subjected to Thermal Treatment

V. I. Zelentsov, T. Ya. Datsko, and E. E. Dvornikova

Institute of Applied Physics, Academy of Sciences of Moldova, ul. Akademiei 5, Chisinau, MD-2028 Republic of Moldova
e-mail: vzelen@yandex.ru

Received October 27, 2007

Abstract—The adsorptive behavior of fluorine ions by the products of electrochemical machining (AMG-6 aluminum alloy samples) subjected to thermal treatment at temperatures of 100, 200, 400, and 600°C was investigated. The regimes were analyzed, which determine the steady-state distribution of fluorine between the bulk solution and the solid surface. All the samples exhibited good adsorptive properties for fluorine removal; the AMG-200 sample was the most efficient. The kinetic curves and adsorption isotherms were plotted. It was shown that the increase in the solution temperature lead to an increase in the adsorptive capacity for all the samples. This gave evidence of the chemical nature of the investigated process. The following mechanism of fluorine fixation on the modified surface of aluminum oxihydrates was proposed: the anion exchange of F^--ions with surface OH^--groups with formation of covalent bonds, which further transform into ionic bonds.

DOI: 10.3103/S1068375508010134

INTRODUCTION

Despite the fact that the phenomena of adsorption from solutions on solid surfaces lies at the basis of many chemical and technological processes, the theory of adsorption of ionic compounds has not been fully developed. Though molecular adsorption has been paid definite attention in the literature, significantly less attention has been given to the adsorption of small-size ions by oxyhydroxide adsorbents [1, 2]. The authors, using as an example investigations of the adsorption of fluorine ions by aluminum oxihydrate, intended to demonstrate the applicability of molecular adsorption models with the aim to describe the adsorption of ions from solutions.

The products of electrochemical dimensional machining (ECDM) of AMG-6 aluminum alloy were used as an adsorbent [3]. The precipitates obtained during the machining were washed of electrolyte ions, dewatered, and dried in air at room temperature and subjected to subsequent thermal treatment at 100, 200, 400 and 600°C (the notations AMG-100, AMG-200, AMG-400, and AMG-600 are used for the treated samples hereafter). The adsorbtive and structural properties of the samples, as well as their chemical and phase composition, were investigated (Table 1).

The initial sample was a porous material with a specific area of 163 m^2/g and a specific pore volume of 0.282 cm^3/g [4]. The initial sludge composition was as follows: 26.9% Al, 1.34% Mg, and 0.15% Fe. The chemical composition corresponds to the formula $Al_2O_3 \cdot 3.24H_2O$. According to the X-ray structural analysis, the initial sample is aluminum trihydrate (baierite) with reflections at 4.777 and 4.341 Å with a pseudoboehmite (10.811 Å) addition [5]. The principle applicability of ECDM products of AMG-6 alloy subjected to thermal treatment as adsorbents for fluorine removal from natural

Table 1. Adsorption and structural characteristics and composition of the products of ECDM of AMG-6 alloy subjected to thermal treatment

Regimes of thermal treatment (T, °C)	Specific area S, m^2/g	Specific pore volume V_s, cm^3/g	Effective pore radius r_{ef}, Å	mol H_2O/mol Al_2O_3	Phase composition
Initial	163	0.282	35	3.24	Baierite, pseudoboehmite traces, amorphous phase
100	170	0.294	34	2.85	Crystallized baierite
200	358	0.457	26	2.00	Baierite residues, amorphous phase
400	317	0.467	29	0.35	γ-Al_2O_3, amorphous phase
600	251	0.485	39	0.089	Well-crystallized γ-Al_2O_3

subterranean waters (with an initial fluorine content of about 1 mmol/l) was reported in [4].

For a rational approach to the choice of conditions and objects for purification while solving problems of this type, it is necessary to know the regularities of the adsorption process of fluorine on the surfaces of a sorbent particle and the mechanism of fixation of fluorine ions in a wide range of its initial concentrations.

With this aim, a systematic investigation of the adsorption of fluorine ions by AMG-100, AMG-200, AMG-400, and AMG-600 samples was undertaken.

Table 2. Change in the pH of the water and NaF solution (0.01 M) with AMG samples

Sample	pH of the suspension after 10 min of adsorption	
	water, PH ~6	NaF solution, PH ~7
$AMG_{initial}$	5.70	9.05
AMG-200	5.90	8.80
AMG-400	8.25	9.25
AMG-600	8.25	9.35

EXPERIMENTAL

Numerous papers have been devoted to the problem of water purification from fluorine ions [6–8], but all of them refer to fluorine removal from solutions with small concentrations of up to 1 mmol/l. In the present research, NaF solutions were used with concentrations from 10^{-4} to 5×10^{-1} mol/l. The adsorption was performed at a constant solution pH of 5.6–6.2. The preliminary experiments on the fluorine adsorption from NaF solutions by AMG samples have shown that, over 10 minutes of the adsorption process, the medium pH differed from its initial values and increased to 9.5 (Table 2). This can serve as an indirect indicator of the ion-exchange character of the processes that occur in the system.

The experiments were carried out in an acetate buffer solution (1 M CH_3COONa + 0.5 M CH_3COOH) to exclude the influence of the medium pH on the fluorine adsorption [9]. A 0.5 M Na_2SO_4 solution was added to maintain the ionic strength of the solution during adsorption. A 0.5 mm fraction of the samples was used; the S : L relationship was 1 : 250. The adsorption process was performed with continuous stirring and control over the change in the fluorine concentration until a equilibrium was reached. A pH-121 ionometer equipped with a fluorine-selective ELIS-131F electrode was used for the registration. The pH was determined with an accuracy of 0.05% and the content of fluorine ions with an accuracy of ±0.1 mmol/l. The fluorine content in the solution was determined using a calibration plot.

Kinetic experiments were performed to determine the time during which the equilibrium was reached; the activity of fluorine ions (the emf in mV of the F-selective electrode according to the ionometer readings) was registered each 30 s during the 180 min of the adsorption process. The fluorine concentration was determined using a calibration plot $E = f(-\log C_F)$ for various adsorption durations. The kinetic curves were plotted in C_F coordinates as a function of time (for an initial fluorine content of 0.03 mol/l); these curves were employed to determine the time during which the equilibrium was reached for each sample (Fig. 1). As can be seen in the figure, the main fluorine quantity (up to 80%) was adsorbed during 60 min of the process. The time needed to reach the equilibrium amounted to 180 min for all the samples; the further contact of the solution and the absorber did not lead to a substantial adsorption increase.

The adsorption experiments were carried out according the following procedure. A buffer solution and some quantity of water were added to a definite volume of the investigated solution to obtain the specified concentration of fluorine ions in the solution. The volume of the buffer solution always amounted to 50% of the entire solution volume. Then, a weighed amount of the adsorbent dried at 105°C and stored in a desiccator before weighing was introduced into the solution with a known concentration of fluorine ions and kept under continuous stirring until the equilibrium was reached. When the experiment was finished, the emf value E (mV) of the fluorine-selective electrode was determined, and the steady-state content of fluorine ions in the solution was found using a calibration plot. The fluorine quantity adsorbed by the sample was determined using the difference between the initial and final fluorine concentrations. The real concentration of fluorine ions corrected for the activity coefficient of fluorine

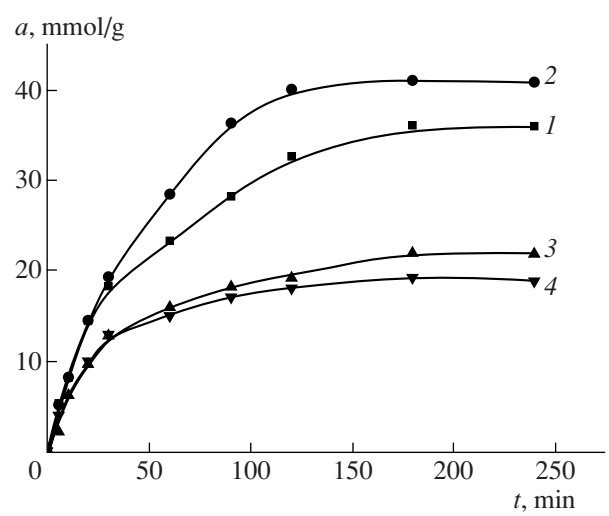

Fig. 1. Kinetics of fluorine adsorption at 20°C by AMG samples subjected to thermal treatments at different temperatures, °C: (*1*) 100, (*2*) 200, (*3*) 400, and (*4*) 600.

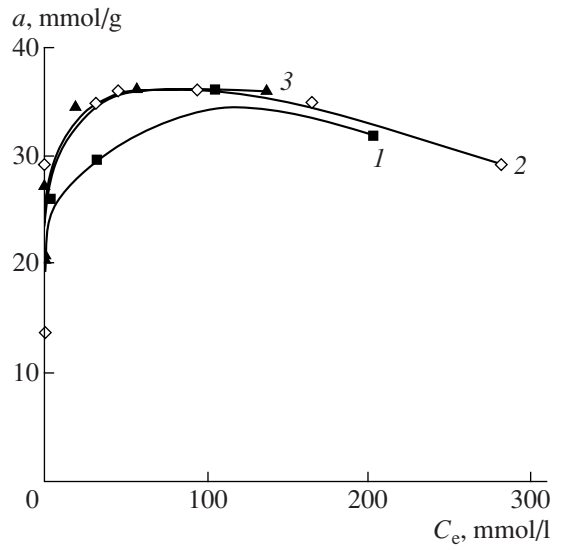

Fig. 2. Isotherms of adsorption of fluorine ions by AMG-100 samples at different solution temperatures, °C: (*1*) 20, (*2*) 30, and (*3*) 40.

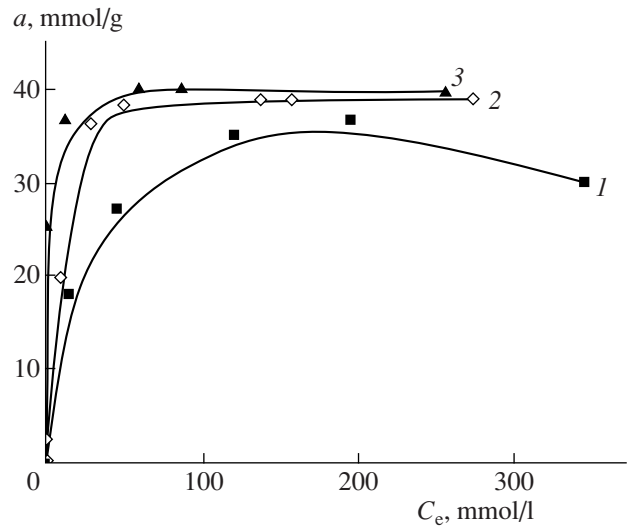

Fig. 3. Isotherms of adsorption of fluorine ions by AMG-200 samples at different solution temperatures, °C: (*1*) 20, (*2*) 30, and (*3*) 40.

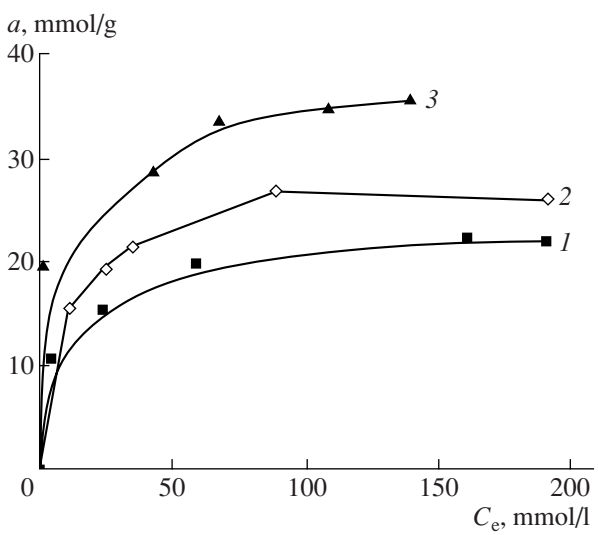

Fig. 4. Isotherms of adsorption of fluorine ions by AMG-400 samples at different solution temperatures, °C: (*1*) 20, (*2*) 30, and (*3*) 40.

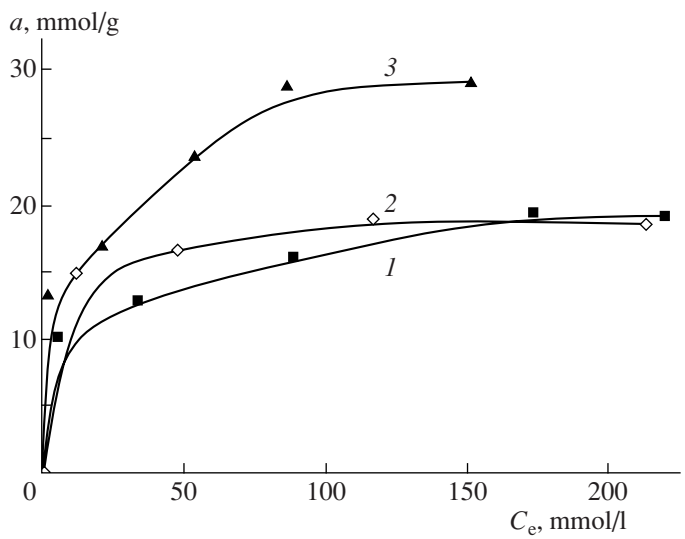

Fig. 5. Isotherms of adsorption of fluorine ions by AMG-600 samples at different solution temperatures, °C: (*1*) 20, (*2*) 30, and (*3*) 40.

ions at the respective ionic solution strength was used for the calculations [10, 11].

To obtain the kinetic and thermodynamic parameters of the adsorption process, we plotted the kinetic curves and adsorption isotherms at solution temperatures of 293, 303, and 313 K. The thermostatting was performed with an accuracy of ±0.2°C.

Experiments on fluorine desorption from the sample surface were also performed. The AMG samples were twice washed with distilled water after the fluorine adsorption and separation of the liquid phase; then, an initial buffer solution with pH = 5.7 was poured and the fluorine was desorbed under continuous stirring at solution temperatures of 20, 30 and 40°C. The solution was separated by centrifugation, and the quantity of fluorine ions in it was determined.

RESULTS AND DISCUSSION

Isotherms of fluorine adsorption by AMG-6 samples at various temperatures are shown in Figs. 2–5. As can be seen, the isotherms of all the samples, according to the Giles classification [12], correspond to Langmuir

monomolecular adsorption. Extremely high values of the fluorine adsorption at low equilibrium concentrations of fluorine ions are markedly seen. This is characteristic for a high affinity of an adsorbate to an adsorbent and is an indirect indicator of the chemical nature of the adsorption. The increase in the solution temperature at adsorption influences the adsorptive capacity of the samples relative to the fluorine ions in various manners. The adsorption capacity of the AMG-100 sample virtually did not change with the temperature increase (Fig. 2); this is associated with the stability of its crystal structure. The solution temperature increase for the AMG-200 and AMG-400 samples (Figs. 3, 4) lead to an increase in their adsorptive activity: a_m increased to 40 mmol/g for the former sample and exceeded the adsorptive capacity of the AMG-100 sample, and the adsorptive capacity of the AMG-400 sample was close to it at the solution temperature of 40°C. Evidently, the samples behave in a similar way due to the hydrothermal transformation of the highly dispersed X-ray amorphous aluminum monohydroxide and oxide in materials with high content of hydroxyl exchange water [13].

The adsorption isotherms for NaF in all the tested samples are satisfactorily described by the Langmuir equation mainly for steady-state fluorine concentrations up to 100–150 mmol/l. This allows one to find the a_m value with a fair accuracy as a slope of the curve of the C_e/a dependence as a function of C_e according the equation of the monomolecular Langmuir adsorbtion in the linear form. The isotherms of adsorption for NaF at 20°C for the AMG-100, AMG-200, AMG-400, and AMG-600 samples plotted in the coordinates of the equation are shown in Fig. 6. In Table 3, the values of the parameters of the Langmuir equation calculated and experimentally determined for the tested samples are presented.

As can be seen, the calculated and experimentally obtained a_m values are rather close. The scattering of these values is probably linked with the various natures of the surfaces of the tested samples. The AMG-100 sample, which is actually aluminum trihydrate (a well-crystallized baierite) with a great content of hydroxyl water, is characterized by the maximal adsorbtive capacity. As was shown in [4], the thermal treatment of AMG samples at 200°C is accompanied by phase transitions and amorphization of the structure, which leads to the development of the maximal specific area. Therefore, though the AMG-200 sample contains a considerably lower water amount than the AMG-100, its adsorbtive capacity with respect to fluorine was at the same level (~36 mmol/g). The AMG-600 sample, a well-crystallized γ-Al_2O_3 with a minimal water content,

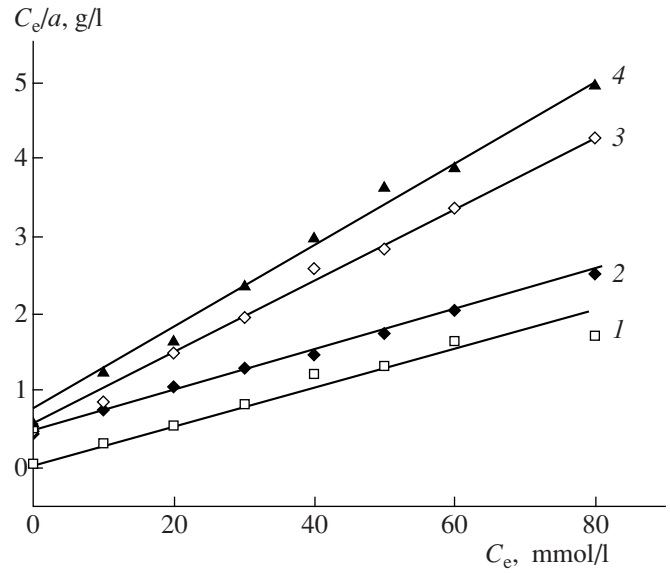

Fig. 6. Isotherms of adsorption of fluorine ions by AMG samples in coordinates of the Langmuir equation in the linear form: (*1*) AMG-100, (*2*) AMG-200, (*3*) AMG-400, and (*4*) AMG-600.

Table 3. Parameters of the Langmuir equation for the fluorine adsorption process by AMG samples

Sample	C_e, mol/l	Solution temperature, K	a_m exp., mmol/g	a_m calcul., mmol/g	K
AMG-100	0.107	293	35.60	33.50	0.330
	0.095	303	36.40	37.89	0.337
	0.058	313	36.40	37.41	0.668
AMG-200	0.295	293	36.20	39.11	0.056
	0.029	303	40.60	42.86	0.115
	0.060	313	39.80	40.65	0.351
AMG-400	0.162	293	22.20	21.32	0.095
	0.089	303	26.90	30.40	0.066
	0.140	313	34.20	35.97	0.132
AMG-600	0.174	293	19.60	19.06	0.087
	0.117	303	18.80	19.52	0.171
	0.153	313	28.40	27.42	0.608

possessed the minimal fluorine adsorptive capacity. The AMG-400 sample occupied the intermediate position.

In the conditions of fluorine adsorption from a weak-acid medium (pH ~ 6), the ionization of molecules occurs on the surface of oxyhydroxide particles according the following reactions:

$$Al(OH)_3 \longrightarrow Al(OH)_2^+ + OH^-;$$

$$Al(OH)_3 \longrightarrow AlOH^{2+} + 2OH^-;$$

$$AlOOH \longrightarrow AlO^+ + OH^-;$$

$$Al_2O_3 + 3H_2O \longrightarrow 2Al(OH)_2^+ + 2OH^-.$$

As a result, the surface groups acquire a positive charge; this leads to their strong electrostatic interaction with the fluoride ions from the solution accompanied with formation of the following compounds: $Al(OH)_2^+F^-$, $AlOH^{++}2F^-$, AlO^+F^-, and AlF_3.

Thus, the adsorption mechanism of fluorine ions by aluminum oxyhydroxides comprises several parallel processes: an ion exchange of F^- by OH^- (this is confirmed by the data in Table 2—the solution pH increases from 7 to 9.5 without any buffer); the coulomb attraction of fluorine ions by positively charged surface sites and formation of chemical bonds. During experiments with adsorption of fluorine ions from solutions with a high initial concentration >0.3 M, (Figs. 2–5) an interesting phenomenon was observed. The curve drops after the maximal adsorption was reached (a monolayer forms) with simultaneous growth of the steady-state concentration of fluorine ions in the bulk solution. The phenomenon when the fluorine adsorption decreases can be explained by the increase of the coulomb repulsion of fluoride ions with the same sign from the occupied surface and formation of sodium fluoride molecular clusters that cannot be adsorbed on the surface.

CONCLUSIONS

The adsorption of fluorine ions from aqueous solutions by the products of electrochemical dimensional machining (ECDM) of AMG-6 aluminum alloy subjected to thermal treatment at temperatures of 100–600°C was investigated. All the samples exhibited an effective adsorption for removal of fluorine ions from aqueous solutions. The adsorptive capacity of the samples reached up to 40 mmol/g. The isotherms of fluorine adsorption by these samples were registered for solution temperatures of 20, 30, and 40°C. The isotherms for all the tested samples were well described by the equation for the Langmuir monolayer adsorption in a linear form. A good coincidence of the values of the adsorptive capacity of the samples for fluorine removal, which were calculated according the Langmuir equation and found experimentally, was shown. It was stated that the fixation of fluorine ions on the sample surface occurs due to ionic exchange of fluorine ions with hydroxide groups, electrostatic interaction of F^--ions with the surface positive sites, and a subsequent formation of chemical compounds.

ACKNOWLEDGMENTS

The authors are indebted to Member–Correspondent of the ASM A.I. Dikusar for his interest in this research.

REFERENCES

1. Koganovskii, A.M., Levchenko, T.M., and Kirichenko, V.A., *Adsorbtsiya rastvorennykh veshchestv* (Adsorption of Dissolved Substances), Kiev: Naukova Dumka, 1977.
2. Giles, Ch., Ingram, B., and Clunie, J., *Adsorbtsia iz rastvorov na tverdykh poverkhnostyakh* (Adsorption from Solutions on Solid Surfaces), Moscow: Mir, 1986.
3. Davydov, A. and Kozak, E., *Vysokoskorostnoe elektrokhimicheskoe formoobrazovanie* (High-Rate Electrochemical Forming), Moscow: Nauka, 1990.
4. Zelentsov, V.I. and Datsko, T.Ya., A Porous Structure of the Products of ECPT of Aluminum Alloy Subjected to Thermal Treatment, *Elektron. Obrab. Mater.*, 1999, no. 4, pp. 59–65.
5. Mirkin, L.I., *Spravochnik po rentgenostrukturnomu analizu polikristallov* (Handbook on the X-ray Analysis of Polycrystals), Moscow: Fizmatgiz, 1961.
6. Klyachko, V.A. and Apel'tsyn, I.E., *Ochistka prirodnykh vod* (Purification of Natural Waters), Moscow: Stroiizdat, 1971.
7. Kul'skii, L.A. and Strokach, P.P., *Tekhnologiya ochistki prirodnykh vod* (Technology of Purificatiion of Natural Waters), Kiev: Vysshaya shkola, 1986.
8. Romanov, A.M., Drondina, R.V., Matveevich, V.A., et al., *Ochistka podzemnykh vod ot toksichnykh primesei elektrokhimicheskimi metodami* (Purification of Subterranian Waters from Toxic Impurities by Electrochemical Methods), Chisinau, Shtiintsa, 1988.
9. *Kratkii spravochnik po khimii* (Desk Handbook of Chemistry), Kiev: Izd. AN Ukr. SSR, 1962.
10. Vasil'ev, V.P., *Termodinamicheskie svoistva rastvorov elektrolitov* (Thermodynamic Properties of Electrolyte Solutions), Moscow: Visshaya shkola, 1982.
11. Izmailov, N.A., *Elektrokhimiya rastvorov* (Electrochemistry of Solutions) Moscow: Khimiya, 1976.
12. Gregg, S. and Sing, K., *Adsorption, Surface Area, and Porosity*, London: Academic, 1967.
13. Chertov, V.M. and Zelentsov, V.I., Hydrothermal Modification of an Active Aluminum Oxide, *Kolloidn. Zh.*, 1973, vol. 35, no. 4, pp. 805–807.

ISSN 1068-3755, Surface Engineering and Applied Electrochemistry, 2008, Vol. 44, No. 1, pp. 69–72. © Allerton Press, Inc., 2008.
Original Russian Text © N.S. Dimitraki, S.N. Dimitraki, 2008, published in Elektronnaya Obrabotka Materialov, 2008, No. 1, pp. 81–85.

OPERATING EXPERIENCE

Measurement of a Conductor Cross Sectional Area

N. S. Dimitraki and S. N. Dimitraki

Technical University of Moldova, bulv. Stefan cel Mare 168, Chisinau, MD-2004 Moldova

Received October 10, 2007

Abstract—An electrical method of indirect measurement of the cross sectional area of a conductor covered by a dielectric covering at casting in a suspended state is considered. The description of the method, the structural and electric equivalent schemes, and a mathematical treatment describing the essence and correctness of the method, as well as an error analysis of the method and its permissible possibilities, are given. Conditions under which the error of the measurement of the cross sectional area is the least are given.

DOI: 10.3103/S1068375508010146

The continuity of a conductor dielectric cover obtained according to professor A.V. Ulitovskii's method [1] makes it impossible to use the traditional methods for measuring the resistance per unit of the conductor length, since such a conductor fails to have a full galvanic connection with the measuring circuit. Regardless of the measuring method and the circuit, at least one of the poles of the connection between the conductor being measured and the measuring circuit should be nongalvanic [2]. As a rule, the transient resistance of such a pole exceeds by several orders the resistance that is being measured. Therefore, for measuring the resistance per unit of length of the above conductor with sufficient accuracy for practice, there should be developed methods that exclude the poles resistances from the circuit of the conductor section being measured or at least minimize their values to ones sufficient for measuring the above resistance with sufficient accuracy for practice.

The present paper describes a measuring method including the Z resistance minimizing of one of the poles (of a complex character, as a rule) in a two-pole measuring circuit where the other pole that connects the measured conductor of R_1 resistance with the measuring circuit is resistive and the value of its junction resistance R_{pf} is significantly lower than the one being measured.

The essence of the method is explained by the structural scheme (Fig. 1a), the electrical equivalent circuits, and the voltage oscillograms (Fig. 2), which show that the measured conductor section of equivalent resistance $R_1 = r_x l_x$ and a sample conductor section of $R_{10} = r_0 l_0$ equivalent resistance with R_{pf} resistance of the preform (a preform is a thin metal bar whose end turns into a metal drop after being fused) are connected in a series circuit and together produce a negative feedback circuit of the OA operational amplifier, which is connected as a reversing circuit.

The sum of the $R_1 + R_2$ resistances, which are indicated in the scheme, form the amplifier load simultaneously with one arm of a four-arm bridge. The second arm of the bridge is formed by a series circuit $r_x l_x + R_{pf} + r_0 l_0$. The produced bridge is fed by the OA output voltage. The conductor section of l_x length that is being measured and a measuring arm of the bridge make a series circuit from one end via the PF preform of R_{pf} equivalent resistance (Fig. 1a) and from the other end via the CM coil of Z_{pf} equivalent and R_{inOA} input resistance of the operational amplifier.

The analysis of the method can be done with the help of the equivalent circuits presented in Fig. 1.

As one can see in the figure, the resistance $Z_{03} = (Z_b + R_{inOA}) \left\| \frac{r_x l_x + r_0 l_0}{A} \right.$ between points 0–3 comes into the measured arm of the above bridge. The bridge equilibrium considering this resistance will occur when

$$R_l r_0 l_0 = R_2 \left| r_x l_x + Z_{03} + R_{pf} \right| \quad \text{or}$$
$$R_l r_0 l_0 = R_2 \left[r_x l_x + R_{pf} + (Z_b + R_{inOA}) \left\| \frac{r_x l_x + r_0 l_0}{A} \right. \right], \tag{1}$$

where A is the OA amplifying and r_x, r_0, l_0, and l_x are the resistances per unit of length and the length of the conductor section being measured and the one being formed, correspondingly.

The final values of the resistances $Z_{03}(Z_{03} \neq 0)$ and R_{pf} $(R_{pf} \neq 0)$ give the conductor manufacturing error of the resistance per unit of length. The error value, as is shown below, significantly depends on the A amplification.

In order to determine these errors, let us examine two cases.

(a) The operational amplifier is ideal, i.e., $A = \infty$, $R_{inOA} = \infty$.

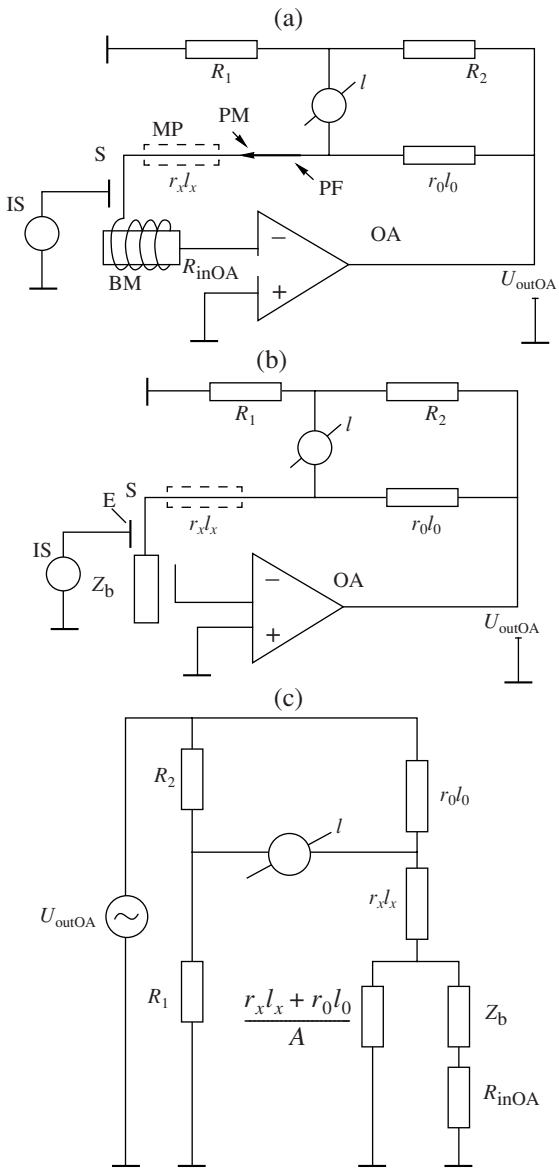

Fig. 1. Structural (a, b) and equivalent (c) circuits explaining the measuring principal of the cross section area with a dielectric cover at its casting.

In this case,

$$Z_{03} = (Z_b + R_{\text{inOA}}) \left\| \frac{r_x l_x + r_0 l_0}{A} \right. = 0, \quad (2)$$

and, when $R_1 = R_2$, the resistance of the measured conductor section is equal to

$$r_x l_x = r_0 l_0 - R_{\text{pf}}, \quad (3)$$

Table 1

A	10	100	1000	10000	10^5
∂d, %	–10.55	–1.01	–0.10	–0.01	0.00

(b) The operational amplifier is real, i.e., $A \neq \infty$, $R_{\text{inOA}} \neq \infty$.

In this case, at $R_1 = R_2$, the resistance $r_x l_x$ is equal to

$$r_x l_x = r_0 l_0 - R_{\text{pf}} - (Z_b + R_{\text{inOA}}) \left\| \frac{r_x l_x + r_0 l_0}{A} < r_0 l_0. \right. \quad (4)$$

Actually, $(r_x l_x + r_0 l_0) \ll |Z_b + R_{\text{inOA}}|$, $A \gg 1$, and, as a consequence,

$$Z_{03} = \frac{r_x l_x + r_0 l_0}{A} \left\| (|z_{\text{b}}| + R_{\text{inOA}}) \ll 1. \right.$$

If we take into consideration the obtained inequality

$$Z_{03} = R_{03} = (r_x l_x + r_0 l_0)/A \quad (5)$$

the condition of the bridge equilibrium becomes as follows:

$$R_l r_0 l_0 = R_2 \left(r_x l_x + R_{\text{pf}} + \frac{r_x l_x + r_0 l_0}{A} \right). \quad (6)$$

When $R_1 = R_2$ and $l_x = l_0 = 1$, the resistance of the conductor section being measured (provided equation (6) is taken into account) has the following form

$$l r_x = r_0 l - \frac{l(r_x + r_0)}{A} - R_{\text{pf}}. \quad (7)$$

From (7), it follows that the lr_x resistance of the manufactured conductor differs from that of the sample conductor by the value

$$r_0 l - l r_x = \frac{l(r_x + r_0)}{A} + R_{\text{pf}}, \quad (8)$$

and its relative divergence (in a percentage ratio) is

$$\partial r = \left(\frac{r_x + r_0}{A r_0} + \frac{R_{\text{pf}}}{r_0 l} \right) \times 100\%. \quad (9)$$

The resistance of the conductor section being measured and the resistances of the sample conductor section and of the preform with their physical values (length l and diameter d) and with the specific resistances of the conductor thread and of the preform have the following relations:

$$r_0 l = 4\rho_0 \frac{l_0}{\pi d_0^2}, \quad (10)$$

$$r_x l_x = 4\rho_x \frac{l_x}{\pi d_x^2}, \quad (11)$$

$$R_{\text{pf}} = 4\rho_{\text{pf}} \frac{lL}{\pi D^2}, \quad (12)$$

where L and D are the length and diameter of the perform, respectively.

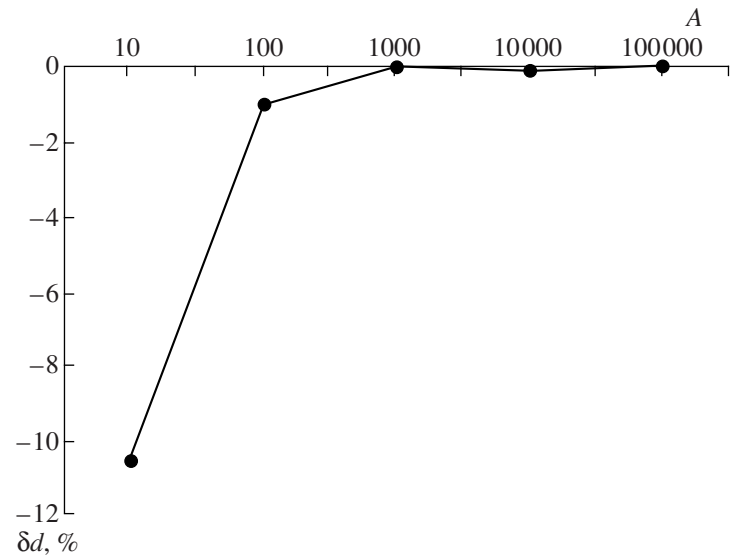

Fig. 2. The dependence of the measuring error of the conductor diameter as a function of the amplification of the operational amplifier.

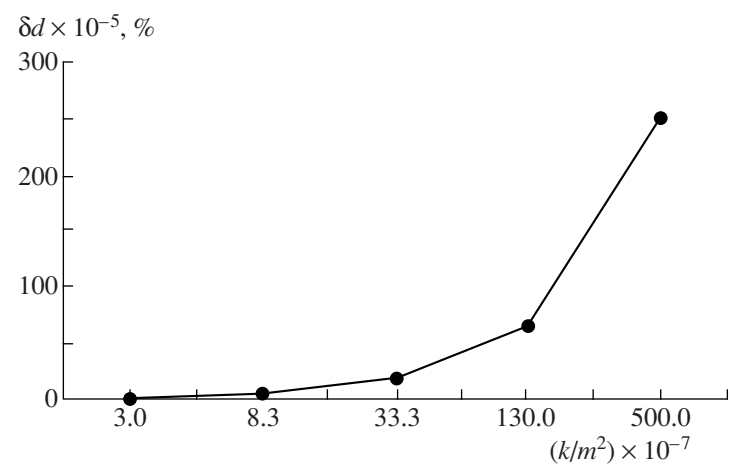

Fig. 3. Dependence of the measurement error of the conductor diameter as a k/m^2 function.

Substituting into (7) the relations (10), (11), (12) and considering that $\rho_0 = \rho_x = \rho_{pf}$, $l_0 = l_x = 1$, after the obvious reduction, we obtain

$$\frac{1}{d_x^2} = \frac{1}{d_0^2} - \frac{1}{A}\left(\frac{1}{d_x^2} + \frac{1}{d_0^2}\right) - \frac{kl}{m^2 d_0^2}, \tag{13}$$

where $k = L/1$, and $m = D/d_0$.

In order to simplify the estimation of the A and m values influence upon the divergence of the actual value of the d_x diameter from the sample d_0 diameter, equation (13) is disintegrated.

1. $k/m^2 = 0, A \neq \infty$, and then equation (13) obtains the following form:

$$\frac{1}{d_x^2} = \frac{1}{d_0^2} - \frac{1}{A}\left(\frac{1}{d_x^2} + \frac{1}{d_0^2}\right), \tag{13a}$$

hence,

$$d_x = d_0\sqrt{\frac{1 + \frac{1}{A}}{1 - \frac{1}{A}}}. \tag{13b}$$

Table 2

$K = L/l$	0.3	0.3	0.3	0.3	0.5
$m = D/d_0$	$3 \times 10^{-3}/3 \times 10^{-6}$	$3 \times 10^{-3}/5 \times 10^{-6}$	$3 \times 10^{-3}/10^{-5}$	$3 \times 10^{-3}/2 \times 10^{-5}$	$3 \times 10^{-3}/3 \times 10^{-5}$
k/m^2	$0.3/10^6 = 3 \times 10^{-7}$	8.3×10^{-7}	3.33×10^{-6}	1.3×10^{-5}	5×10^{-5}
$\partial d, \% = \left(1 - \frac{1}{\sqrt{1 - \frac{k}{m^2}}}\right) \times 100$	$1.5 \times 10^{-5}\%$	4.15×10^{-5}	16.6×10^{-5}	65×10^{-5}	250×10^{-5}

2. $k/m^2 \neq 0, A = \infty$, and then equation (13) appears as follows:

$$\frac{1}{d_x^2} = \frac{1}{d_0^2}\left(1 - \frac{k}{m^2}\right), \tag{14}$$

hence,

$$d_x = \frac{d_0}{\sqrt{1 - \frac{k}{m^2}}}. \tag{15}$$

From (13b) and (15), we can determine the divergence value (relative) of the diameter d_x from the preset d_0 for the first and second cases, correspondingly:

(1) $k/m^2 = 0, A \neq \infty$,

$$\partial d \longrightarrow \partial d_{\begin{cases} k/m^2 = 0 \\ A \neq \infty \end{cases}} = \left[1 - \sqrt{\frac{1 + \frac{1}{A}}{1 - \frac{1}{A}}}\right]; \tag{16}$$

(2) $k/m^2 \neq 0, A = \infty$,

$$\partial d_{\begin{cases} k/m^2 \neq 0 \\ A = \infty \end{cases}} = \left[1 - \frac{1}{\sqrt{1 - \frac{K}{m^2}}}\right]. \tag{17}$$

The total divergence is equal to

$$\partial d_{\begin{cases} k/m^2 \neq 0 \\ A \neq \infty \end{cases}} = \left[2 - \left(\sqrt{\frac{1 + \frac{1}{A}}{1 - \frac{1}{A}}} + \frac{1}{\sqrt{1 - \frac{K}{m^2}}}\right)\right]. \tag{18}$$

Tables 1 and 2 and Fig. 3 present the dependencies $\partial d_{\begin{cases} K/m^2 \neq 0 \\ A = \infty \end{cases}} = \varphi(A)$ and $\partial d_{\begin{cases} K/m^2 = 0 \\ A = \infty \end{cases}} = \varphi\left(\frac{k}{m^2}\right)$ for certain possible values of A and $\frac{k}{m^2}$, which show that, already at $A = 100$, the divergence of the real d_x diameter from the preset d_0 hardly exceeds one percent.

REFERENCES

1. Ulitovskii, A.V. and Averin, N.M., USSR Inventor's Certificate no. 8596, *Byull. Izobret.*, 1948.

2. Dimitraki, S.N., Methods and Devices for Measurement and Simulation of Microconductor Parameters and Microconductor Articles in the Production Process, *Doct. Sci. (Tech.) Dissertation*, Moldova Tech. Univ., 1986.

ISSN 1068-3755, Surface Engineering and Applied Electrochemistry, 2008, Vol. 44, No. 1, pp. 73–77. © Allerton Press, Inc., 2008.
Original Russian Text © V.I. Gun'ko, L.I. Onishchenko, I.Yu. Grebennikov, A.Ya. Dmitrishin, E.N. Slepets, S.O. Toporov, 2008, published in Elektronnaya Obrabotka Materialov, 2008, No. 1, pp. 86–90.

OPERATING EXPERIENCE

Study of Compatibility of Polymethylsiloxane Liquid PMS-10 with Structural Materials

V. I. Gun'ko, L. I. Onishchenko, I. Yu. Grebennikov, A. Ya. Dmitrishin, E. N. Slepets, and S. O. Toporov

Institute of Pulse Research and Engineering, National Academy of Sciences of Ukraine, pr. Oktyabr'skii 43-a, Nikolaev, 54018 Ukraine

Received July 24, 2007

Abstract—The influence of structural materials on the principal electrophysical characteristics (relative permittivity, loss tangent, volume electric resistivity, and electric strength) of polymethylsiloxane liquid PMS-10 is considered in the paper.

DOI: 10.3103/S1068375508010158

When creating high-voltage electrotechnical devices, the selection of the impregnating liquid dielectric is especially important. Along with the usual requirements such as high electric strength, low dielectric loss, resistance to the effect of partial discharges, resistance to gas, liquid dielectrics should possess a number of special properties; their compatibility with structural materials is the principal one. Liquid dielectric compatibility with structural materials is considered to mean not only the fact that the used structural materials shouldn't cause substantial reduction of the electrophysical parameters of a liquid dielectric but the

Compatibility testing results for polymethylsiloxane liquid PMS-10 with structural materials

Materials	Characteristics			
	E_{st}, kV/mm	ε	$\tan\delta$	ρ_v, Ω cm
Aluminum foil A5	16.8	2.61	4.6×10^{-4}	1.8×10^{12}
Polyethyleneterephthalate film PET-KE	17.2	2.68	5.2×10^{-4}	2.1×10^{12}
Polycarbone film PK-K	16.9	2.62	5.8×10^{-4}	2.2×10^{12}
Polypropylene film PP-KSS	17.1	2.63	6.1×10^{-4}	2.0×10^{12}
Steel St3	17.0	2.59	4.8×10^{-4}	2.5×10^{12}
Steel 45	17.1	2.60	4.9×10^{-4}	2.4×10^{12}
Copper M1	16.4	2.47	6.2×10^{-4}	1.6×10^{12}
Copper tin-coated with solder POS-40	16.9	2.51	5.4×10^{-4}	2.1×10^{12}
Brass L63	16.5	2.50	6.1×10^{-4}	1.8×10^{12}
Glass-epoxidephenol tube	17.2	2.69	5.4×10^{-4}	2.7×10^{12}
Glass fiber laminate STEF-1	17.1	2.68	6.1×10^{-4}	2.2×10^{12}
Amides PA6 of type "B"	16.9	2.41	4.8×10^{-4}	2.2×10^{12}
Polypropylene interpolymer 22007-29	16.8	2.48	5.6×10^{-4}	2.6×10^{12}
Rubber MBS-M1	13.6	2.38	8.4×10^{-4}	1.7×10^{12}
Rubber 51-1434	16.7	2.55	4.8×10^{-4}	2.1×10^{12}
Rubber 51-1486	16.8	2.52	4.8×10^{-4}	2.2×10^{12}
Rubber IRP-2052	8.7	2.31	1.9×10^{-3}	3.2×10^{12}
Lacquer LBS-1	17.1	2.52	3.8×10^{-4}	2.1×10^{12}

Note: Before compatibility testing with structural materials, the polymethylsiloxane liquid PMS-10 had the following characteristics: E_{st} = 17.4 kV/mm; ε = 2.64; $\tan\delta = 4.0 \times 10^{-4}$; $\rho_v = 2.5 \times 10^{12}$ Ω cm.

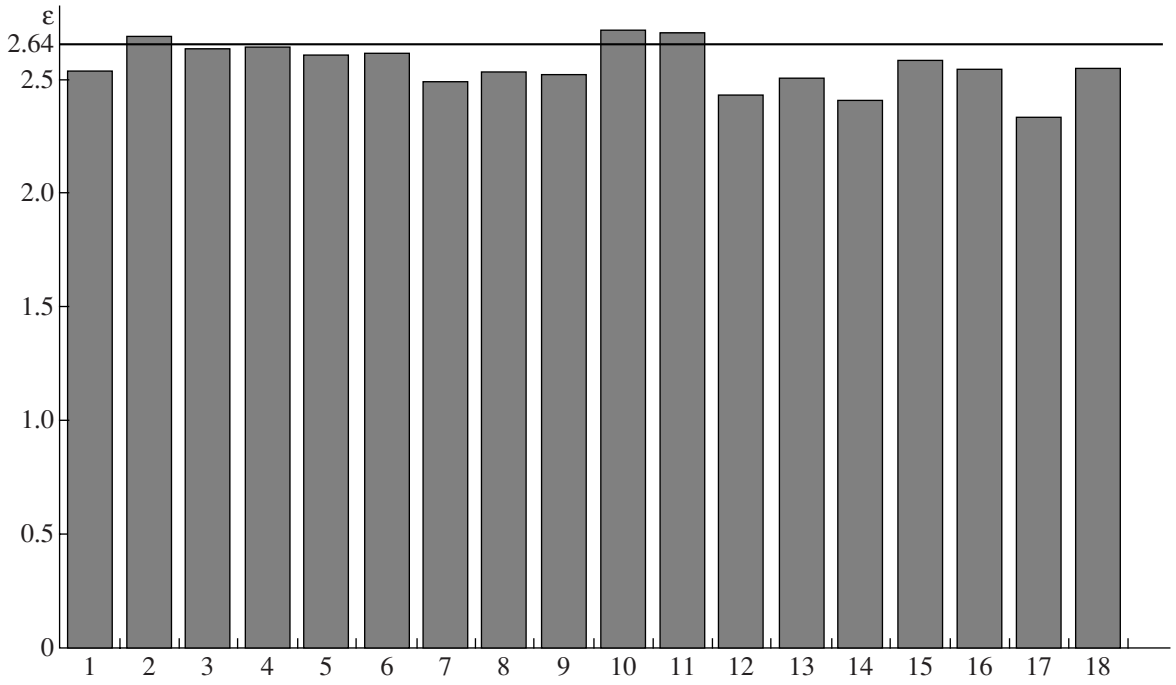

Fig. 1. Variation of polymethylsiloxane liquid PMS-10 relative permittivity after contact with structural materials. 1—aluminum foil A5; 2- polyethyleneterephthalate film PET-KE; 3—polycarbone film PK-K; 4—polypropylene film PP-KSS; 5—steel St3; 6—steel 45; 7—copper M1; 8—copper tin-coated with solder POS-40; 9—brass L63; 10—glass-epoxidephenol tube; 11—glass fiber laminate STEF-1; 12—amides PA6 of type "B"; 13—polypropylene interpolymer 22007-29; 14—rubber MBS-M1; 15—rubber 51-1434; 16—rubber 51-1486; 17—rubber IRP-2052; 18—lacquer LBS-1.

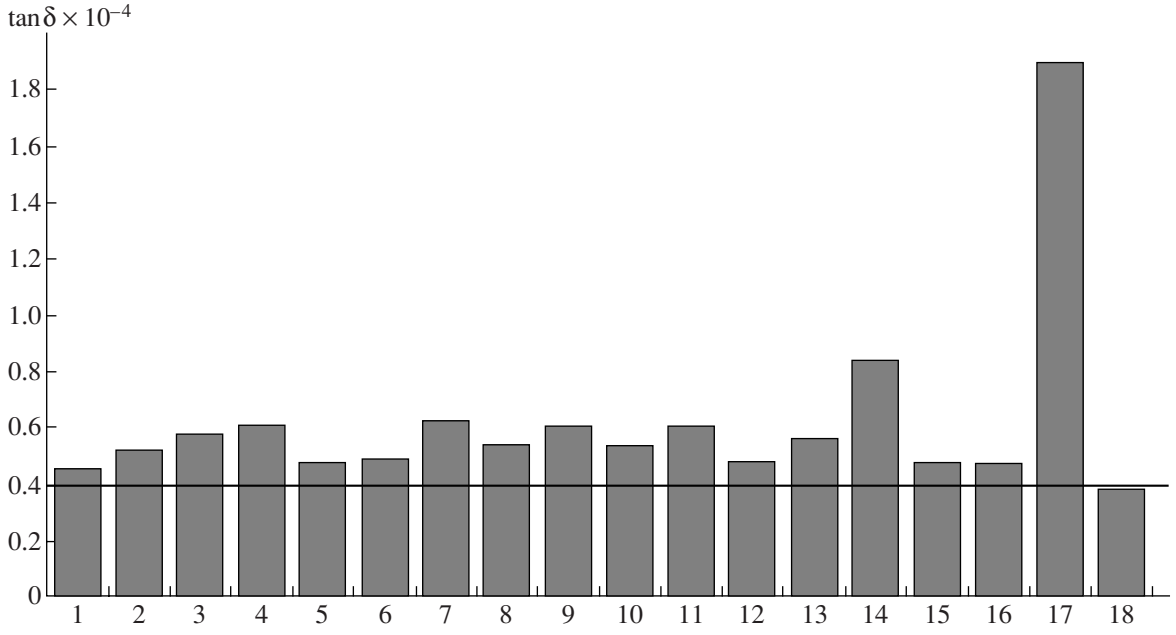

Fig. 2. Variation of the polymethylsiloxane liquid PMS-10 loss tangent after contact with structural materials. 1—aluminum foil A5; 2- polyethyleneterephthalate film PET-KE; 3—polycarbone film PK-K; 4—polypropylene film PP-KSS; 5—steel St3; 6—steel 45; 7—copper M1; 8—copper tin coated with solder POS-40; 9—brass L63; 10—glass-epoxidephenol tube; 11—glass fiber laminate STEF-1; 12—amides PA6 of type "B"; 13—polypropylene interpolymer 22007-29; 14—rubber MBS-M1; 15—rubber 51-1434; 16—rubber 51-1486; 17—rubber IRP-2052; 18—lacquer LBS-1.

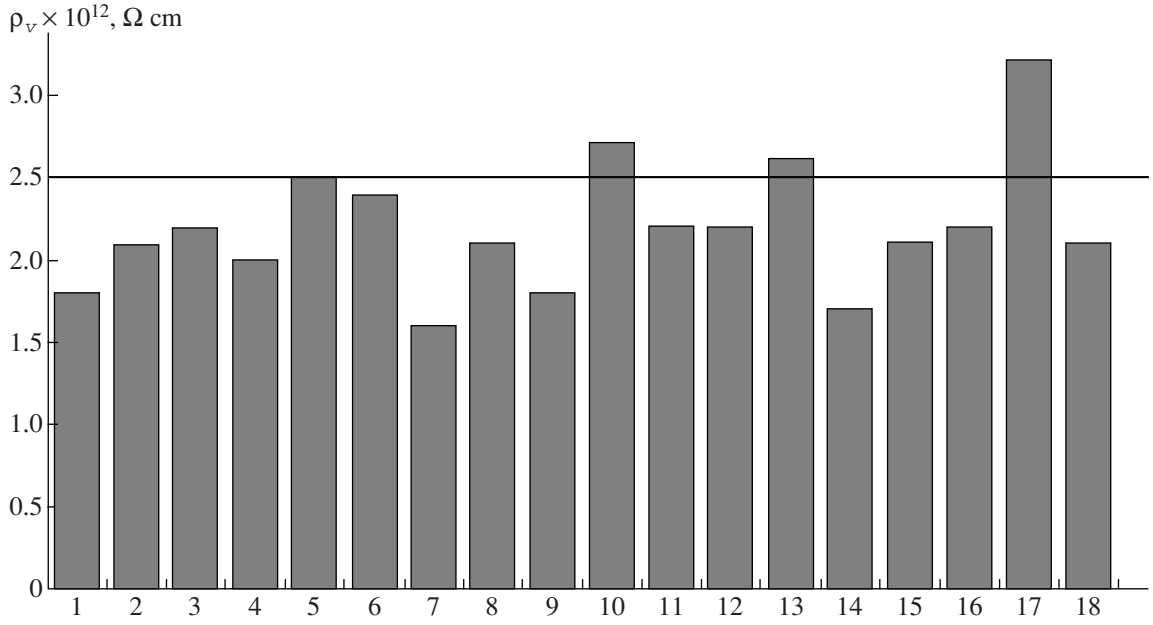

Fig. 3. Variation of polymethylsiloxane liquid PMS-10 volume electric resistivity after contact with structural materials. 1—aluminum foil A5; 2— polyethyleneterephthalate film PET-KE; 3—polycarbone film PK-K; 4—polypropylene film PP-KSS; 5—steel St3; 6—steel 45; 7—copper M1; 8—copper tin coated with solder POS-40; 9—brass L63; 10—glass-epoxidephenol tube; 11—glass fiber laminate STEF-1; 12—amides PA6 of type "B"; 13—polypropylene interpolymer 22007-29; 14—rubber MBS-M1; 15—rubber 51-1434; 16—rubber 51-1486; 17—rubber IRP-2052; 18—lacquer LBS-1.

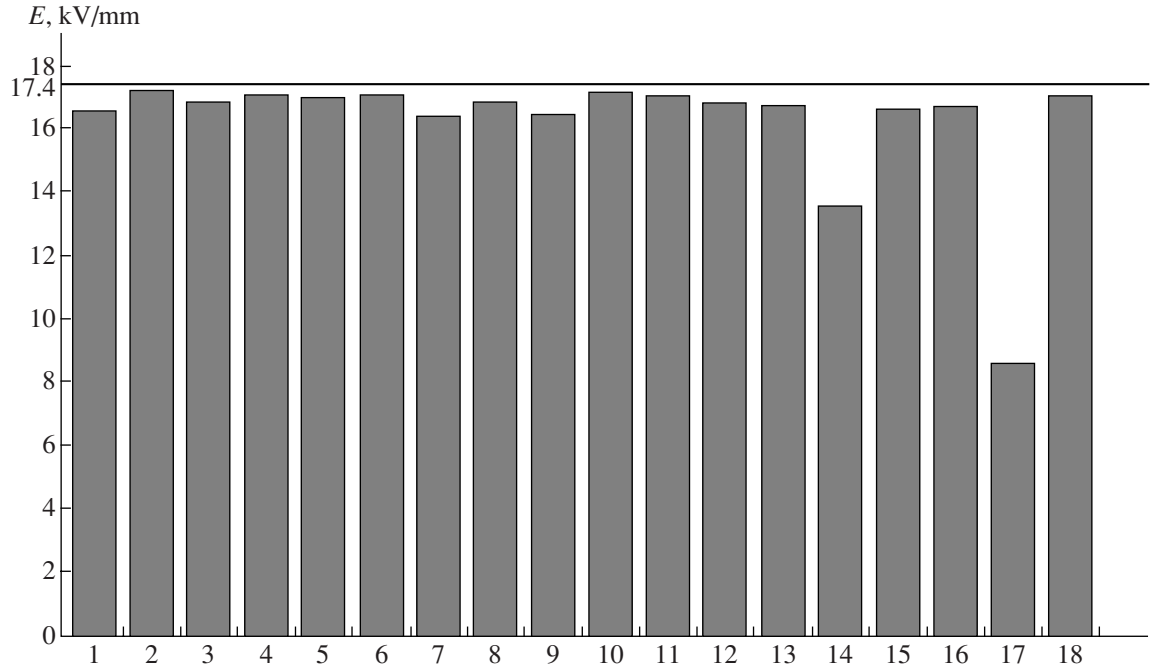

Fig. 4. Variation of the polymethylsiloxane liquid PMS-10 electric strength after contact with structural materials. 1—aluminum foil A5; 2—polyethyleneterephthalate film PET-KE; 3—polycarbone film PK-K; 4—polypropylene film PP-KSS; 5—steel St3; 6—steel 45; 7—copper M1; 8—copper tin coated with solder POS-40; 9—brass L63; 10—glass-epoxidephenol tube; 11—glass fiber laminate STEF-1; 12—amides PA6 of type "B"; 13—polypropylene interpolymer 22007-29; 14—rubber MBS-M1; 15—rubber 51-1434; 16—rubber 51-1486; 17—rubber IRP-2052; 18—lacquer LBS-1.

liquid itself shouldn't impair the physicomechanical characteristics of the constructive materials. Lack of specific information doesn't allow predicting the longevity of electrotechnical devices, in particular high-voltage impulse capacitors wherein liquid dielectrics are often exploited under the conditions of strong electric fields and elevated temperatures.

In the reference literature [1, 2], the data on the reciprocal influence of liquid dielectrics and structural materials are presented in a general form: oxidation active catalyzers are copper and its alloys, salts of organic acids, and metals with variable valency (copper, iron, cobalt, etc.), where, for every kind of liquid dielectric, it is necessary to individually select polymer materials, especially rubbers used to seal electrotechnical devices.

When evaluating the effect of structural materials on electrophysical parameters of liquid dielectrics used in capacitor manufacture [3–5], the emphasis is on the influence of polymer films, foil, and metal layers on liquid parameters, the compatibility being estimated according to the change of the liquid dielectric loss tangent as one of the most sensitive characteristics reflecting the working capacity of the impregnated insulation.

The assessment of the structural material used in capacitor manufacture on the electrophysical parameters of polymethylsiloxane liquid PMS-10, which is utilized as an impregnating dielectric in high-voltage pulse capacitors, is the purpose of this work.

The obtained research outcome can be employed not only for the creation of high-voltage pulse capacitors but for any other electrotechnical devices where polymethylsiloxane liquid PMS-10 is applied.

The following structural materials were selected to carry out the investigation: aluminum foil A5, polyethyleneterephthalate film PET-KE, polycarbone film PK-K, polypropylene film PP-KSS, copper M1, copper tin coated with solder POS-40, brass L63, glass-epoxidephenol tube, glass fiber laminate STEF-1, amides PA6 of type B, polypropylene interpolymer 22007-29, rubber MBS-M1, rubber 51-1434, rubber 51-1486, rubber IRP-2052, and lacquer LBS-1. The influence of capacitor paper of type KON and fluoroplastic hasn't been examined as they are inert to liquid dielectrics (according to the data of [1, 2]).

The polymethylsiloxane liquid PMS-10 was refined and stabilized by the corresponding technology before the investigation.

The structural material samples were placed into separate glass containers with polymethylsiloxane liquid PMS-10 and kept for 24 h under the following conditions:

—residual pressure not more then 6 Pa;

—temperature 125^{+5}°C.

After exposure under the mentioned conditions, the containers with the polymethylsiloxane liquid PMS-10 and the structural material samples were cooled in vacuum up to the environmental temperature and were held for 48 h.

The results of the measurement of the polymethylsiloxane liquid PMS-10 electrophysical parameters (relative permittivity ε, loss tangent $\tan\delta$, volume electric resistivity ρ_v, and electric strength E_{st} after contact with the structural materials are shown in the table and diagrams presented in Figs. 1–4. To make the variation of the PMS-10 electrophysical parameters more obvious, there are represented their values before the contact with the structural materials in the form of the base line.

As the results of the carried out researches show, nearly all the structural materials selected for the experiments on compatibility with the polymethylsiloxane liquid PMS-10 (except for the rubbers MBS-M1 and IRP-2052) don't considerably affect the PMS-10 parameters. Consequently, after the contact with the rubbers MBS-M1 and IRP-2052, the liquid electric strength reduced by 21.8 and 50%, respectively, and the PMS-10 loss tangent increased by a factor of 2.1 to 5.

The influence of copper and its alloys (brass L63) on the polymethylsiloxane liquid PMS-10 parameters is not so noticeable as the effect of these materials on the transformer oil characteristics [6], but, in this experiment, copper tin coated with solder POS-40 also influences the liquid parameters less when comparing them with the impact of copper and brass L63.

Generalizing the results of the conducted investigation on the assessment of the structural materials effect on the polymethylsiloxane liquid PMS-10 electrophysical characteristics, we can draw the following conclusions:

—the examined structural materials don't considerably impair the electrophysical characteristics of the polymethylsiloxane liquid PMS-10,

—the design of electrotechnical devices where polymethylsiloxane liquid PMS-10 is used should include the tinning of all copper current-carrying parts, and

—rubbers of types 51-1434 and 51-1486 can be recommended for use when there is possible contact with polymethylsiloxane liquid PMS-10.

REFERENCES

1. Berezin, V.B., Prohorov, N.S., Rykov, G.A., et al, *Elektrotekhnicheskie materialy* (Electrotechnical Materials), (Reference-book), Moscow: Energoatomizdat, 1983.

2. *Spravochnik po elektrotekhnicheskim materialam* (Handbook on Electrotechnical Materials), Koritskii, Yu.V. et al., Eds., Moscow: Energoatomizdat, 1986.

3. Andreev, A.M., Zhuravleva, N.M., Aleksandrova, N.P., and Galakhova, N.M., Change of Working Characteristics of the Film-Impregnated Capacitor Insulation due to the Interrelation of Its Components, *Elektrotekhnika*, 1996, no. 3, pp. 69–71.

4. Zhuravleva, N.M., Andreev, A.M., Molodova, L.A., and Lutskaya, T.V., Selection of Impregnating Fluids for High-Voltage Film Capacitors, *Elektrotekhnika*, 1994, no. 4, pp. 55–58.

5. Andreev, A.M., Zhuravleva, N.M., Sazhin, B.M., and Lutskaya, T.V., Assessment of Specific Power-Consumption of Film Capacitor Structures Impregnated with Liquid Dielectrics, *Elektrotekhnika*, 1994, no. 9, pp. 57–60.

6. Gun'ko, V.I., Dmitrishin, A.Ya, Toporov, S.O., and Feshchuk, T.A., Investigation of Compatibility of T-1500 Transformer Oil with Structural Materials, *Elektron. Obrab. Mater.*, 2006, no. 5, pp. 77–79.

ISSN 1068-3755, Surface Engineering and Applied Electrochemistry, 2008, Vol. 44, No. 1, pp. 78–80. © Allerton Press, Inc., 2008.
Original Russian Text © S.I. Vlasov, A.V. Ovsyannikov, 2008, published in Elektronnaya Obrabotka Materialov, 2008, No. 1, pp. 91–94.

OPERATING EXPERIENCE

The Rate of Surface Generation of Charge Carriers at the Semiconductor–Glass Interface

S. I. Vlasov and A. V. Ovsyannikov

Ulugbek National University of Uzbekistan, Studencheskii gorodok, Tashkent, 700174 Republic of Uzbekistan
vlasov@uzsci.net

Received August 28, 2007

Abstract—A method was proposed that allows to one to determine the temporal dependence of the rate of the surface generation at the semiconductor–insulator interface. It was shown that the rate of surface generation in metal–insulator–semiconductor (MIS) structures made of n-Si covered by a lead-borosilicate glass was a function of time.

DOI: 10.3103/S106837550801016X

The majority of modern semiconductor devices contain a semiconductor–insulator interface as a constituent part. The method of isothermal relaxation of capacitance in metal–insulator–semiconductor (MIS) structures in the process of formation of an inversion layer charge is most often used to study the generation–recombination behavior of interfaces [1]. This method is based on the registration of variations of capacitance of MIS structures with a constant inversion voltage V_1 applied to it after the voltage pulse V_2; the variation of capacitance is registered that corresponds the increase in the charge of the inversion layer for $V_2 > V_1$. The following equation is used to describe the temporal behavior of the process of the capacitance variation in an MIS structure:

$$\frac{1}{C^3(t)}\frac{dC(t)}{dt} = \frac{Sn_i}{C_d N_m \varepsilon\varepsilon_0} + \frac{n_i}{C_d N_m \tau}\left(\frac{C_\infty}{C(t)} - 1\right)\frac{1}{C_\infty}, \quad (1)$$

where $C(t)$ is the instant capacitance value, C_d is the capacitance of the dielectric layer, C_∞ is the structure capacitance at the end of the relaxation process, N_m is the impurity concentration in the semiconductor, n_i is the impurity concentration in the intrinsic semiconductor, τ is the lifetime of the thermally generated charge carriers, S is the rate of surface generation, ε is the semiconductor permittivity, and ε_0 is the permittivity of the vacuum [2]. While deriving equation (1), the authors [2] assumed that the rate of the surface recombination is constant; hence, its value does not change in the process of the capacitance relaxation.

The increase in the voltage pulse applied across the structure leads to the change of the bending in the energy band diagrams. As a result, part of the surface states filled with electrons appear to lie higher than the Fermi level for the case of an n-type semiconductor (Fig. 1).

The process of thermal generation leads to liberation of electrons and changes the charge of the surface states. In the process of thermal ionization, at first, electrons are librated from those surface states with higher energy, which are located near the conduction band. Consequently, electrons from deeper surface states are liberated. If the density of the surface states is spread uniformly in the examined energy range (ΔE, Fig. 1), then the number of electrons generated in the unit of time is also constant. Hence, the rate of surface generation is also a constant value in this case. However, the distribution of surface states within the forbidden gap of a semiconductor, as a rule, possesses a rather sophisticated shape [3–5]. When the pulse voltage increase

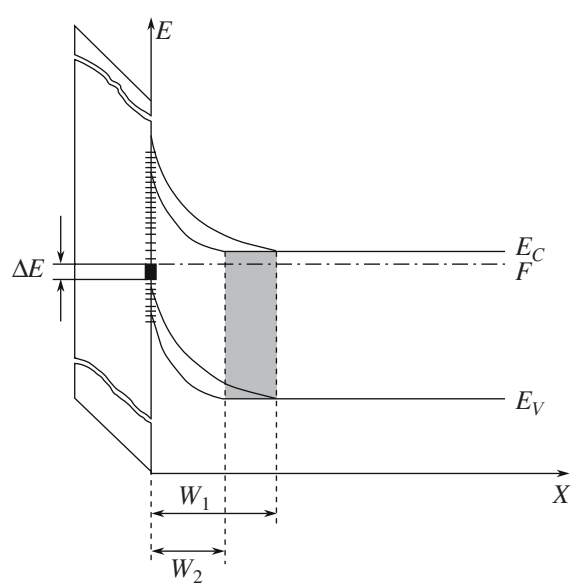

Fig. 1. Energy band diagram of an MIS structure; the energy range of recharging the surface stated is shown.

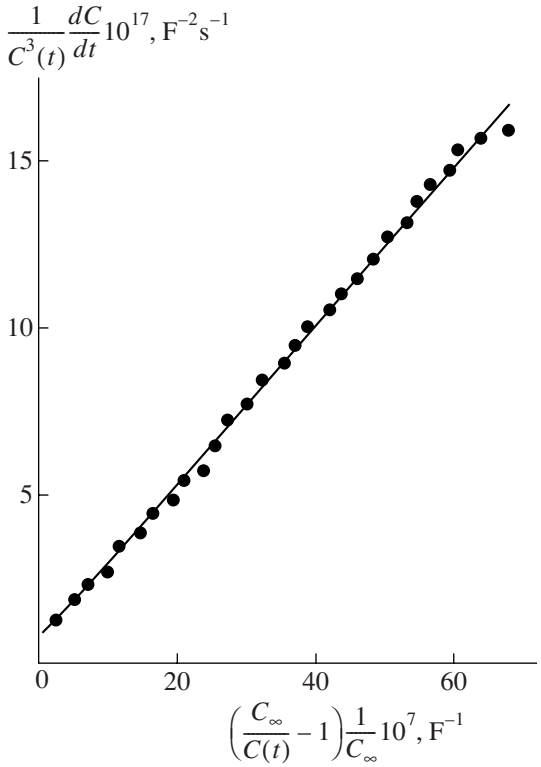

Fig. 2. Experimental $C(t)$ values for one of the MIS structures plotted according to Eq. (1).

corresponds to the energy range with nonuniform distribution of the density of surface states, then the rate of surface generation is a function of time. Furthermore, for the voltage switch $V_1 \longrightarrow V_2$, which corresponds to the inversion of the surface conductance, the broadening of the space charge layer of the semiconductor from W_2 to W_1 occurs at the initial time moment (Fig. 1). Further, with the development of the bulk and surface thermal generation, the accumulation of minority charge carriers occurs in the semiconductor near the semiconductor–dielectric interface; that is, the charge of the inversion layer increases. The increase in the charge of the inversion layer leads to the shielding of the electric field, which penetrates into the semiconductor, and the width of the space charge layer in the semiconductor decreases from W_1 to W_2. The bending in the energy band diagrams reduces due to the decrease in the electric field strength, and the part of the surface states localized in the energy range ΔE becomes filled with electrons. Hence, in the process of capacitance relaxation in MIS structures, the rate of surface generation of charge carriers is not constant but is a function of time.

To confirm all that was mentioned above, the $C(t)$ dependence was measured for an Al–n-Si–glass–Al structure using the method reported in [2]. A lead-borosilicate glass of the following mass-percentage composition was used: 33% SiO_2, 40% PbO, 24% B_2O_3, 2% Al_2O_3, and 1% Ta_2O_3. The thermal reflow of the initial mixture was performed on Si wafers (KEF-15 with the ⟨100⟩ crystallographic orientation) at a temperature of 700°C for 30 min with a subsequent annealing at 400°C for 10 min.

The relaxation dependences were measured in the dark at a frequency of 150 kHz at a temperature of T = –50°C after a 4 $\longrightarrow$ 18 V voltage switch. The obtained dependences (Fig. 3, curve *1*) were processed using equation (1). One of the calculated dependences is shown in Fig. 2. Using this dependence and assuming that the rate of the surface generation was constant, we found, according to method [2], a value of the rate of the surface generation equal to S = 55 cm/s.

Further, using the initial conditions of the relaxation dependence $C(t)$ and the meaning of the capacitance of

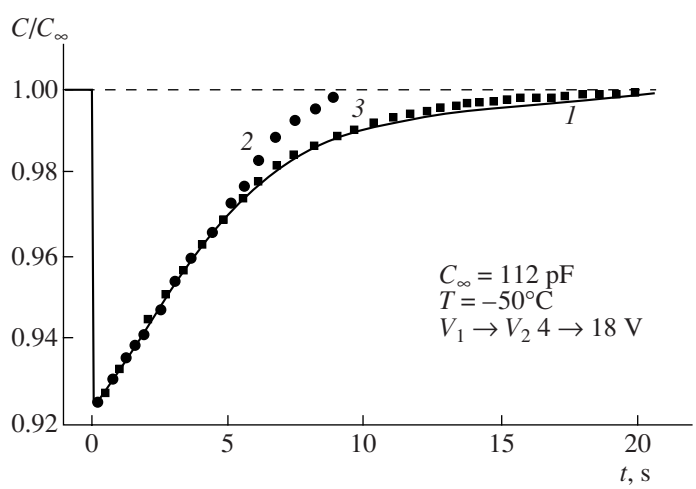

Fig. 3. Experimental (*1*) and calculated (*2*, *3*) dependences of the dark capacitance relaxation of the MDS structure in the process of increasing of the inversion layer charge after the voltage switch from 4 to 18 V.

the structure at the initial moment of relaxation, we solved equation (1) with respect to time:

$$t = \frac{B - AC_\infty}{B^2 C_\infty}\ln(C) + \frac{AC_\infty - B}{B^2 C_\infty}\ln(BC - BC_\infty - ACC_\infty) - \frac{1}{BC} + \eta, \quad (2)$$

where $A = \frac{Sn_i}{C_d N_m \varepsilon\varepsilon_0}$, $B = \frac{n_i}{C_d N_m \tau}$, and η is the integration constant equal to

$$\eta = -\frac{(B - AC_\infty)}{B^2 C_\infty}\ln(C) + \frac{(AC_\infty - B)}{B^2 C_\infty}\ln(BC_n - BC_\infty - ACC_\infty) + \frac{1}{BC_n}. \quad (3)$$

Using equations (1)–(3) and the $C(t)$, C_d, C_∞, N_m, S, and τ values determined experimentally, we found the calculated dependence $t = t(C/C_\infty)$ assuming that the rate of the surface generation S does not change with time and compared it with the experimental dependence. Figure 3 shows the experimental dependence (curve *1*) and calculated dependences (curves *2*, *3*) of the capacitance relaxation of the MIS structure (normalized to the value of the steady-state capacitance C_∞). It can be seen that the displayed dependences only coincide at the initial section of the relaxation curve. We employed the method of optimal fit of parameters and the experimental curve of capacitance relaxation of MIS structures at a fixed temperature and found an empirical temporal dependence of the rate of surface generation for the entire relaxation process. The dependence found can be approximated using numerical processing methods by the following equation:

$$S = S_0[0.5 - 0.3\arctan(t)], \quad (4)$$

where S_0 is the rate of surface generation at the initial time moment.

Comparison of the calculated dependence $t = t(C/C_\infty)$ (Fig. 3, curve *3*) with the experimental dependence (curve *1*) under the assumption that the temporal dependence of the rate of the surface generation S is described by equation (4) showed a fair coincidence of both dependences.

On the basis of the presented data, we can conclude that, in MIS structures constructed on the basis of n-type silicon covered with a lead-borosilicate glass layer, the rate of surface generation is a temporal function, which can be approximated by equation (4).

REFERENCES

1. Kang, J.S. and Schroder, D.K., The Pulsed MIS Capacitor, *Phys. Stat. Sol. A*, 1985, vol. 89, no. 13, pp. 13–43.
2. Zerbst, M., Relaxationseffekte an Halbleiter-Isolator-Grenzflachen, *Z. Angew. Phys.*, 1966, vol. 22, pp. 30–33[D1]. Relaxation Effects on Holbeiter Isolator-grenzflochen, *Z. Angew. Phys.,* 1962, no. 30, pp. 22–29.
3. Parchinskii, P.B., Vlasov S.I., and Nasirov A.A., Influence of γ-Radiation on the Characteristics of the Interface Silicon–Lead-Borosilicate Glass, *Fiz. Tekh. Poluprovod.* (S.-Peterburg), 2004, vol. 38, no. 11, pp. 1345–1348 [*Semiconductors* (Engl. Transl.), vol. 38, issue 11, pp. 1304–1307].
4. Parchinskii, P.B., Influence of Ultrasonic Treatment on the Surface State Density on the Interface Silicon–Silicon Dioxide Subjected to γ-Quanta Radiation, *Mikroelektronika*, 2005, vol. 34, no. 6, pp. 420–423.
5. Berman, L.S., Analysis of the Temporal Instability of Parameters of the Interface Dielectric-III-V Compound Using a Method of Isothermal Capacitance Relaxation, *Fiz. Tekh. Poluprovod.* (Leningrad), 1977, vol. 31, no. 1, pp. 78–81.